Design and Setup of an Ultracold Dual-species Rydberg Experiment

MASTERARBEIT
vorgelegt von
Nicolas Zuber

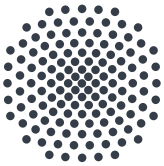

Universität Stuttgart

Hauptberichter: Prof. Dr. Tilman Pfau
Mitberichter: Prof. Dr. Martin Dressel

5. Physikalisches Institut
Universität Stuttgart
20. April 2016

ZUSAMMENFASSUNG

Im Rahmen dieser Arbeit wurde ein Apparat zum Kühlen und Fangen von Lithium- und Rubidiumatomen aufgebaut. Dies ist Teil eines neuen Doppelelement-Rydberg Experiments mit ultrakalten Quantengasen. Heutzutage werden mit kalten und ultrakalten Quantengasen Fragestellungen zur Bose-Hubbard-Physik [1, 2], zu Quantensystemen im Nichtgleichgewicht [3] und zu dipolare Vielteilchensystemen [4] untersucht. Ein physikalisches System, welches in den letzten Jahren beträchtliche Aufmerksamkeit erfahren hat, sind Rydbergatome in ultrakalten Quantengasen. Bei Rydbergatomen befindet sich mindestens ein Elektron in einem hoch angeregten Zustand. Durch die hohe Anregung sind Rydbergatome sehr groß. Bei einer Hauptquantenzahl des Rydbergelektrons von $n = 200$ besitzt das Atom die etwa 40.000-fache Größe des Grundzustandsatoms. Dadurch besitzen Rydbergatome eine hohe Polarisierbarkeit, welche mit n^7 skaliert und sie stark untereinander und mit ihrer Umgebung wechselwirken lässt. Diese Eigenschaft macht Rydbergatome zu sensitiven Sensoren, welche zum Beispiel einzelne Photonen zerstörungsfrei detektieren können [5].

Werden Rydbergatome in einem Hintergrundgas angeregt, können sich viele neutrale Atome des Hintergundgases innerhalb des Rydbergorbits des Elektrons befinden und durch Streuung mit diesem wechselwirken. Im Jahr 2000 wurden durch Greene, Dickinson und Sadeghpour Rydbergmoleküle vorhergesagt, bei denen eine Bindung zwischen neutralem Atom und Rydbergatom aufgrund der Streuung des Rydbergelektrons am neutralen Atom entsteht [6]. Solche homonuklearen Rydbergmoleküle wurden 2009 zum ersten Mal in Stuttgart von Bendkowsky u. a. in einem ultrakalten Gas aus Rubidiumatomen nachgewiesen [7]. Heutzutage wurden auch Rydbergmoleküle der Elemente Cäsium [8] und Strontium [9] nachgewiesen.

Diese Arbeit handelt von dem Entwurf und Aufbau essenzieller Teile eines neuen Rydbergversuchsaufbaus, mit Hilfe dessen ultrakalte Rubidium- und Lithiumquantengase erzeugt werden können und welcher die Erforschung von heteronuklearen Rydbergmolekülen ermöglicht. Diese konnten im Gegensatz zu homonuklearen Rydbergmolekülen bislang noch nicht nachgewiesen werden und sollen als Ausgangspunkt für weitere Experimente dienen. Unter anderem sollen mit Hilfe von Rydbergmolekülen räumliche Korrelationen in ultrakalten Quantengasen untersucht werden [10]. Außerdem eröffnet sich die Möglichkeit mit Hilfe von D-Zustands-Rydbergmolekülen ultrakalte Ion-Atom Stöße zu untersuchen. In einem schwachen magnetischen Feld lassen sich diese Moleküle ausrichten und durch Pho-

toionisation ein Ion-Atom-Paar in einem definierten Anfangszustand erzeugen. Im Rahmen dieser Arbeit wurde ein Zeemanabbremser entwickelt und gebaut, der es ermöglicht, gleichzeitig schnelle Lithium- und Rubidiumatome auf niedrige Geschwindigkeiten abzubremsen, sodass sie in einer magneto-optischen Falle (MOT) gefangen werden können. Die dafür nötigen Spulen wurden simuliert und aufgebaut. Eine weitere Vorgabe für das Experiment war die Möglichkeit, hohe homogene Magnetfelder von bis zu einem Kilogauß zu erreichen, um mit Hilfe von Feshbachresonanzen die Wechselwirkungsstärke zwischen den Atomen zu variieren. Hierfür wurden Simulationen durchgeführt und die nötigen Spulen aufgebaut. Für einen sicheren dauerhaften Betrieb wurde eine mikroprozessorgesteuerte Temperatur- und Stromüberwachung realisiert. Zusätzlich wurden Spulen auf allen drei Raumachsen zur hochpräzisen Kompensation störender Streufelder, wie zum Beispiel dem Erdmagnetfeld, entwickelt und simuliert. Im späteren Experiment sollen Rubidium und Lithium in einer optischen Dipolfalle bis zur Quantenentartung gekühlt werden. Hierzu wurden verschiedene Fallengeometrien berechnet und simuliert, um einen möglichst großen Überlagerung der beiden Atomwolken zu gewährleisten.

In Kapitel 2 dieser Arbeit werden die theoretischen Grundlagen der Laserkühlung und das Fangen von Atomen erklärt. Hierzu wird zunächst die Atom-Licht Wechselwirkung und der Einfluss magnetischer Felder auf die atomaren Zustände behandelt. Der Fokus des Kapitels liegt auf der Erläuterung verschiedener Kühlmethoden. Unter anderem wird der Zeemanabbremser, die MOT, optische Molassekühlung und Verdampfungskühlung in optischen Dipolfallen beschrieben.

Kapitel 3 handelt von dem Versuchsaufbau und Lasersystem des Experiments. Es wird zuerst ein Überblick über die Vakuumkammer gegeben und danach detaillierter auf den Ofen und die Hauptkammer eingegangen. Im Folgenden wird das zum Kühlen und Abbilden verwendete Lasersystem beschrieben und es werden Berechnungen für eine optimale Dipolfallengeometrie vorgestellt. Die Entwicklung, Simulation und der Aufbau des Zeemanabbremsers werden detailliert beschrieben und bilden den Hauptteil dieses Kapitels. Weiterhin werden Rechnungen und Simulationen zu den MOT- und Feshbachspulen diskutiert. Die Spulen zur hochpräzisen Kompensation von Streufeldern werden am Ende des Kapitels vorgestellt.

CONTENTS

LIST OF FIGURES

LIST OF TABLES

1 INTRODUCTION

In the past century scientists discovered a variety of new physical effects during their quest for lower and lower temperatures. In 1911 Kamerlingh Onnes observed a sudden drop in the electrical resistivity of mercury at $T = 4.3\,K$ when cooling it with liquid helium. This was the first observation of superconductivity, an effect based on the superfluidity of the bosonic Cooper pairs of fermionic electrons. Liquid helium-4 was first produced only three years earlier and did not only serve as a coolant, but showed interesting effects itself, e. g. in its density around 2.2 K [11]. This behavior was explained in 1938 by Kapitza [12] and independently by Allen and Misener [13] with the occurrence of a phase transition of the bosonic helium-4 to a superfluid state. Both superconductivity and superfluidity are macroscopic manifestations of quantum many body physics of fermions and bosons, respectively.

These two kinds of particles behave crucially different in quantum mechanics. The statistical behavior of bosons is described by Bose-Einstein statistics and at zero temperature all bosons of a non-interacting ensemble occupy the lowest energy state, forming a Bose-Einstein condensate. In contrast Fermions, described by the Fermi-Dirac statistics, occupy the available energy levels up to the Fermi energy with a maximum of one particle per level. Quantum mechanical effects caused by the different statistics were first studied in liquid helium and solid state systems. A prominent example is the BCS theory by Bardeen, Cooper and Schrieffer [14] published in 1957, describing type-I superconductivity.

The technological improvement of lasers and the invention of laser-cooling lead to a new approach to ultra-cold physics: the study of dilute atomic gases. First attempts of laser cooling immediately achieved temperatures of 1 K for atoms slowed by a Zeeman slower [15] and reached temperatures on the order of microkelvin in optical molasses [16]. With the development of magneto optical trapping, atoms could not only be cooled, but also trapped at temperatures well below 1 mK. Sub-Doppler cooling [17] opened the door to temperatures in the low microkelvin range. However, even at such low temperatures the achievable densities in the atom clouds are too low to reach quantum degeneracy. The recoil energy of a single photon sets the lower limit in the energy scale reached by light-based cooling techniques. As a consequence evaporative cooling in magnetic traps was developed. This allows temperatures well below 1 μK. In 1995 groups in Boulder at the University of Colorado [18] and at MIT [19] ob-

served the first Bose-Einstein condensation of rubidium respectively sodium atoms. This opened the door to a new approach to explore many body quantum physics. Quantum gases offer a high degree of control and tunability. Interactions for example can be tuned via Feshbach resonances and crystal-like structures can be created with optical lattices. Today, not only alkali atoms have been cooled to degeneracy, but also some alkaline earth metals, chromium, helium and the three lanthanides dysprosium, erbium and ytterbium.

Today, cold and ultracold quantum gases are employed to study Bose-Hubbard physics [1, 2], quenched quantum systems [3], dipolar many-body physics [4] and many more topics. One system which attracted considerable attraction in the past years is the excitation of Rydberg atoms in ultracold gases. Rydberg atoms possess at least one highly excited electron with a large principle quantum number n. In these atoms the electron is bound very weakly to the atomic core and is, in a classical picture, on an orbit far away from the atomic core. For a principle quantum number $n = 200$ its size is 40.000 times larger than its ground state. As a consequence, Rydberg states possess large polarizabilities scaling with n^7 and interact strongly with each other and their surrounding. This property makes Rydberg atoms very sensitive probes, for example capable of nondestructively detecting single photons [5].

Rydberg atoms excited in a background gas can have thousands of neutral ground state atoms inside the orbit of the Rydberg electron. Shifts of the spectroscopic Rydberg lines in a dense background gas at high temperatures were observed already in 1934 [20]. These shifts are explained with Fermis theory of low-energy scattering of an electron with a neutral atom [21]. In the year 2000 Greene, Dickinson, and Sadeghpour [6] applied this model to a single atom sitting within the orbit of a Rydberg electron and predicted molecules consisting of a Rydberg atom and a neutral atom. Such homonuclear Rydberg molecules were first observed in Stuttgart by Bendkowsky et al. [7] in an ultracold gas of rubidium atoms. Today, Rydberg molecules have been produced also in cesium [8] and strontium [9]. Moreover not only S-state molecules, but also D-state molecules [22, 23] and molecules with more exotic shapes, such as trilobite and butterfly molecules with a large permanent electric dipole moment [24, 25] have been observed. The production of heteronuclear Rydberg molecules however has not been realized yet.

This thesis reports on the setup of a new dual-species Rydberg experiment, enabling the study of heteronuclear Rb*Li-Rydberg molecules. These molecules consisting of a rubidium Rydberg and lithium ground state atom are well suited as in-situ probes to study spatial correlations in ultracold gases [10]. Since the size of the Rydberg molecule and the Fermi length are on the same order for typical parameters in the experiment, spatial correlations are expected to manifest itself

in the spectrum of trimers and higher order multimers. Moreover in the strongly interacting regime close to a Feshbach resonance in lithium [26], the scattering length can be tuned to length scales on the same order as the binding length of the Rydberg molecule, which is expected to manifest itself in a change of the Rydberg molecule spectrum.

Furthermore heteronuclear D-state Rydberg molecules provide excellent starting conditions to study ultracold ion-atom collisions in the quantum regime. Until now, significant work on ion-atom collisions has been done with various ion-atom combinations [27] in the cold classical Langevin regime, but not in the ultracold regime of quantum scattering. The hybrid traps mainly used by the ion-atom experiments combine a Paul trap for the ion and a magnetic or optical trap for the atoms. The use of Paul traps leads to micromotion of the ion, setting a limit for the minimum collision energy [28] and prevents leaving the classical regime. By optical trapping of the ion [29] the heating of the Paul trap can be avoided. The use of D-state Rydberg molecules follows a different path to enter the ultracold quantum regime by avoiding the use of a Paul trap. D-state molecules can be produced in atomic clouds trapped in an optical or magnetic trap. With a small magnetic field, these D-state molecules can be well aligned in the laboratory frame and provide a small and by the principle quantum number tuneable initial distance of the scattering partners. After photoionizing the Rydberg molecule, a short electric field pulse accelerates the ion to the desired collision velocity and initiates the scattering. The small initial distance permits to stay in the s-wave regime, even if small stray electric fields accelerate the ion. Due to the small reduced mass, the Rb^+-Li scattering partners have a s-wave scattering limit of $k_B \cdot 9\,\mu K$, which is much higher than the s-wave limit of other available mixtures of ultracold gases.

About this thesis: This thesis reports on the design and setup of pivotal parts of a new dual-species Rydberg experiment, which will allow for the production of ultracold degenerate quantum gases of rubidium and lithium, in which heteronuclear Rydberg molecules can be studied. In chapter 2 of this thesis the theoretical background of laser cooling and trapping is explained. The focus of the chapter lies on atom-light interaction and the influence of magnetic fields on the level structure of an atom. Subsequently, different cooling concepts are explained, namely the Zeeman slower, the magneto-optical trap, optical molasses and evaporative cooling in an optical dipole trap.

The topic of chapter 3 is the experimental setup with its vacuum chamber and the cooling laser system. Furthermore, a scheme of efficient evaporative cooling of lithium and rubidium in an optical dipole trap is presented. The main part of the chapter is dedicated to the simulation and setup of a dual-species Zeeman slower to decelerate lithium and rubidium simultaneously. The design of coils capable of

producing high magnetic fields an later used for the magneto-optical trap and as Feshbach coils, is presented. Additionally several magnetic field compensation coils which will be later used to compensate stray fields and the earth magnetic field, are discussed.

2

THEORY

2.1 LITHIUM AND RUBIDIUM

Lithium and rubidium will be both used in the new experiment. They are both alkali metals and have one electron in their outermost s-shell. Lithium has two stable isotopes of which ^{6}Li is a fermion with nuclear spin $I = 1$ and ^{7}Li is a boson with a nuclear spin of $I = 3/2$. In this experiment ^{6}Li will be used, which has a natural abundance of 7.6% and a mass of $m = 6.015\,u = 6.008 \times 10^{-26}\,kg$, where u is the atomic mass unit [30].

Rubidium has two bosonic isotopes: the stable ^{85}Rb and ^{87}Rb with an natural abundance of 72.2% and 27.8%, respectivly. The latter one is used in the experiment. It is radio active but the half time is in the order of 10^{10} years which makes it in practice stable. Its mass is 86.909 u and the nuclear spin is $3/2$ [31, 32]. It is more often used in cold atomic experiments than ^{85}Rb because of its positive scattering length, which prevents the collapse of the Bose-Einstein condensates. In the following lithium will refer to the ^{6}Li isotope and rubidium to the ^{87}Rb isotope.

The energy levels of ^{6}Li and ^{87}Rb are shown in figure 2.1. The optical transition used to cool lithium is the 2S-2P and for rubidium the 5S-5P transition. The wavelength of these transitions is around 671 nm for lithium and 780 nm for rubidium. The natural line width of these transitions is about $\Gamma = 2\pi \cdot 5.9\,MHz$ for the lithium $D_{1,2}$-line and $\Gamma_{D1} = 2\pi \cdot 5.8\,MHz$ for the D1-line respectively $\Gamma_{D2} = 2\pi \cdot 6.1\,MHz$ for the D2-line of rubidium [33, 34].

With the hyperfine splittings of the $2^2P_{3/2}$-state in lithium being smaller than its natural linewidth, the single levels of this state cannot be resolved and the open transition $2^2S_{1/2}F = 3/2 \rightarrow 2^2P_{3/2}F = 3/2$ is excited additionally to the cooling transition. Thus a strong repumper is needed for cooling. To pump back to the $2^2S_{1/2}F = 3/2$-state, the D_2-line with the $2^2S_{1/2}F = 1/2 \rightarrow 2^2P_{3/2}F = 3/2$ transition is used.

In the case of rubidium, the hyperfine splitting of $h \cdot 267\,MHz$ between the $5^2P_{3/2}F = 3$ state and the $5^2P_{3/2}F = 2$ is large compared to lithium, with h the Planck constant. However it is still small enough to allow off resonant excitation to the $F = 2$ state. This state decays with equal probability to the two $5^2S_{1/2}$ hyperfine states. The 6.8 GHz splitting between these levels makes the atom in the $F = 1$ state not accessible to the cooling light. The loss of atoms via this channel is

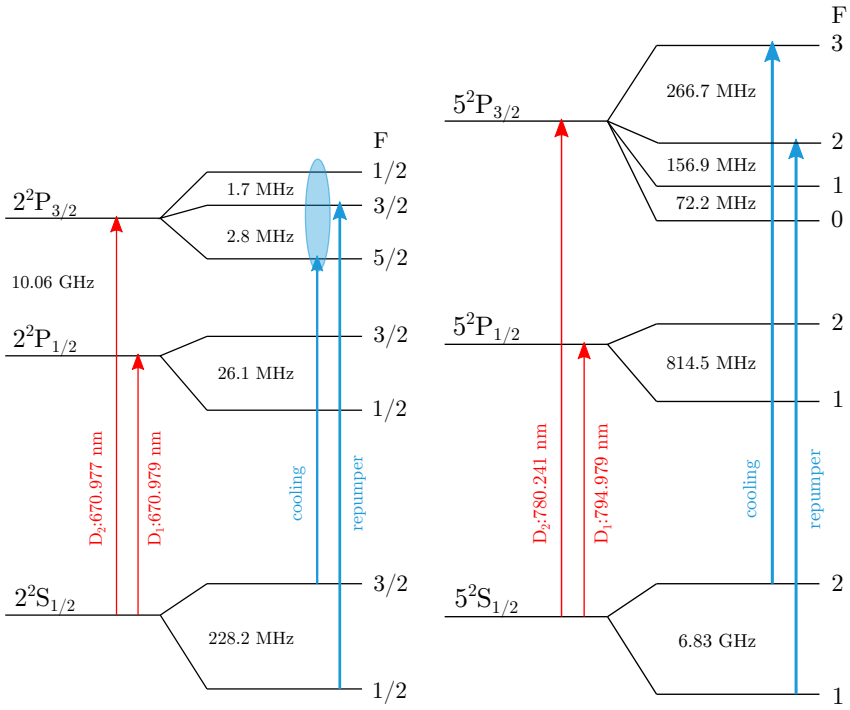

(a) Lithium 6 level scheme (b) Rubidium 87 level scheme

Figure 2.1: The hyperfine level scheme of lithium 6 and rubidium 87 which are used in this experiment. The relevant transitions for cooling the two atomic species are marked in blue. The hyperfine levels in the ^{6}Li $2^2P_{3/2}$ state are not resolved because the hyperfine splittings are smaller than the natural line width $\Gamma = 2\pi \cdot 5.9\,\mathrm{MHz}$.

prevented with a repumper laser on the $5^2S_{1/2}F = 1 \rightarrow 5^2P_{3/2}F = 2$ transition.

2.2 ATOM LIGHT INTERACTION

To cool and manipulate atoms, the interaction between the light and the atoms is of great interest. In general the interaction splits broadly speaking into two forces[1]. The *dipole force* is based on coherent absorption and stimulated emission of photons and the *scattering force* based on spontaneous emission.

To get an idea of these effects, we can treat the electric field as a classical monochromatic field

$$\boldsymbol{E}(\boldsymbol{r}, t) = \boldsymbol{E}(\boldsymbol{r}) \cos(\omega t + \phi) = \hat{\varepsilon} E(\boldsymbol{r}) e^{-i\omega t} + \text{c.c.} \tag{2.1}$$

with frequency ω, amplitude $E(\boldsymbol{r})$ and polarization vector $\hat{\varepsilon}$ inducing an atomic dipole moment. The dipole moment

$$\boldsymbol{d}(t) = \alpha(\omega)\boldsymbol{E}(t) = e \cdot \boldsymbol{x}(t) \tag{2.2}$$

oscillates with the same frequency as the field and is connected to it via the polarizability $\alpha(\omega)$. The induced dipole moment is created by an electron with charge e and mass m_e, which is displaced by $\boldsymbol{x}$. In the equation 2.2, the electric field was assumed to be spatially constant. This is a reasonable assumption, because the atom is usually small compared to the wavelength of the light. In the Lorentz model the atom is treated as a damped oscillator

$$\ddot{\boldsymbol{x}} + \Gamma(\omega)\dot{\boldsymbol{x}} + \omega_0^2 \boldsymbol{x} = -e\frac{\boldsymbol{E}(t)}{m_e}. \tag{2.3}$$

The electron is driven by the electric field but looses at the same time energy by radiation with the classical damping rate

$$\Gamma(\omega) = \frac{e^2\omega^2}{6\pi m_e \epsilon_0 c^3}. \tag{2.4}$$

Here ϵ_0 is the vacuum permittivity and c the speed of light. Solving the equation of motion for the damped harmonic oscillator leads to a solution for the polarizability

$$\alpha(\omega) = \frac{e^2}{2m_e}\frac{1}{\omega_0^2 - \omega^2 - i\Gamma(\omega)\omega}. \tag{2.5}$$

This complex polarizability is connected to the mechanical forces between light and atom in the following way.

1 This is only true for atoms with vanishing vector or tensor polarizabilties [35].

2.2.1 *Scattering force*

The energy absorbed and remitted per time by the atom in the Lorentz oscillator model is given by

$$P = \langle \dot{\boldsymbol{d}}\boldsymbol{E} \rangle = \frac{\omega}{\epsilon_0 c} \operatorname{Im}[\alpha] I. \tag{2.6}$$

The dot denotes the time derivative and $I = 2\epsilon_0 c|E|^2$ is the intensity of the light. The out of phase part of the dipole oscillation, which corresponds to the imaginary part of the polarizability, is therefore responsible for the absorption of the light. With the absorbed energy and the energy per photon, one can calculate the number of scattered photons per second

$$\Gamma_{sc} = \frac{P}{\hbar\omega} = \frac{1}{\hbar\epsilon_0 c} \operatorname{Im}[\alpha] I(\boldsymbol{r}). \tag{2.7}$$

This expression is valid not only for atoms but in general also for all polarizable particles in electric fields. For low saturation the classical Lorentz model gives already a good description. Taking equation 2.5, the scattering rate becomes

$$\Gamma_{sc} = \frac{3\pi c^2}{2\hbar\omega_0^3} \left(\frac{\omega}{\omega_0}\right)^3 \left(\frac{\Gamma}{\omega_0 - \omega} + \frac{\Gamma}{\omega_0 + \omega}\right)^2 I(\boldsymbol{r}) \tag{2.8}$$

where $\Gamma = \Gamma(\omega_0)$ is the on resonance scattering rate and ω_0 the frequency of the atomic transition [36]. Here one can see also the scaling of the scattering rate with the detuning. For a detuning which is much smaller than the transition frequency, equation 2.8 can be simplified by the rotation wave approximation to

$$\Gamma_{sc} = \frac{3\pi c^2 \Gamma^2}{2\hbar\omega_0^3} \frac{I(\boldsymbol{r})}{(\omega - \omega_0)^2} \propto \frac{I(\boldsymbol{r})}{\delta^2} \tag{2.9}$$

where $\delta = \omega - \omega_0$ is the detuning of the laser frequency in respect to the transition frequency. This will be important for dipole traps, which will be discussed in section 2.2.2.

If an atom scatters lots of photons, it is a considerable amount of time in the excited state, not absorbing any further photons. This causes saturation effects, which are not covered by the classical linear Lorentz model. In the case of large scattering rates, the classical treatment of the atom is not sufficient anymore. This is is important when using the scattering of the light to slow and cool atoms.

In a theoretical description for such a case, the atom is treated as a two level system, whereas the light field is still classical. Initially developed to describe the nuclear magnetic resonance, the optical Bloch equations provide a useful framework. The derivation is omitted here but can be found in [37].

The excited state population ρ_{ee} can be derived from the stationary solution of the optical Bloch equation, because the timescales for trapping and slowing are much longer than the lifetime τ of the excited state. In contrast to the Bloch equations for magnetic resonance, the damping factor $\Gamma = \tau^{-1}$ has to be phenomenological introduced to the formalism. In magnetic resonances the decay rates are negligible because of their frequency scaling ω_0^3. As a solution one gets

$$\rho_{ee} = \frac{1}{2}\frac{\frac{I}{I_{sat}}}{1 + \frac{4\delta^2}{\Gamma^2} + \frac{I}{I_{sat}}} = \frac{1}{2}\frac{s_0}{1 + \frac{4\delta^2}{\Gamma^2} + s_0} \tag{2.10}$$

with the saturation parameter

$$s_0 = \frac{I}{I_{sat}} . \tag{2.11}$$

The saturation intensity at resonance

$$I_{sat} = \frac{\hbar\Gamma\omega_0^3}{12\pi c^2} \tag{2.12}$$

gives an energy scale for the laser intensity. For example at $I = I_{sat}$ the atom is a fourth of the time in the excited state. For rubidium the saturation intensity for isotropic light polarization is $3.58\,\mathrm{mW/cm^2}$ for the D_2-line, which means even with modest intensities, the transition can be strongly driven.

The scattering force is caused by the photon momentum $\boldsymbol{p} = \hbar\boldsymbol{k}$, which is transferred to the atom in the absorption and emission process. If both, the absorption and emission process, would be completely random in their direction, the atom would undergo a random walk, but no net force would be present. Instead the direction of absorbed photons is defined by the laser beam and only emission happens in all spatial direction. This gives a net force of

$$\langle \boldsymbol{F}_{sc} \rangle = \hbar\boldsymbol{k}\Gamma_{sc} = \hbar\boldsymbol{k}\Gamma\rho_{ee}. \tag{2.13}$$

$$= \hbar\boldsymbol{k}\frac{\Gamma}{2}\frac{s_0}{1 + \frac{4\delta^2}{\Gamma^2} + s_0} . \tag{2.14}$$

The scattering rate Γ_{sc} is expressed as a product of the damping coefficient and the probability to be in the excited state and is shown in figure 2.2. This is possible for a steady state, in which the atom is interacting with a monochromatic light at constant intensity and the absorption and emission rate are in equilibrium. For the D_2 line of rubidium the excited state lifetime is around 26 ns. Thus for high intensities, one atom can scatter up to 19.1×10^6 photons per second. Other alkalis have similar lifetimes of their cooling transitions and thus scattering rates. This is important for the scattering force, because for $I \to \infty$ the ground and excited level population approaches

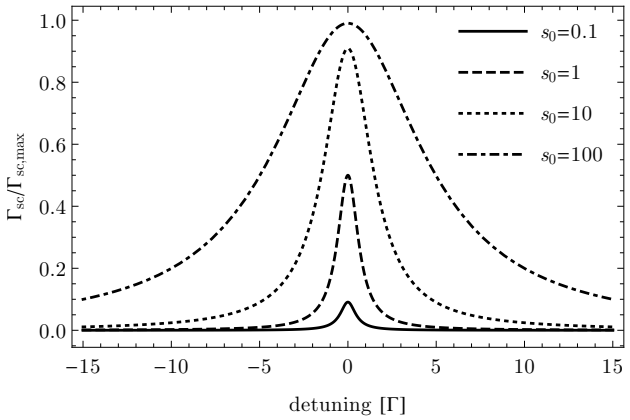

Figure 2.2: Spontaneous scattering rate Γ_{sc} of an atom plotted versus the detuning δ of the light for different saturation parameters s_0. For high intensities the scattering rate saturates and becomes power broadened.

one half and limits the scattering force to $F_{max} = \hbar k\Gamma/2$. The maximum acceleration

$$a_{max} = \frac{F_{sc}}{m} = \frac{\hbar k\Gamma}{2} \tag{2.15}$$

is $0.11 \times 10^6\ m/s^2$ for rubidium and $1.8 \times 10^6\ m/s^2$ for lithium, about 10^4 to 10^6 stronger than gravitational acceleration. This is used for example in the Zeeman slower, which slows atoms down from hundreds of meters per second to several meters per second on a distance less than one meter and is described in section 2.4.

The recoil momentum of one photon sets a limit to the minimum velocity of an atom cooled with laser light. This minimum velocity is called recoil velocity:

$$v_r = \frac{\hbar k}{m} \tag{2.16}$$

where m is the mass of the atom. For rubidium the recoil velocity is $0.6\,cm/s$ and for lithium $9.8\,cm/s$.

2.2.2 *Dipole force*

Due to the induced dipole moment, the atom has the following energy in the electric field averaged over many laser oscillations

$$V_{dip}(\boldsymbol{r}, t) = -\frac{1}{2}\langle \boldsymbol{d}(\boldsymbol{r}, t)\boldsymbol{E}(\boldsymbol{r}, t)\rangle \tag{2.17}$$

$$= -\frac{1}{2\epsilon_0 c}\,\mathrm{Re}\left[\alpha(\omega)\right]\, I(\boldsymbol{r}, t)\ . \tag{2.18}$$

Because the dipole moment is induced and not a permanent one, the factor $1/2$ has to be considered. This potential is proportional to the

intensity $I = 2\epsilon_0 c|E|^2$ of the light and the real part of the polarizability, which is describing the in phase oscillation of the dipole with the field. For a spatial varying intensity, the atoms are attracted to the lowest potential energies. The force acting on the atom is then

$$\boldsymbol{F}(\boldsymbol{r}) = -\nabla V_{dip}(\boldsymbol{r}) = \frac{1}{2\epsilon_0 c} \operatorname{Re}[\alpha(\omega)] \nabla I(\boldsymbol{r}) \tag{2.19}$$

and thus proportional to the gradient of the intensity.

Combining equation 2.4 and equation 2.5 the dipole potential becomes

$$V_{dip}(\boldsymbol{r}, t) = -\frac{3\pi c^2}{2\omega_0^3} \left(\frac{\Gamma}{\omega_0 - \omega} + \frac{\Gamma}{\omega_0 + \omega} \right) I(\boldsymbol{r}, t) \tag{2.20}$$

$$\overset{\text{rwa}}{=} \frac{3\pi c^2 \Gamma}{2\omega_0^3} \frac{I(\boldsymbol{r}, t)}{\omega - \omega_0} \propto \frac{I(\boldsymbol{r}, t)}{\delta} . \tag{2.21}$$

In the second step, the equation was simplified by using the rotating wave approximation (rwa). This is only valid for light not too far detuned.

Looking at the sign of the potential with respect to the detuning $\delta = \omega - \omega_0$, the potential is negative for red detunings ($\omega_0 > \omega$, $\delta < 0$) and positive for a blue detuning ($\omega_0 < \omega$, $\delta > 0$). The red detuning attracts atoms into the light field to regions with maximum intensity, whereas the blue detuning repels atoms out of the field.

As mentioned in section 2.2.1, the stochastic scattering process of the spontaneous force introduces a heating mechanism of the cold atoms. Increasing the detuning reduces the spontaneous scattering rate, but also the trap depth. Nevertheless large detunings are more preferable, because of the different scaling ($V_{dip} \propto I/\delta$, $\Gamma_{sc} \propto I/\delta^2$) of the trap depth and the scattering rate. The downside is the need of high laser power up to some hundred Watts, to create deep enough traps. In contrast to the scattering force in section 2.2.1, the dipole force does not saturate for increasing intensities.

Multilevel atoms

Real atoms have a much more elaborated level structure than the simple two levels, assumed in the model system above. To calculate the exact trapping potential for a real atom, this structure have to be taken into account. As in the classical case, the electric field can be assumed to be homogeneous over the extent of the atom, because the wavelength of the visible light is much larger than the atom. However the interaction Hamiltonian between the light and the atom is approximated by the dipole interaction

$$\mathcal{H}_{int} = -\hat{\boldsymbol{d}}\boldsymbol{E} \tag{2.22}$$

with the dipole operator $\hat{\boldsymbol{d}}$. With time independent perturbation theory, the energy shift of the eigenstates of the atom-light system can

be calculated. Because of the induced dipole moment the first order perturbation is zero and the second order gives an energy shift of the i-th eigenstate $|i\rangle$ of

$$\Delta E_i = \sum_{i \neq j} \frac{|\langle j|\, \mathcal{H}_{int}\, |i\rangle|^2}{E_i - E_j}. \tag{2.23}$$

Here E_j are the unperturbed eigenenergies of the states. The eigenstates $|i\rangle$ of the combined atom-light system are called dressed states [38]. Applying this to a two level atom results in same the energy shift of the ground state as the dipole potential calculated in the previous section [36]. This shift is also known as light shift or ac-Stark shift.

In this experiment lithium and rubidium are used. For infrared light, mostly the two transitions from $nS_{\frac{1}{2}} \rightarrow nP_{\frac{1}{2}}$ (D_1) and from $nS_{\frac{1}{2}} \rightarrow nP_{\frac{3}{2}}$ (D_2) contribute to the energy shift. This is true for the other alkalis as well. For a detuning larger than the hyperfine splitting and for using linear polarized light, the ground state energy shift calculated with equation 2.23 is [36]

$$\begin{aligned} \Delta E(\boldsymbol{r}, t) = &\frac{\pi c^2 \Gamma_{D1}}{2\omega_{D1}^3} \left(\frac{1}{\omega - \omega_{D1}} + \frac{1}{\omega + \omega_{D1}} \right) I(\boldsymbol{r}, t) \\ &+ \frac{\pi c^2 \Gamma_{D2}}{2\omega_{D2}^3} \left(\frac{2}{\omega - \omega_{D2}} + \frac{2}{\omega + \omega_{D2}} \right) I(\boldsymbol{r}, t)\,. \end{aligned} \tag{2.24}$$

In this chapter linear polarized light was used because for a detuning exceeding the hyperfine splitting, all magnetic sublevels of one state are shifted by the same amount. For circular polarized light the different sublevels shift differently and only for much larger detunings, this can be neglected [36].

The scaling of the scattering rate and the dipole potential with respect to the detuning stays the same as in the classical treatment. So the same rules for small heating rates and deep potentials apply: large detunings combined with high laser power.

2.3 ZEEMAN SHIFT

For slowing and trapping the atoms, it is important to understand the dependency of the energy levels of the atom on an external magnetic field. The interaction is described by the Hamiltonian

$$\mathcal{H}_B = \frac{\mu_B}{\hbar} (g_S \boldsymbol{S} + g_L \boldsymbol{L} + g_I \boldsymbol{I}) \cdot \boldsymbol{B} \tag{2.25}$$

with μ_B the Bohr magneton, $\boldsymbol{S}$ the total electron spin, $\boldsymbol{L}$ the total angular momentum and $\boldsymbol{I}$ the momentum spin of the core. The Landé factor for the electron spin g_S is close to 2 and has been measured with high precision. The electron orbital Landé factor g_L is approximately 1. A correction for the finite nuclear mass is given by

$$g_L = 1 - \frac{m_e}{m_{nuc}}\,, \tag{2.26}$$

where m_e is the electron mass and m_{nuc} is the mass of the atomic nucleus [39]. A higher precision is not required to calculate the magnetic field for the Zeeman slower. For the nuclear g-factor the complex structure of the nucleus has to be taken into account and measured values are used.

The fine structure of an atom is the result of the coupling between the spin $\boldsymbol{S}$ and the angular momentum $\boldsymbol{L}$ to a total angular momentum of $\boldsymbol{J} = \boldsymbol{S} + \boldsymbol{L}$. If the energy shift in the external magnetic field is weaker than the coupling, J (describing the magnitude of $\boldsymbol{J}$) is a good quantum number and the Hamiltonian simplifies to

$$\mathcal{H}_{B,\text{strong}} = \frac{\mu_B}{\hbar}(g_J J_z + g_I I_z) \cdot B_z \, . \tag{2.27}$$

The quantization axis was chosen to point in the direction of the magnetic field (z-direction). The Landé factor g_J is given by

$$g_J = g_L \frac{J(J+1) - S(S+1) + L(L+1)}{2J(J+1)} + g_S \frac{J(J+1) + S(S+1) - L(L+1)}{2J(J+1)} \, . \tag{2.28}$$

In the same manner the total electron angular momentum $\boldsymbol{J}$ and the angular momentum of the core $\boldsymbol{I}$ can couple, which gives a total angular momentum of

$$\boldsymbol{F} = \boldsymbol{J} + \boldsymbol{I}. \tag{2.29}$$

The quantum number F describes the magnitude of $|\boldsymbol{F}| = \hbar\sqrt{F(F+1)}$ and defines m_F the projection on the quantization axis. F is conserved as long as the coupling to external fields is smaller than the coupling of J and I. This means, the energyshift caused by the external field must be smaller than the hyperfine splitting. The Hamiltonian then becomes

$$\mathcal{H}_{B,\text{weak}} = \frac{\mu_B}{\hbar} g_F F_z B_z \tag{2.30}$$

with a hyperfine Landé factor in the weak magnetic field regime which can be calculated similarly to g_J

$$g_F = g_J \frac{F(F+1) - I(I+1) + J(J+1)}{2F(F+1)} + g_I \frac{F(F+1) + I(I+1) - J(J+1)}{2F(F+1)} . \tag{2.31}$$

The second term is often neglected because the core Landé factor $g_I \simeq g_J \times 10^{-3}$ is very small compared to the total electron Landé factor.

With perturbation theory, it is possible to calculate the energy shift of the zero field hyperfine eigenstates. In lowest order this gives a

ELEMENT	CONSTANT	VALUE [MHZ]	REF.
^{6}Li	$A_{5^2S_{1/2}}$	152.136	[41]
^{6}Li	$A_{5^2P_{3/2}}$	−1.155	[41]
^{6}Li	$B_{5^2P_{3/2}}$	−0.10	[41]
^{87}Rb	$A_{5^2S_{1/2}}$	3417.341	[42]
^{87}Rb	$A_{5^2P_{3/2}}$	84.7185(20)	[43]
^{87}Rb	$B_{5^2P_{3/2}}$	12.4965(37)	[43]

Table 2.1: The magnetic dipole and quadrupole constants of ^{6}Li and ^{87}Rb.

linear energy shift proportional to the magnetic quantum number m_F

$$E^{HFS}_{Zeeman} = \mu_B g_F m_F B, \tag{2.32}$$

which breaks the degeneracy of the different m_F eigenstates.

The same can be done for equation 2.27 in the high field regime, which would give an energy shift

$$E^{HFS}_{PB} = \mu_B (g_J m_J + g_I m_I) B \tag{2.33}$$

proportional to m_J and m_I instead of m_F. In the lithium $2^2P_{3/2}$ state, the so called *hyperfine Paschen-Back regime* is already entered at magnetic fields greater $\approx 3\,G$. Hence we will have a look at a more detailed treatment. In a high magnetic field, the hyperfine Hamiltonian

$$\mathcal{H}_{HFS} = A_{HFS}\frac{\boldsymbol{I}\cdot\boldsymbol{J}}{\hbar^2} + B_{HFS}\frac{\frac{3}{\hbar^2}(\boldsymbol{I}\cdot\boldsymbol{J})^2 + \frac{3}{2\hbar}(\boldsymbol{I}\cdot\boldsymbol{J}) - I(I+1)J(J+1)}{2I(2I-1)J(2J-1)}, \tag{2.34}$$

with the magnetic dipole constant A_{HFS} and the magnetic quadrupole constant B_{HFS} (listed in table 2.1), can be treated as a perturbation to the high field eigenstates [40].

In first order perturbation theory, the energy shift is

$$E^{HFS}_{PB} = (g_J m_J + g_I m_I)\mu_B B + A_{HFS} m_I m_J + B_{HFS}\frac{9(m_I m_J)^2 - 3J(J+1)m_I^2 - 3I(I+1)m_J^2 + I(I+1)J(J+1)}{4J(2J-1)I(2I-1)}. \tag{2.35}$$

The hyperfine Hamiltonian contribution to the energy shift is independent of the magnetic field, but for the correct splittings of the levels, the hyperfine interaction cannot be dropped.

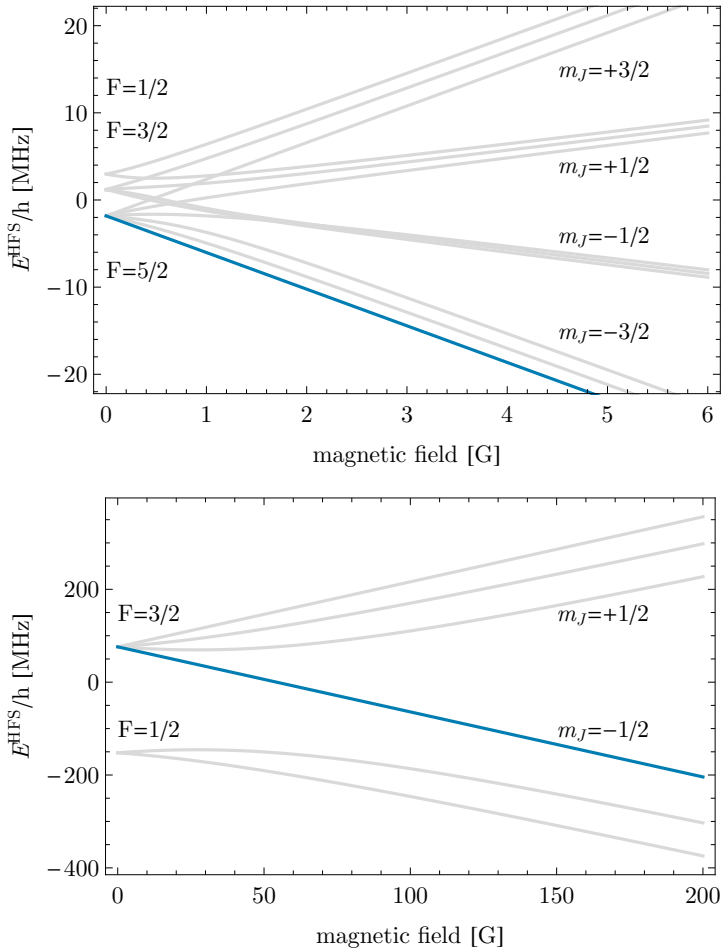

Figure 2.3: The hyperfine splitting of lithium 6 in a magnetic field. The magnetic field mixes the eigenstates of the zero field Hamiltonian and the eigen energies are shifted. In the upper figure the $2^2P_{3/2}$ excited state is shown and below the $2^2S_{1/2}$ ground state is plotted. Colored lines represent the states used for optical cooling. The calculations were done numerically.

Note that very strong magnetic fields can result in further effects, for example if the coupling between $\boldsymbol{S}$ and $\boldsymbol{L}$ is weaker than the coupling to the magnetic field. In even stronger fields also the coupling of the electric dipole of the atom starts to interact with the magnetic field which leads to the quadratic Zeeman effect. These effects do not play a role for this thesis and will not be explained here, but a detailed treatment can be found in [44].

Until now, only the low and high field regime is characterized. The intermediate regime is more difficult to describe and has to be treated numerically. Only for the ground state manifold of the alkali metal

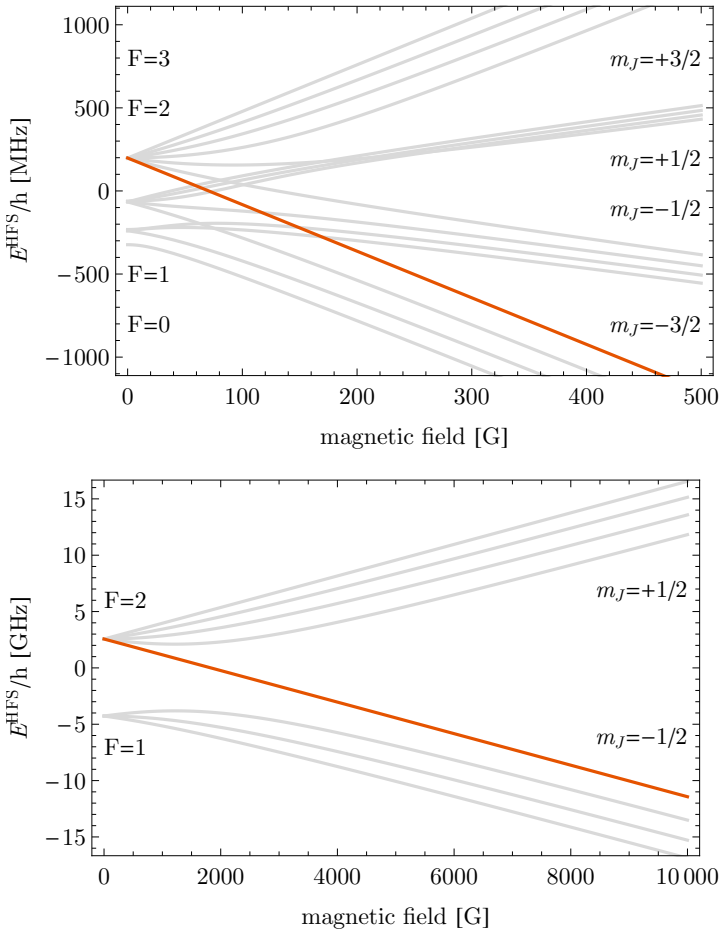

Figure 2.4: The hyperfine splitting of rubidium 87 in a magnetic field. The magnetic field mixes the eigenstates of the zero field Hamiltonian and the eigen energies are shiftet. In the upper plot the $5^2P_{3/2}$ excited state is shown and below the $5^2S_{1/2}$ ground state is plotted. Colored lines represent the states used for optical cooling. The calculations were done numerically.

atoms, the Breit-Rabi formula can used for the hole range of the magnetic field[45]

$$E^{HFS} = -\frac{\Delta E_0}{2(2I+1)} - m g_I \mu_B B \pm \frac{\Delta E_0}{2} \cdot \sqrt{1 + \frac{4m}{2I+1} x + x^2} \tag{2.36}$$

with

$$x = \frac{g_J - g_I}{\Delta E_0} \mu_B B \tag{2.37}$$

and ΔE_0 being the hyperfine splitting of the two ground state hyperfine states.

The hyperfine splitting of lithium 6 and rubidium 87 in a magnetic field is depicted in figure 2.3 and figure 2.4 which was calculated numerically. This can be done by calculating the hyperfine and the

B-field interaction Hamiltonian in their respective eigenstates. With Clebsch-Gordan coefficients one of these can be transferred into the basis of the other Hamiltonian and then the total Hamiltonian can be diagonalized. In both figures the levels of the cooling transition are marked. In lithium 6 the $\left|F = \frac{3}{2}, m_F = -\frac{3}{2}\right\rangle$ to $\left|F' = \frac{5}{2}, m_{F'} = -\frac{5}{2}\right\rangle$ is used. Whereas for rubidium 87 the cooling transition is $|F = 2, m_F = -2\rangle$ to $|F' = 3, m_{F'} = -3\rangle$. Because the energies of both, the lower and upper leves, are shifted, the difference of the shift is from interest for laser cooling. For the Zeeman regime the shift of the energy difference is

$$\begin{aligned} \Delta E^{HFS}_{Zeeman} &= (g^{ex}_F m^{ex}_F - g^g_F m^g_F)\mu_B B \\ &= \mu_{eff} B, \end{aligned} \tag{2.38}$$

whereas for the Paschen-Back regime the shift is

$$\begin{aligned} \Delta E^{HFS}_{PB} &= (g^{ex}_J m^{ex}_J - g^g_J m^g_J)\mu_B B \\ &\quad + (A^{ex}_{HFS} m^{ex}_I m^{ex}_J - A^g_{HFS} m^g_I m^g_J). \\ &= \mu_{eff} B + E_{off} \end{aligned} \tag{2.39}$$

In the case of rubidium and lithium the states used for cooling shift linearly with the magnetic field. These so called stretched states do not mix with the other states, if a magnetic field is applied. Looking at figure 2.4 and figure 2.3 one can see, that for the complete range of magnetic fields in our setup (up to 700 G in the Zeeman slower) equation 2.38 can be used. The effective magnetic moment for the cooling transitions in Rubidium and Lithium is $\mu_{eff} = -\mu_B$.

2.4 ZEEMAN SLOWER

When the atoms leave the oven, they have a modified Maxwell-Boltzmann velocity distribution [46]. For rubidium with an oven temperature of 170 °C, the mean velocity is 360 m/s. That means, that only a fraction of 10^{-6} of all atoms would be captured in a magneto optical trap with a typical capture velocity of 40 m/s. To achieve a higher number of atoms with low velocities one could reduce the oven temperature, but at the same time, the vapour pressure would decrease and the total atomic flux as well. The other solution is, to slow the fast atoms using the scattering force of light (see section 2.2.1). To slow down a rubidium atom from 300 m/s to 20 m/s, it has to scatter about $\frac{m_{Rb} \cdot \Delta v}{\hbar k} = 5 \times 10^4$ photons. Here k is the wave vector and v the velocity of the atom. With a narrow band laser, a Doppler shift on the order of the natural line width Γ of the employed transition brings atoms initially resonant out of resonance and leads to a strong decrease of the slowing force. This corresponds to a velocity change of $\Delta v = \frac{\Gamma}{k} = 4.5\,\text{m/s}$. To be able to scatter many photons in a short time, one has to compensate the Doppler shift and optical pumping to dark states, which cannot be accessed by the slowing laser.

To overcome this problem, a time dependent frequency shift of the laser can be used. This is known as chirp cooling, where the frequency of the slowing light is changed to stay in resonance, with the slowing atoms [47]. Another concept is the use of a very broadband light source to stay always resonant with the atoms, but this requires high intensities of the light. A third concept is the Zeeman slower [15], which is used in this experiment and described in this chapter.

The Zeeman slower produces an inhomogeneous magnetic field along the flight direction of the atoms, which shifts the atomic levels via the Zeeman effect (see section 2.3) depending on the position in the slower. This makes it possible to cancel the Doppler shift $\delta_{\text{Doppler}} = vk$ for a wide range of velocities. The effective detuning of the light is

$$\delta_{\text{eff}} = \delta_0 + \delta_{\text{Doppler}} + \frac{\Delta E}{\hbar} = \omega - \omega_0 + v \cdot k + \frac{\mu_{\text{eff}} B}{\hbar}, \tag{2.40}$$

where δ_0 is the difference between the transition frequency ω_0 at zero magnetic field and the laser frequency ω and ΔE is the differential energy shift of the ground and excited states caused by the Zeeman effect. The effective magnetic moment $\mu_{\text{eff}} = \mu_B(g_e m_e - g_g m_g)$ depends on the Landé factor g_i and the magnetic quantum numbers m_i of the excited and the ground state (see section 2.3).

For a constant deceleration a, the velocity of the atom in the Zeeman slower is given by

$$v(z) = \sqrt{v_0^2 - 2az}\,. \tag{2.41}$$

Combining equation 2.40 and equation 2.41 the spatial dependence of the magnetic field is

$$B(z) = \frac{\hbar}{\mu}(\delta_0 + k\sqrt{v_0^2 - 2az}). \tag{2.42}$$

A constant deceleration a also fixes the required stopping distance of

$$L_0 = \frac{v_0^2 - v_{\text{end}}^2}{a} \tag{2.43}$$

for a maximum capture velocity v_0 and end velocity v_{end}. With the maximum deceleration for rubidium $a_{\text{max, Rb}} = 112 \times 10^3\,\text{m/s}^2$ this implies a stop after 0.4 m for small end velocities. Due to its lighter mass, lithium can be slowed on an even shorter distance.

In principle there are three possibilities for the realization of the Zeeman slower. The magnetic fields of these different types are shown in figure 2.5.

In the first case the light is resonant with the atoms at rest ($\delta_0 = 0$) and the magnetic field at the beginning of the slower shifts the energy

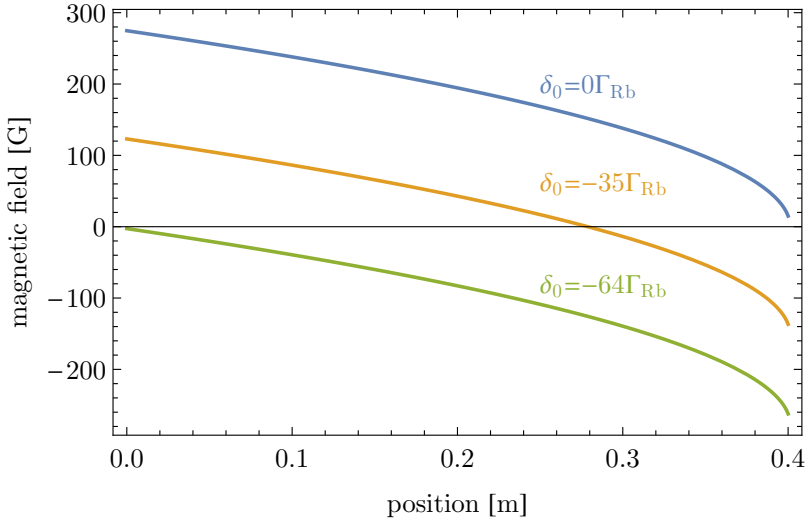

Figure 2.5: The theoretical optimum magnetic field of a Zeeman slower calculated for rubidium 87 with a maximum capture velocity of 300 m/s. The theoretical maximum acceleration achievable by the scattering force was assumed. Three different detunings of the slowing light are used. Increasing field Zeeman slower in blue with zero detuning. A detuning of -35Γ for a spin flip Zeeman slower and -64Γ for an increasing field version (increasing with respect to the absolute of the field).

levels to compensate the Doppler shift for the fastest atoms. This implies that the maximum magnetic field value selects the maximum velocity which can be slowed. With decreasing velocity, also the magnetic field has to become smaller. This *decreasing field Zeeman slower* has the advantage, that close to the magneto-optical trap, the magnetic field is small and only little compensation is needed to cancel stray magnetic fields. These could otherwise disturb efficient cooling (e. g. optical molasses cooling) and measurements, where good control over the magnetic field is needed. Also less heat is produced near the experiment chamber. A disadvantage, however, is the small detuning of the slowing light to the cooling transition for atoms at rest in zero magnetic field. Because of geometric reasons the slowing light has to pass the trapped atoms in the MOT to counter propagate relative to the incoming atoms. This heats the sample because of the scattering of photons and less light will be available in the slower to decelerate atoms.

The *spin flip Zeeman slower* is another possible realization. The magnetic field starts at a lower value than the decreasing field configuration. This means the slower light has to be red detuned from resonance. At some point in the slower the magnetic field crosses zero. The position of the zero crossing is determined by the detuning δ_0 as one can see in equation 2.42. A larger detuning shifts the zero cross-

ing to the beginning of the slower. The advantage of this concept is a lower maximum magnetic field, which simplifies the construction because it requires less current. A drawback of this design is the larger region of small magnetic fields. In the case of lithium the cooling transition is closed for magnetic fields exceeding 100 G. In smaller fields, however, this is not the case anymore. Especially in the intermediate regime between the Zeeman regime and the Paschen-Back regime, their cooling transitions are not closed and transitions into the dark state $\left|2^2S_{1/2}F=\frac{1}{2}\right\rangle$ are possible. In general, a repumper laser is used to pump the atoms back to the bright $\left|2^2S_{1/2}F=\frac{3}{2}\right\rangle$ state. However, the effective magnetic moment μ_{eff} (see equation 2.38 and equation 2.39) for the repumping transition is different to that of the slowing transition. This makes it impossible to keep the repumper beam on resonance over the total magnetic field range. In a spin flip Zeeman slower the region with absolute magnetic fields smaller than a hundred Gauss is twice as large as in the other two configurations and there is more time for atoms to decay into dark states.

In an *increasing field Zeeman slower* the detuning of the light is as large as the Doppler shift of the fastest atoms being captured. The absolute value of the magnetic field has then the highest value close to the MOT. This results in a stronger residual magnetic field in the region, where the atoms are trapped and cooled. As a consequence one needs an additional compensation coil. In this experiment, the chamber design sets a minimum distance of approximately 12 cm between the end of the slower and the center of the MOT. Therefore the leaking field is not a major problem in our case and can be compensated. In contrast to the decreasing Zeeman slower, the light is far detuned for atoms in the MOT. For lithium and rubidium the calculated detuning in the final design is around

$$\delta_0^{\text{Rb }87} = 875\,\text{MHz} \approx 144\,\Gamma$$
$$\delta_0^{\text{Li }6} = 1.1\,\text{GHz} \approx 177\,\Gamma.$$

For these detunings, the influence of the slowing light on the trapped atoms can be neglected. Another benefit is, that atoms fall out of resonance very quickly after they leave the Zeeman slower. This ensures that the atoms are not further slowed down and eventually get accelerated back to the oven. As a consequence of the above points, we decided to use the increasing field design for the Zeeman slower.

As mentioned in section 2.2.1, the scattering force has a maximum value because of the finite scattering rate. This limits the maximum deceleration and constrains the minimal length of a Zeeman slower. Hence there exists a maximum allowed gradient of the magnetic field,

which is often expressed with the so-called adiabatic slowing criteria. It is derived by differentiating equation 2.40

$$\left|\frac{\partial B(z)}{\partial z}\right| < \frac{\hbar k a_{max}}{\mu_{eff} v(z)}, \tag{2.44}$$

where $a = v\frac{\partial v}{\partial z}$ was used. For the construction of Zeeman slowers a fraction of the maximum acceleration $a_{eff} = \eta a_{max}$ is used for several reasons. First, the scattering of photons is random and the time between two scattering events varies. A gradient too close to the maximum would rise the chance, that between two scattering events an atom flies out of the region where the adiabatic slowing condition is fulfilled. This means that the magnetic field shifts the cooling transition out of resonance. Second, the Zeeman slower coil cannot be produced perfectly, which results in unevenness in the magnetic field. And third, current fluctuations cause noise in the magnetic field, causing field variations, which could lead to violations of the adiabatic slowing condition. All this could increase the gradient to much, and all atoms slowed before such a point, would fall out of resonance and would be lost for the cooling.

2.5 OPTICAL MOLASSES

The Zeeman slower described in section 2.4 uses the scattering force to slow down the atomic beam in one direction. However, in a trapped gas, the movement of the atoms is in all directions. Using counter propagating laser beam pairs on three orthogonal axes is one possible solution to cool the atoms in all three spatial directions. Since the frictional like force acting on the atom is similar to the force experienced by a particle in honey or any other viscous fluid, this technique is called *optical molasses* [16]. In figure 2.6 this is illustrated for an atom and one spatial dimension. For a moving atom, a red detuned laser gives an imbalance in the number of scattered photons of each beam. In the reference frame of the atom the laser beam frequency is increased, if it is moving towards the beam and the frequency is closer to the resonance. The number of scattered photons increases as opposed to the scattered photons of the other beam. The total force acting on an atom in light beams with wave vector k and $-k$ is

$$\begin{aligned} F_{molasses} &= F(\omega - \omega_0 - kv) - F(\omega - \omega_0 + kv) && (2.45)\\ &= \hbar k \frac{\Gamma}{2} \frac{s_0}{1 + s_0 + (2\frac{\delta_0 - k\cdot v}{\Gamma})^2} \\ &\quad - \hbar k \frac{\Gamma}{2} \frac{s_0}{1 + s_0 + (2\frac{\delta_0 + k\cdot v}{\Gamma})^2} && (2.46)\\ &\overset{kv \ll \Gamma}{\simeq} -4\hbar k^2 s_0 \frac{-2\delta_0/\Gamma}{(1 + s_0 + (2\delta_0/\Gamma)^2)^2} v = -\zeta v && (2.47) \end{aligned}$$

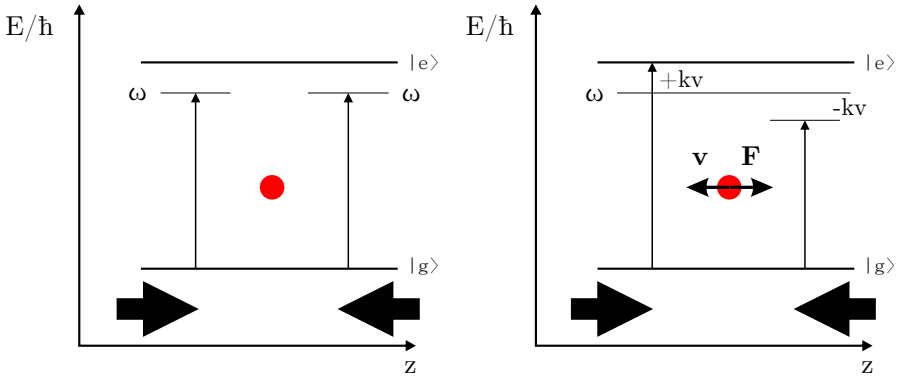

Figure 2.6: Principle of a one dimensional optical molasses of a two level system. (a) For an atom at rest both lasers (thick black arrows) are detuned by the same amount from resonance. (b) For a moving atom with velocity $\boldsymbol{v}$, the detuning of each laser beam is different because of the Doppler shift kv. This difference causes a force $\boldsymbol{F}$ contrary to the velocity.

with drag constant ζ. The linearization in equation 2.47 is only valid for Doppler shifts smaller than the line width ($k \cdot v \ll \Gamma$). Furthermore, the whole treatment above is only valid for intensities well below the saturation intensity. Otherwise stimulated emission cannot be neglected and the forces are not independent of each other anymore [37]. The molasses force (equation 2.45) is frictional for a red detuning of the light ($\delta_0 = \omega - \omega_0 < 0$) and leads to a damped motion of the atoms. In figure 2.7 the force is plotted for velocities of $-2\Gamma/k$ to $2\Gamma/k$, a detuning of $\delta_0 = -1/2\Gamma$ and a saturation parameter $s_0 = 1/10$. In addition the force of each beam is plotted in dashed lines separately.

The maximum damping in a molasses is achieved for a maximum of ζ at a detuning of $\delta_0 = -\Gamma/(2\sqrt{3})$. As we will see in equation 2.50, the minimum temperature is not achieved with the maximum damping coefficient. From figure 2.6 and figure 2.7 one can already see that the cooling mechanism only works for a certain velocity range of $\pm\delta/k \simeq \pm\Gamma/k$. For rubidium 87 this is in the order of $\pm 5\,m/s$ and $\pm 4\,m/s$ for lithium. Thus only already slow atoms can be cooled with this technique. Furthermore there is no spatial confinement (the force depends only on the velocity) which makes it not suitable to capture atoms at the end of a Zeeman slower. This obstacle can be overcome by the magneto-optical trap, which is used and explained in section 2.6.

From the simple model introduced above, it looks like the movement of the atoms is completely damped away, which is not the case in a real system. That is, because only the average force was considered in the model. The fluctuations of the force lead to heating of the sample, caused by the gained momentum $\hbar k$ of emitted photons,

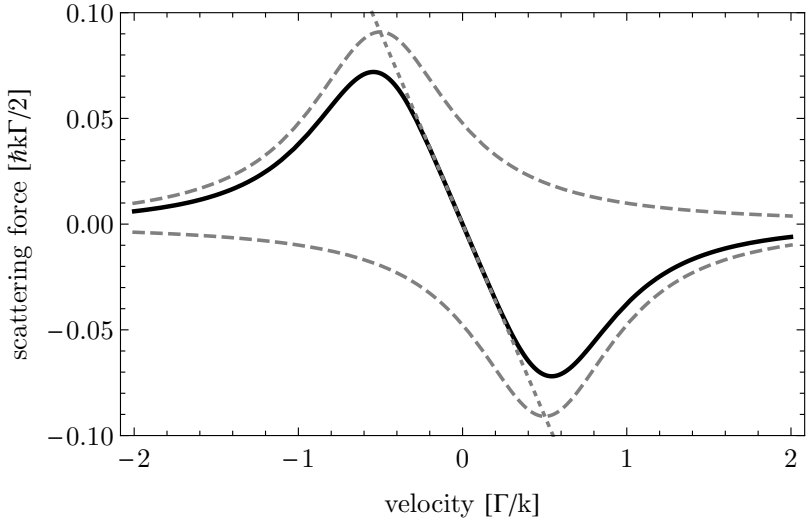

Figure 2.7: The velocity dependent total force in the one dimensional molasses is plotted in a black solid line. The dashed gray lines represent the force of each light beam with wave vectors $\pm k$. The detuning is $\delta_0 = -1/2\Gamma$ and the light intensity in each beam is $1/10$ of the saturation intensity. The dotted gray line is the linearized force expressed in equation 2.47.

which leads to a random walk in momentum space. In other words, the atom gains the recoil energy each time it emits a photon

$$E_{rec} = \frac{\hbar^2 k^2}{2m} = \hbar\omega_r \, . \tag{2.48}$$

The emission of the photons is determined by the scattering rate Γ_{sc}, which gives an expression for the heating rate

$$\dot{E}_{heat} = 2 \cdot \hbar\omega_r \Gamma_{sc} = \hbar\omega_r \Gamma \frac{s_0}{1 + \frac{4\Delta^2}{\Gamma^2} + s_0}. \tag{2.49}$$

The factor of 2 arises, since there are two counter propagating laser beams involved in the process. This heating process prevents a reduction of the atomic velocity to zero and limits the minimum temperature of the sample. In the steady state, the cooling rate $\dot{E}_{cool} = F_{molasses} \cdot v$ and the heating rate should be equal and the temperature can be estimated by

$$k_B T = \frac{\hbar\Gamma}{4} \frac{1 + (2\delta/\Gamma)^2}{-2\delta/\Gamma}. \tag{2.50}$$

A detuning of $\delta = -\Gamma/2$ minimizes the temperature to the so called Doppler temperature

$$T_D = \frac{\hbar\Gamma}{2k_B}. \tag{2.51}$$

For lithium 6 and rubidium 87 the Doppler temperature for the D_2-line is around $T_D \approx 140\ \mu K$.

In experiments it turned out, that laser cooling can achieve temperatures well below the Doppler limit, because the assumption of two independent light beams oversimplifies the system. The two circular polarized counter propagating light beams form a position dependent polarization direction. A moving atom has then a difference in the scattering probability of photons from the two beams [48]. This mechanism cools the atoms to temperatures close to the recoil temperature

$$T_{rec} = \frac{(\hbar k)^2}{2 k_B m} = \frac{E_{rec}}{k_B}. \tag{2.52}$$

The momentum of the photon $\hbar k$ transferred to the atom in the scattering process defines the lower limit. Because of its small mass, lithium has a very high recoil temperature of 3.5 µK compared to the heavier alkalies like rubidium with $T_{rec} = 362\,\mathrm{nK}$. A different cooling mechanism with two perpendicular polarized laser beams (polarization gradient cooling) also have the recoil temperature as a limit [48].

2.6 MAGNETO-OPTICAL TRAP

The optical molasses technique described in section 2.5 is very efficient for cooling atoms. However, the force which acts on the atoms does only have a velocity dependent component. To trap atoms in space, a spatial dependent force is required. It turns out that with a simple magnetic field configuration and the same laser setup as in the optical molasses, this requirement can be fulfilled. Hence the name *magneto-optical trap* (MOT), which was first experimentally realized in 1987 by Raab et al. [49]. In the following section, the principle and characteristics are explained. A magnetic field gradient produces a spatial dependent splitting of the different magnetic hyperfine sublevels of the atom (see equation 2.38). This by itself does not confine the atoms as it is done in magnetic traps, because of the much smaller gradients. However the energy shift makes the scattering rate dependent on the position of the atom and the polarization of the light, because the effective detuning of the light from resonance includes the Zeeman shift (see equation 2.40). In an experiment the magnetic field is produced by two coils in anti-Helmholtz configuration as shown in figure 2.8. The trapping mechanism is illustrated for one dimension in figure 2.9. A two level atom with ground state $|F = 0\rangle$ and excited state $|F = 1\rangle$ ($g_F > 0$) is placed at a distance $z' > 0$ from the center of the MOT. The linear increasing magnetic field shifts the excited $|F = 1\, m_F = 1\rangle$ state further away from the resonance in contrast to the $|F = 1\, m_F = -1\rangle$ state, which gets closer. The counter-propagating laser beams with σ^+ and σ^- polarization and a red detuning have now different scattering probabilities. A photon of the σ^- laser beam is more likely absorbed than one of the σ^+ beam. This pushes the

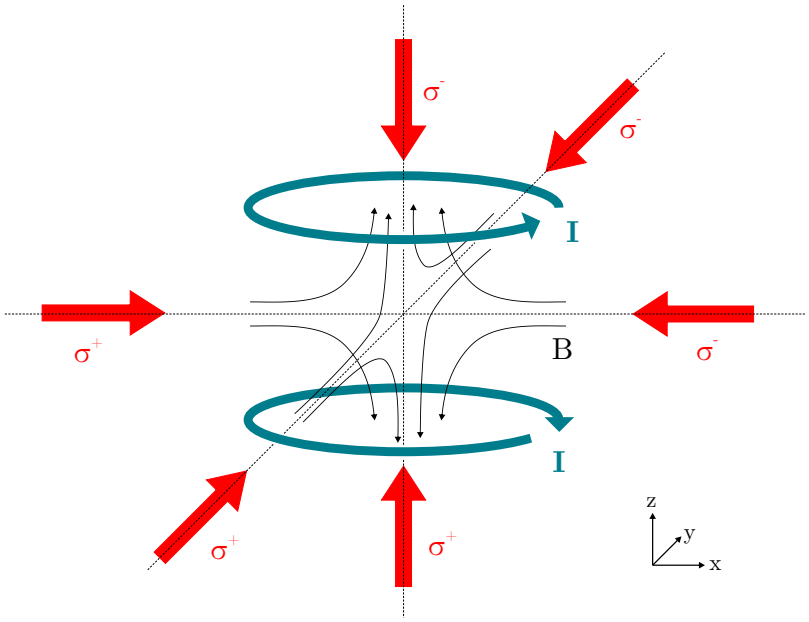

Figure 2.8: Model of a three dimensional MOT. Two coils in anti-Helmholtz configuration, symbolized by the blue arrows, provide a magnetic quadrupole field (black arrows). The trapping force is generated by three counter propagating pairs of $\sigma^{\pm}$ polarized laser beams.

atom towards the center of the MOT. It is worth noting that this is not only working for a $|F = 0, m_F = 0\rangle \rightarrow |F' = 1, \Delta m_{F'} = \pm 1\rangle$ transition but for any other $|F\rangle \rightarrow |F' = F + 1\rangle$ transition as atoms get pumped to states with maximum $|m_F|$, forming a closed cooling transition. For a position $z' < 0$ the situation is converse. Photons of the σ^+ beam have a higher probability to scatter as photons of the σ^- beam and the force is pointing still to the trap center. The resulting force for small Doppler and Zeeman shifts ($\delta_0 \gg |kv| + |\mu_{eff} B/\hbar|$) is then

$$F_{MOT} = -\zeta v - \kappa z \tag{2.53}$$

with a spring constant of

$$\kappa = \frac{\mu_{eff}}{\hbar k} \frac{\partial B}{\partial z} \zeta \,. \tag{2.54}$$

The damping coefficient

$$\zeta = 4\hbar k^2 s_0 \frac{-2\delta/\Gamma}{\left(1 + s_0 + (2\delta/\Gamma)^2\right)^2} \tag{2.55}$$

is already known from equation 2.47. The equation 2.53 describes a damped harmonic oscillator with a oscillator frequency of

$$\omega_{osc} = \sqrt{\frac{\kappa}{m}}. \tag{2.56}$$

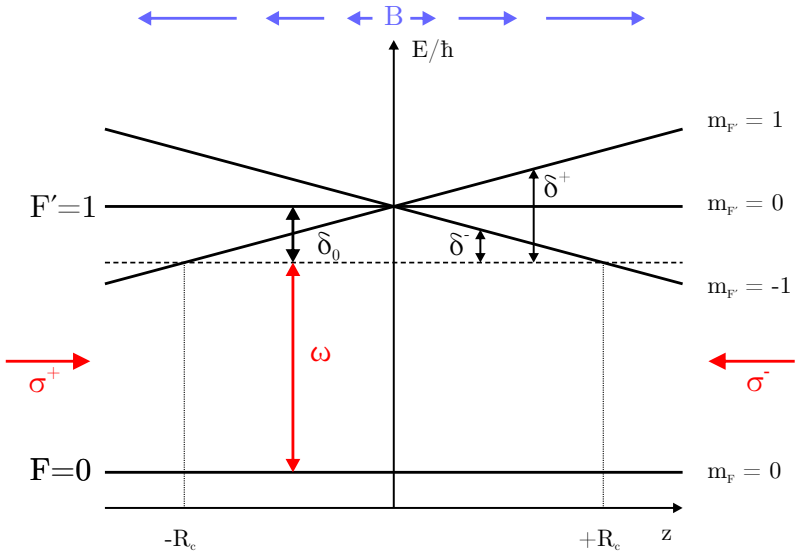

Figure 2.9: Modell of a one dimensional magneto-optical trap for a system with ground state $F = 0$ and an excited state $F = 1$. The magnetic field has a linear gradient in z-direction and is zero at the center. Shifts the energy levels (Zeeman effect). The two counter propagating circular polarized beams have a frequency $\omega = \omega_0 + \delta_0$. At a distance of the capture range R_c, the Zeeman shift is the same as the detuning of the lasers.

Because the damping rate $\beta = \zeta/(2m)$ is much higher than the oscillator frequency, the atomic motion in the MOT is over damped. For example typical values for a lithium MOT with $\delta = 2\Gamma$, $s_0 = 4$, $\partial_z B_z = 15\,\mathrm{G/cm}$ and $\mu_{\mathrm{eff}} = \mu_B$ result in a oscillation frequency of $\omega_{\mathrm{osc}} = 4.4 \times 10^4\,\mathrm{s}^{-1}$ and $\beta = 6.7 \times 10^5\,\mathrm{s}^{-1}$.

Compared to the optical molasses the temperature in a MOT is higher. This has mainly two reasons. For the sub Doppler cooling effects one needs very good compensation of the magnetic fields. Even the weak earth magnetic field with about 0.5 G is already disturbing this process because the Zeeman shift exceeds the light shift. Second the density in a MOT is high and a lot of light gets absorbed and scattered. In this high densities multiphoton scattering processes can heat the atomic cloud [50, 51].

2.6.1 *Capture range and velocity*

The maximum possible distance from the MOT center to capture an atom is defined as the capture range R_c. At the capture range, the Zeeman shifts brings the atom at rest in resonance with one of the two beams:

$$R_c = \frac{\hbar\delta_0}{\mu\frac{\partial B}{\partial z}}. \tag{2.57}$$

The magnetic quadrupole field gradient in the experimental setup is not the same in all directions. In axial direction of the coils the gradient is two times larger than in the radial direction due to Maxwell equations:

$$\mathrm{div}\boldsymbol{B} = \frac{\partial B_x}{\partial x} + \frac{\partial B_y}{\partial y} + \frac{\partial B_z}{\partial z} = 0$$

When choosing the z-axis as the axial direction and x,y as the radial directions of the coil this leads to

$$\frac{\partial B_z}{\partial z} = -2 \cdot \frac{\partial B_r}{\partial r} \, .$$

The gradient in x and y direction have to be the same due to symmetry reasons. This causes different capture ranges for the different axes. A second important quantity is the maximum velocity of an atom to be captured in the MOT. This means that an atom at $-R_c$ has to have such a low kinetic energy that it is stopped until it reaches $+R_c$. This limits the maximum velocity to

$$v_c = \sqrt{2E_{kin}/m} = \sqrt{\frac{4F_{max}R_c}{m}} \, . \tag{2.58}$$

A larger capture range makes it possible to catch more atoms from the diverging atomic beam after the Zeeman slower, increasing the loading rate of the MOT. For the same number of atoms, a bigger MOT allows lower densities which reduces two body losses. For beam waists smaller than the capture range, the restriction of the atomic cloud is given by the beam size. A higher capture velocity has also several advantages. The atoms leaving the Zeeman slower can be faster, which reduces the spread of the atoms before they reach the center of the MOT. Also more atoms which gain energy due to inelastic collisions can be trapped in a MOT with higher capture velocity.

2.7 DIPOLE TRAP

In cold atom experiments it is common to transfer the atoms from the MOT to a magnetic trap or an optical trap to avoid the limitations for the temperature by spontaneous emission and density limitations by radiation trapping effects [52]. With the ability to modify the beam shape of the laser beam, optical dipole traps allow a great number of trap shapes, for example double well potentials, one or two dimensional shaped systems or crystal-like structures.

In contrast to magnetic traps, optical dipole traps provide a trapping potential for all magnetic substates of an atomic species, whereas magnetic traps confine only low field seeking states. This offers the opportunity to trap in the lowest magnetic hyperfine state (which is always high-field seeking) to avoid inelastic collisions. It also keeps

the possibility open, to use the magnetic field as an additional tool for accessing Feshbach resonances.

Evaporative cooling in optical traps offers an easy method to increase the phase space density in order to reach low temperatures up to degeneracy. The Zeeman slower and the MOT are still important to provide good starting conditions with high numbers of precooled atoms for more efficient and faster cooling.

2.7.1 *Single beam trap*

A single focused Gaussian laser beam is one of the simplest realizations of a dipole trap. With red detuned light of power P propagating along the z-axes the atoms are soaked into the intensity maximum (see section 2.2.2) which is given by the beam profile

$$I(z,\rho) = \frac{2P}{\pi w^2(z)} \exp\left(-2\frac{\rho^2}{w^2(z)}\right) \tag{2.59}$$

with ρ as the radial distance to the z-axes and the $1/e^2$ radius

$$w(z) = w_0\sqrt{1+\frac{z^2}{z_R^2}}.$$

The waist minimum is given by w_0 and the Rayleigh length is denoted by $z_R = \pi w_0^2/\lambda$. A relation to the potential is given by equation 2.20. For small dimensions of the cloud ($z, \rho \ll z_R, w_0$) which means a thermal energy smaller than the trap depth U_0, the potential can be simplified by a Taylor expansion and approximate as a harmonic potential

$$U(r,\rho) \approx -U_0\left(1-2\frac{r^2}{w_0^2}-\frac{z^2}{z_R^2}\right). \tag{2.60}$$

The trap depth is given by the deepest value of the potential at $z, \rho = 0$ and the radial and axial trapping frequencies

$$\omega_r = \sqrt{4U_o/(mw_0^2)} \tag{2.61}$$

$$\omega_z = \sqrt{2U_o/(mz_R^2)}\,. \tag{2.62}$$

2.7.2 *Evaporative cooling*

To reach temperatures cold enough to generate Bose-Einstein condensates and degenerate Fermi gases, the standard technique is evaporative cooling. Its fundamental principle, also well known for example from a cup of tee, is based on the removal of the hottest (fastest) atoms of the cloud, in atomic physics by lowering of the trap depth and the rethermalization of the remaining ones via elastic scattering.

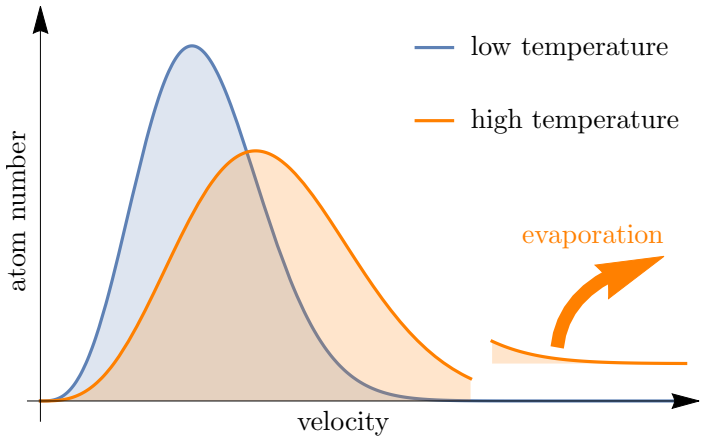

(a) Atom number versus velocity in a non interacting classical gas for two different temperatures. The evaporation can be realized by a rf-knife in magnetic traps or by lowering the trap depth of optical dipole traps.

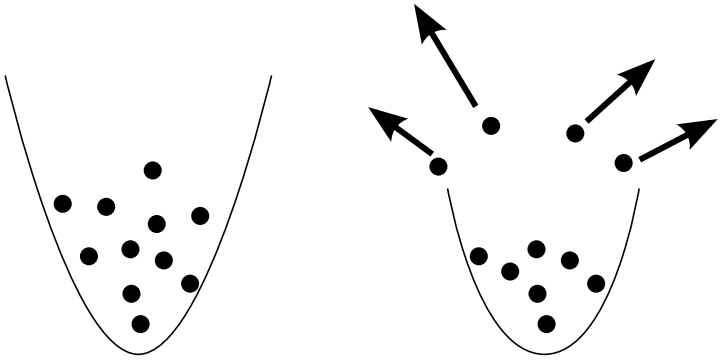

(b) Trap depth is lowered in dipole traps to enable the atoms with highest energy to escape from the trap.

Figure 2.10: Principle of evaporative cooling. Atoms with high energy (high velocity at trap minimum) are removed from the trap. The remaining atoms rethermalize and the gas has a smaller temperature than before.

This leads to more slow atoms than before and the average kinetic energy drops, reducing the temperature of the cloud far below any temperature reachable by optical cooling.

In magnetic traps the lowering of the trap depth is done by changing the magnetic substate of the hottest atoms with a radio frequency to an untrapped state. Because the trap potential rises with the magnetic field, the fastest atoms reach the highest magnetic field. Making the rf frequency resonant to the transition at these fields removes only the fastest atoms. By changing the frequency the threshold of the evaporation can be lowered (forced evaporation). This is necessary because the probability to have atoms with an energy ε greater than the potential depth U_0 is supressed approximatly by $\exp\left(-U_0/k_B T\right)$ [53].

This means, that for smaller temperatures the evaporation process slows down, because an exponentially decaying part of the atoms is able to leave the trap. The cooling process even comes to an end, if the loss or heating rate (by scattered photons or intensity fluctuations) are on the same order. Loss can occur by three body collisions or collisions with the background gas. In optical dipole traps the evaporation threshold can be changed by lowering the power of the laser beam. However this has one important side effect. Because the trap frequencies are proportional to the square root of the trap depth (equation 2.61, 2.62), they will also decrease and make the rethermalization process slower.

2.7.3 *Scaling properties of evaporative cooling*

The scaling laws described here are results from kinetic theory, treated in detail in [53–55]. In this section the essential parts are discussed to understand the the evaporative cooling process. The assumption of a classical gas is sufficient because in most of the cases the thermal energy of the atoms is much higher than the energy level spacing of the trap. For atoms loaded from a MOT into the ODT, the phase space density

$$\rho = n\lambda_{dB} \ll 1 \tag{2.63}$$

is much smaller than one and classical behaviour can be assumed. Here $n = N/V$ is the number density with N the total number of atoms in the volume V and $\lambda_{dB} = \sqrt{2\pi\hbar/(mk_BT)}$ is the thermal de Broglie wavelength for an atom with mass m. Only at the end of the evaporation process when Bose Einstein condensation or degeneracy is reached, this model breaks down. With this assumptions a simple model gives insight in the scaling behaviour of the number of atoms N, the collision rate γ and the peak phase space density ρ_0, if the trapping potential U_0 is changed [55]. The ratio of the potential and the temperature $\eta = \frac{U_0}{k_BT}$ is in general between $6-10$ for experiments. This allows us, to approximate the potential, created by Gaussian beams with a harmonic oscillator (equation 2.60). Of course the following scaling laws are also valid for any other potential, which can be approximated by a harmonic potential.

The mean energy carried away by an evaporated atom consists of the potential energy U_0 and a kinetic part χk_BT depending on the temperature T with $0 < \chi < 1$ [53]. For temperatures small compared to the harmonic potential depth χ is given by $\chi = (\eta-5)/(\eta-4)$ [55]. This gives an energy loss rate of $\dot{E} = \dot{N}(U_0 + \zeta k_BT)$, depending on the evaporation rate of atoms $\dot{N}$ from the trap. One has to keep in mind that in this treatment, three-body losses and background gas collisions are neglected. By lowering the trap potential in a single beam optical dipole trap, the trap characteristics are changing. Thus

an adiabatic change in the potential influences the trap frequencies $\omega \propto \sqrt{U_0}$ and the mean energy of the atoms in the harmonic potential $E/2 \propto \bar{\omega}$. Here $\bar{\omega}$ is the mean trap frequency. For magnetic traps the change in trap depth does not influence the trap frequencies. This is modelled in kinetic theory with [54]

$$\dot{E}_{ad} = 3Nk_B T\frac{\dot{\bar{\omega}}}{\bar{\omega}} = \nu E\frac{\dot{U}_0}{U_0}\,. \tag{2.64}$$

The total energy E of gas in a harmonic trap is given by $E = 3Nk_B T$ in the classical limit and the parameter ν takes account for the change in the trap frequencies with respect to the potential depth. For a magnetic trap ν is zero, whereas for a harmonic trap the parameter is $1/2$. All together this results in a total energy change of

$$\dot{E} = \dot{N}\left(U_0 + \chi k_B T\right) + \nu E\frac{\dot{U}_0}{U_0}. \tag{2.65}$$

On the other hand the total energy change can be written as

$$\dot{E} = 3\dot{N}k_B T + 3Nk_B\dot{T} \tag{2.66}$$

and combined with equation 2.65 result in

$$\dot{N}\left(U_0 + \chi k_B T\right) + \nu E\frac{\dot{U}_0}{U_0} = 3Nk_B\dot{T} + 3\dot{N}k_B T. \tag{2.67}$$

Assuming a constant ratio η, which implies a fast rethermalization compared to the change in potential depth, one can arrange equation 2.67 to

$$\frac{\dot{N}}{N} = \frac{\dot{U}_0}{U_0}\frac{3-3\nu}{\eta+\chi-3}. \tag{2.68}$$

Solving this equation one get a scaling law for the atom number

$$\frac{N}{N(0)} = \left(\frac{U_0}{U_0(0)}\right)^{\frac{3-3\nu}{\eta+\chi-3}} = \left(\frac{T}{T(0)}\right)^{\frac{3-3\nu}{\eta+\chi-3}} \tag{2.69}$$

with $N(0)$, $U(0)$ and $T(0)$ as the initial atom number, trap depth and temperature. It is also important to know the scaling for the phase space density, because this quantity defines for example at which point a non interacting Bose gas undergoes the phase transition to a Bose-Einstein condensate ($\rho = 2.612$ [56]). As adiabatic expansion can cool the atoms, by definition it does not change the phase space density. Thus the parameter of interest is the phase space density and not temperature. In a classical regime, the phase space density for a harmonic potential is $\rho = N(\hbar\bar{\omega})^3/(k_B T)^3$ with $\bar{\omega}$ as the mean trap frequency. Using equation 2.69, the scaling law for is

$$\frac{\rho}{\rho(0)} = \left(\frac{U_0}{U_0(0)}\right)^{(3\nu-3)\frac{\eta+\chi-4}{\eta+\chi-3}} = \left(\frac{N}{N(0)}\right)^{4-\eta-\chi}. \tag{2.70}$$

For an η of 10, ρ scales as N^{-7}. This means that already a small number of evaporated atoms lead to a huge increase in the phase space density. This scaling gets even better for higher η.

For a fast and efficient cooling process, it is important to have a large elastic collision rate $\gamma = n_0 \sigma \bar{v}$ for the rethermalization process. The collision cross section σ is assumed to be constant in the temperature range of interest (s-wave cross section) and $\bar{v}$ is the mean relative velocity of two atoms. With the peak space density $n_0 = \rho/\lambda_{dB}$ the scaling of the elastic collision rate is

$$\frac{\gamma}{\gamma(0)} = \left(\frac{U_0}{U_0(0)}\right)^{\frac{(3\nu-1)(\eta+\chi)-12\nu+6}{\eta+\chi-3}} . \tag{2.71}$$

For a focused laser beam ($\nu = 1/2$) this equation reveals a decrease for the elastic collision rate with decreasing potential depth ($\gamma \propto (U/U(0))^{0.69}$ for $\eta = 10$). If the collision rate is to low in the beginning, the cooling process stagnates before the final desired temperature is reached. Reducing the trap depth with constant trap frequencies ($\nu = 0$) the rate increases with smaller traps $\gamma \propto (U(0)/U)^{0.63}$. This is the so called runaway regime with an increasing speed in evaporation.

2.7.4 *Realization methods of dipole traps*

As shown in section 2.7.1 it is possible to use one laser beam as a dipole trap [57]. However for evaporative cooling the large aspect ratio of the trapping frequencies

$$\frac{\omega_r}{\omega_z} = \sqrt{2}\frac{z_R}{w_0}$$

is not favourable, because it permits efficient rethermalization. The ratio is around 208 for a typical wavelength of 1064 nm and a beam waist of 50 μm. For bigger waists, the ratio increases and for effective evaporative cooling, small waists (below 50 μm) are necessary to ensure high atomic densities. On the other hand, a small waist means little overlap of the dipole trap with the MOT, hence inefficient transfer of the atoms.

A very common approach is a crossing of two laser beams [58, 59] to generate a much tighter confinement of the atoms in all directions. Providing higher densities increases the elastic collision rate and makes the evaporation process faster. Nevertheless the trapping frequencies will decrease with lower trap potentials making it necessary to work with small beam waists. More sophisticated solutions were therefore developed.

In [60] a crossed dipole trap with a movable lens was realized to adjust the overlap of the two beams. This makes it possible to load the atoms in a large trap and then compress the atoms during evaporation to have fast rethermalization.

The group of R. Grimm realized a crossed ODT with an additional tightly focused beam [61]. This makes it possible to catch the atoms in a large trap and increase the density with the dimple for fast cooling.

Both methods have one thing in common. Forcing evaporation by changing the trap depth also influences the shape and the trap frequencies. The setup in [62] uses a magnetic field gradient to lower the trap depth and force evaporation cooling. The trap confinement is unaffected, keeping the atoms at high collision rates. Even runaway evaporation is achieved, where the collision rate increases during the cooling process. A more flexible way in reference [63] uses a misaligned dipole beam instead of the magnetic field gradient, leaving the opportunity to use the magnetic field as an independent tool. A tightly focused beam offers a large trap depth and high trap frequencies. The misaligned large beam creates a potential gradient, which pulls the atoms out of the confined trap. By varying the laser power, the effective trap depth can be changed without changing the trap frequencies. This is in analogy to the radio frequency knife in magnetic traps.

3

EXPERIMENTAL SETUP

In fall 2014 our group started the design of a new ultracold, dual-species Rydberg experiment. Within this thesis, which started in April 2015, parts of this new experiment were designed and built up. The new experiment is build as a successor of the first generation experiment [64], at which the first Rydberg molecules were detected in 2009 [7], the permanent electric dipole moment of homonuclear Rydberg molecules was investigated [65] and single Rydberg atoms in a BEC could be studied [66]. A second generation single species setup was built up from 2011 to 2014 in our institute [67, 68]. It offers, in contrast to the first generation experiment, an optical resolutions better than the Rydberg blockade of typically several micrometer [69] and can detect single ions with temporal resolution.

The third generation setup partly designed, built up and envisaged within thesis is a further development aiming at the extension of experimental possibilities. It is designed as a two species experiment featuring the elements rubidium and lithium and will enable to experimentally realize the first heteronuclear Rydberg molecules. These molecules are envisaged to be used as a sensitive in-situ probe for spatial correlations in fermionic and bosonic quantum gases and to study ion-atom collisions in the ultracold quantum regime. An elementary feature of the experiment will be a delay line detector, enabling single ion detection with high temporal and spatial resolution. An ion microscope column in front of the delay line detector further increases the spatial resolution to better than the Rydberg blockage radius.

This chapter gives an overview over the experimental setup and conceptional ideas behind it. The main part of this master thesis was the design of a dual-species Zeeman slower to provide a high flux of rubidium and lithium atoms. Furthermore, a magnetic field control for low and high fields was designed. In the following detailed calculations and simulations for the Zeeman slower and the magnetic field coils are presented. Additionally, calculations for an optical dipole trap with minimum relative shift of two elements due to the gravitational force and the laser system necessary for cooling the atoms are described.

3.1 THE VACUUM CHAMBER

Experiments with ultracold gases require an ultra high vacuum with pressures of 10^{-11} mbar to 10^{-12} mbar. At higher pressures collisions with the background gas heat up the trapped atoms and remove them

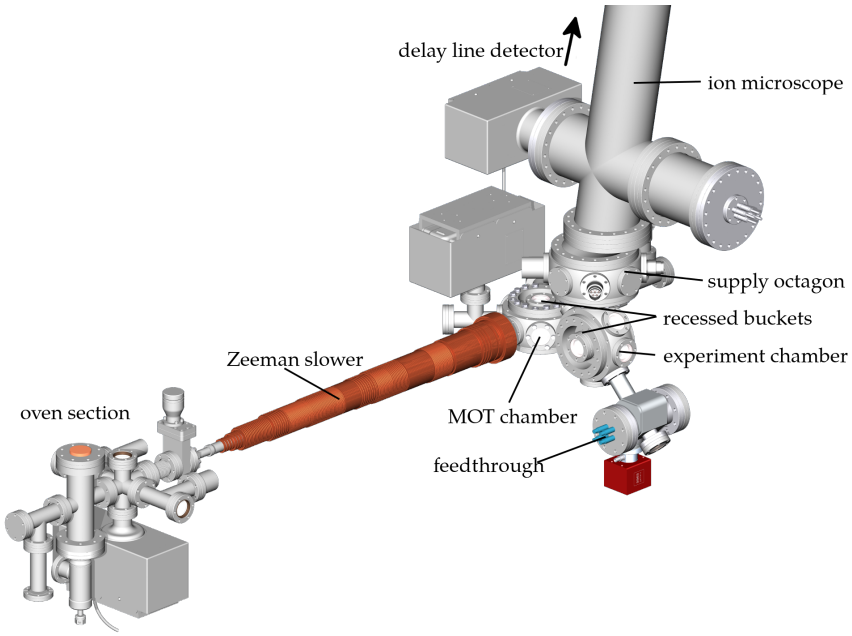

Figure 3.1: CAD drawing of the vacuum setup. The oven section provides a collimated atomic beam of rubidium which is slowed down to velocities smaller 30 m/s and trapped in the MOT chamber. After precooling the atoms are optically transported into the experiment chamber for the measurements. A delay line detector in combination with an ion microscope provides high spatial and temporal resolution to detect ionized Rydberg atoms.

from the trap. To reach such low pressures, an elaborated vacuum chamber is required.

The complete vacuum chamber is shown in figure 3.1. The rubidium and in a later stage of the experiment lithium are heated up in the oven section. This section can be separated from the other parts of the vacuum chamber to provide access to the rubidium and lithium reservoirs, while keeping the vacuum in the rest of the setup. The rubidium and lithium atoms leaving the oven are too fast to be trapped in the magneto-optical trap and therefore get simultaneously slowed in the dual species Zeeman slower. A small differential pumping tube at the end of the oven section and the long Zeeman slower tube reduce the flux of background gas to the MOT chamber.

After precooling the atoms, they are transported over a length of 18 cm to the experiment chamber with a 300 W Ytterbium fiber laser with 1070 nm wavelength. The focus of this laser beam can be shifted by a lens mounted on a air bearing translation stage, which can be controlled by a computer. After the transport the atoms will be evaporative cooled in the optical dipole trap. The multiple frequency modes of the transport laser can induce heating of the atomic cloud by driving two-photon Raman transitions. Nevertheless, successful evapora-

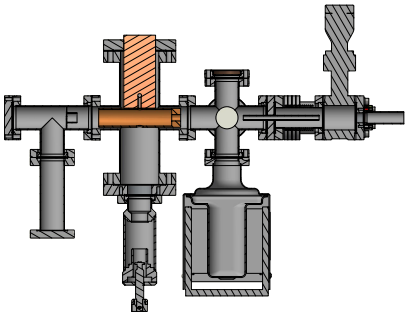

(a) CAD drawing of the oven section.

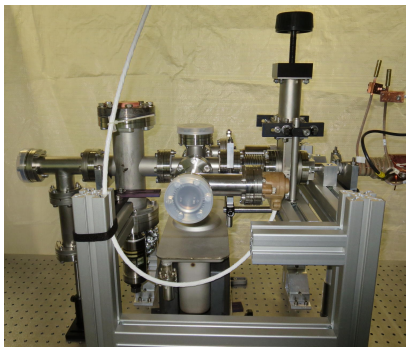

(b) Picture of the assembled oven with a rubidium reservoir

Figure 3.2: The oven section of the experiment to produce a high flux of rubidium and lithium. The lithium reservoir is not mounted to the oven and will be added later. Rubidium is placed in the lower left tube of the vacuum system and the Zeeman slower is connected on the right side to the gate valve.

tive cooling with rubidium 87 in a multifrequency laser was demonstrated in reference [70].

After evaporative cooling in the optical dipole trap to an ultracold thermal or degenerated gas, the Rydberg excitation and measurement can be performed. Ionized Rydberg atoms can be imaged on a delay line detector via an ion microscope with three electrostatic lenses. This magnifies the ion beam over 100 times, increasing the resolution to 1 µm which is smaller than the Rydberg orbit for high quantum numbers. Several feedthroughs on the lower right of the experiment chamber (figure 3.1) and in the supply octagon allow to connect the electric field control inside the experiment chamber and the ion lenses.

3.1.1 *The oven section*

There are several solutions for an atomic source to load MOTs. Loading the trap with background gas atoms from a dispenser [67], with a double MOT system [71, 72], a 2D MOT [73] or with an effusive oven and a Zeeman slower is possible. The effusive oven with the Zeeman slower has the advantage to produce the highest atomic fluxes at low background gas pressures in the trapping region. It also requires a low amount of cooling light compared to the other solutions.

The oven produces a flux of lithium and rubidium atoms. A schematic view and a picture of the oven is shown in figure 3.2. It can be separated from the Zeeman slower by a gate valve which provides access to the lithium and rubidium reservoirs, while keeping the vacuum in the rest of the setup. The reservoir for the rubidium on the left side in figure 3.2 is heated up to 160 °C, to produce a high flux of atoms.

The lithium reservoir will be added later to the setup and can be connected to the vacuum system at the rubidium reservoir tee. It has to withstand 400 °C because of the smaller vapor pressure of Lithium. The pressure in the oven is calculated with

$$p_{Rb}(T) = 10^{9.3177-\frac{4040}{T}} \text{ and} \tag{3.1}$$

$$p_{Li}(T) = \frac{101325}{760} \times T^{0.68106} \times 10^{10.3854-\frac{8345.574}{T}-0.0000884\cdot T}, \tag{3.2}$$

where temperature is given in Kelvin and pressure in Pascal. At the given temperatures, the pressure for rubidium is $1 \cdot 10^{-2}$ mbar and for lithium $8.6 \cdot 10^{-1}$ mbar. Due to the reactive nature of lithium and the high temperature, the copper gaskets have to be replaced with sealed nickle gaskets to prevent corrosion by the reactive lithium vapor.

A nozzle, which is in our case an aperture with 3.5 mm diameter, together with a cooling shield collimates the atomic beam. The cooling shield is made of copper and is cooled by a Peltier device[1] to approximately 0 °C. This reduces the amount of atoms, which are not directed towards the slower and get stuck in the oven section, preventing a rapid filling of the ion pump. A venting valve is placed at the four-way cross, necessary when refilling the rubidium or lithium reservoirs. After the cooling shield a six-way cross enables optical access on the horizontal axis, allowing optical pumping and an easier alignment of the slower beam. On the vertical axis the ion pump[2] is connected. A rotatable shutter in this cross interrupts the atomic beam after loading the MOT to prevent collisions of the fast atomic beam with the trapped atoms. A differential pumping tube with a diameter of 6 mm and a length of 120 mm reduces the pressure in the Zeeman slower and MOT chamber and additionally causes a more collimated atomic beam in the slower.

3.1.2 *The MOT and experiment chamber*

The main chamber[3] is shown in figure 3.3. It is split into two parts and made of 316L steel, offering a very low magnetic permeability.

The UHV MOT chamber is connected to the Zeeman slower and provides optical access for the MOT cooling and repumping light (indicated in orange in figure 3.3). The slowing light for the Zeeman slower enters the chamber through a window opposite of the slower. In experiments with chromium and dysprosium, the windows are coated quickly with atoms too fast to be trapped in the MOT, reducing the transmission of the slowing light through the window. A simple solution is to use a mirror and have the window not directly

1 Adaptive ET-161-12-08-E, 100 W
2 Agilent ion pump, VacIon Plus 40 StarCell
3 MCF800M-Cust-G1F4C13 from Kimball Physics

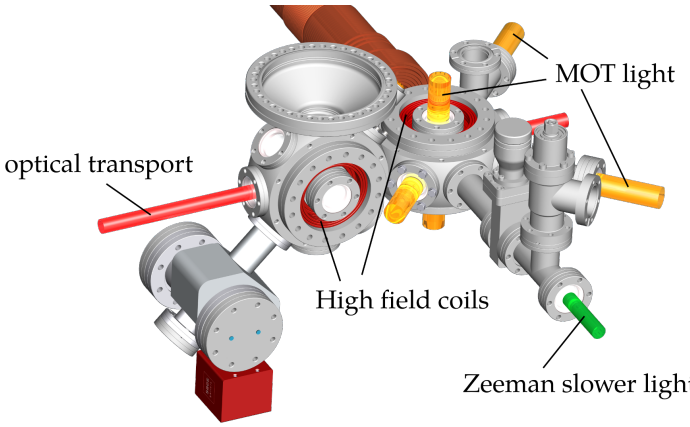

Figure 3.3: The main chamber is split into two parts: the MOT chamber for precooling the atoms after the Zeeman slower and the experiment chamber with electric field control, an in-vacuum lens for high optical resolution and the ion microscope for the delay line detector. The atoms are transported optically in a focused 1070 nm beam with 300 W. The high magnetic field coils are placed inside recessed buckets to allow a smaller design of the coils, reducing the required current and dissipated heat. The Zeeman slower light enters the chamber through a heated window.

in the atomic beam path. In the case of chromium, the mirror gets coated, but remains its high reflectivity. However, a test with dielectric mirrors in lithium vapor was not successful, because the lithium vapor reacted with the coating and destroyed the mirror. Stainless steel does not react, however its reflectivity is rather low (around 50% – 60 % [74]) for wavelengths between 600 nm and 800 nm. The reflectivity could increase with time, if a layer of lithium or rubidium is deposed on the steel, but it is unclear if the atomic beams of rubidium and lithium depose as flat layer on the steel. To reduce the risk of blocking the window with layers of rubidium and lithium, the possibility to heat the window is integrated. A gate valve makes it also possible to change the window, if the coating cannot be removed. Such a scheme is already successfully used in the group of J. Hecker Denschlag.

Compensation of residual fields smaller than the earth magnetic field (≈ 0.5 G) is necessary for sub-Doppler cooling in the optical molasses. The magnetic field compensation is realized by three Helmholtz coil pairs mounted around the MOT chamber. They are not shown in figure 3.3 for better visibility of the vacuum setup but explained in detail in section 3.4.4. High field coils in Helmholtz and anti-Helmholtz configuration are mounted in flanges of the MOT chamber. The anti-Helmholtz coils are generating the field gradient for the MOT and can be water cooled (see section 3.4.3). The coils in Helmholtz configuration are used to produce fields up to ≈ 1 kG, to tune the inter-

action between the lithium atoms via a Feshbach resonance for more efficient cooling. They are described in detail in section 3.4.2.

After precooling of the atoms in the MOT, they are transported to the experiment chamber with a 300 W Ytterbium fiber laser with 1070 nm wavelength. This chamber provides doubly-recessed flanges, allowing high magnetic fields with the Feshbach coils and strong field gradients with the anti-Helmholtz coils (same design of the coils as in the MOT chamber). The doubly-recessed design additionally allows an ultra stable electric field control with eight field plates in clover leave configuration [75]. An in-vacuum lens provides a high numerical aperture for imaging and to write potential landscapes into the atom cloud. An ion microscope is also connected to the chamber to achieve magnifications greater than 100 for the spatial detection on the delay line detector. The chamber is surrounded by coils in Helmholtz and anti-Helmholtz configuration to compensate any small magnetic field offset and gradients.

3.2 COOLING AND TRAPPING LIGHT

The principle of laser cooling is described in section 2.2. For reliable operation of the experiment, frequency stabilized laser light is needed. Not only a high long term stability is required, but also a narrow linewidth, to enable the addressing of the single hyperfine state of the atoms in the cycling transition. Additionally the Zeeman slower and the MOT require intensities larger than the saturation intensity. With higher laser power, it is also possible to have larger beams for the MOT at the same saturation parameter. This increases the capture range and MOT size. Typical values for the intensities of a rubidium MOT cooling light beam are about eight times the saturation intensity ($I_{sat} = 1.6\,\mathrm{mw/cm^2}$) in radial and 23 times in axial direction [64]. Because the laser light also passes plenty of optical elements a larger total laser power is required. Especially accusto optical modulators (AOMs) have only an efficiency of $60 - 80\%$ and thus reduce the initial laser power significantly. Hence the laser has to deliver several hundred milliwatts to allow efficient cooling.

Most of the rubidium cooling laser setup of the old experiment can be reused. Only the last part before the experiment chamber needs new components for two reasons. First the $\lambda/4$ wave plates in front of the chamber have to work for the wavelengths of both rubidium and lithium and the beams have to be overlapped. Second the beam size is increased and instead of one inch optics, mirrors and wave plates with two inch diameter are required to distribute the light to the chamber. Also the old repumper laser was replaced by a DFB laser diode, to increase the stability of the system.

For lithium a complete new laser setup has to be built. In contrast to rubidium, the amount of reliable commercial laser sources for 671 nm

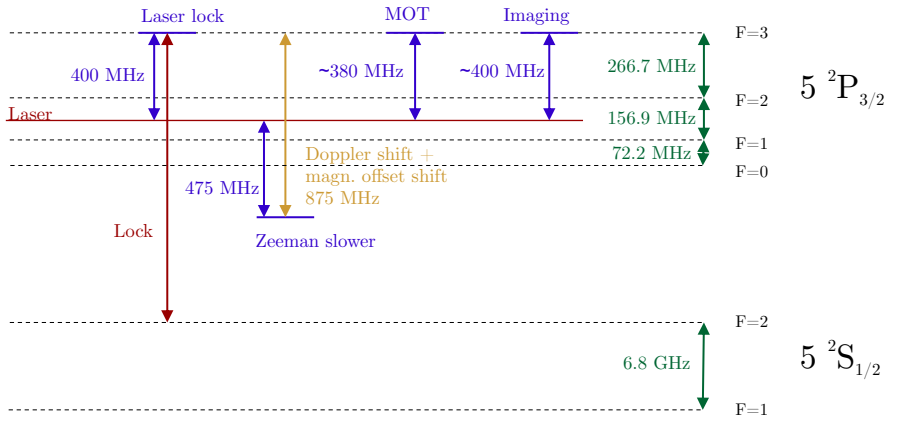

Figure 3.4: Scheme of the different frequencies of the rubidium cooling laser used in the experiment. The frequencies are shifted with AOMs. This enables flexible detunings during the experiment cycle.

light is much smaller. Especially for powers exceeding several tens of milliwatt. To set these up will be a future project and is therefore not described in this thesis.

3.2.1 *Cooling and imaging light*

The rubidium laser system consists of a Nd:YAG laser[4], which produces up to 10 Watts of 532 nm light. It is used to pump a titan-sapphire laser[5], producing approximately 700 mW of light with 780 nm wavelength at 8.5 W of the Verdi-V10 pump light. This light is then used to cool the atoms in the Zeeman slower and catch them in the MOT, as well as for absorption imaging. As described in section 2.4 the Zeeman slower light needs to be detuned by approximately 875 MHz from the $F = 2 \rightarrow F' = 3$ cooling transition, whereas the MOT laser beams need to be red-detuned by a couple of linewidths ($\approx 20 - 30$ MHz). This is achieved by several AOMs in the light path. The full scheme of the different laser frequencies is shown in figure 3.4.

Additionally the modulators allow a very fast switching of the laser power in typically 30 ns. However, a small amount of the light can leak through the modulator, thus mechanical shutters[6] are placed into the light path to completely block the light.

To frequency stabilize the laser, a small part of the light is shifted by 400 MHz in frequency with a double pass AOM and sent to an absorption spectroscopy cell. The shifted laser light is then frequency stabilized with Doppler-free polarization spectroscopy to the $5^2S_{1/2}F = 2 \rightarrow 5^2P_{3/2}F' = 3$ transition [76]. The rest of the light is split into several

4 Coherent Verdi-V10
5 Coherent MBR 110
6 LS3ZM2H, Uniblitz, Vincent Associates

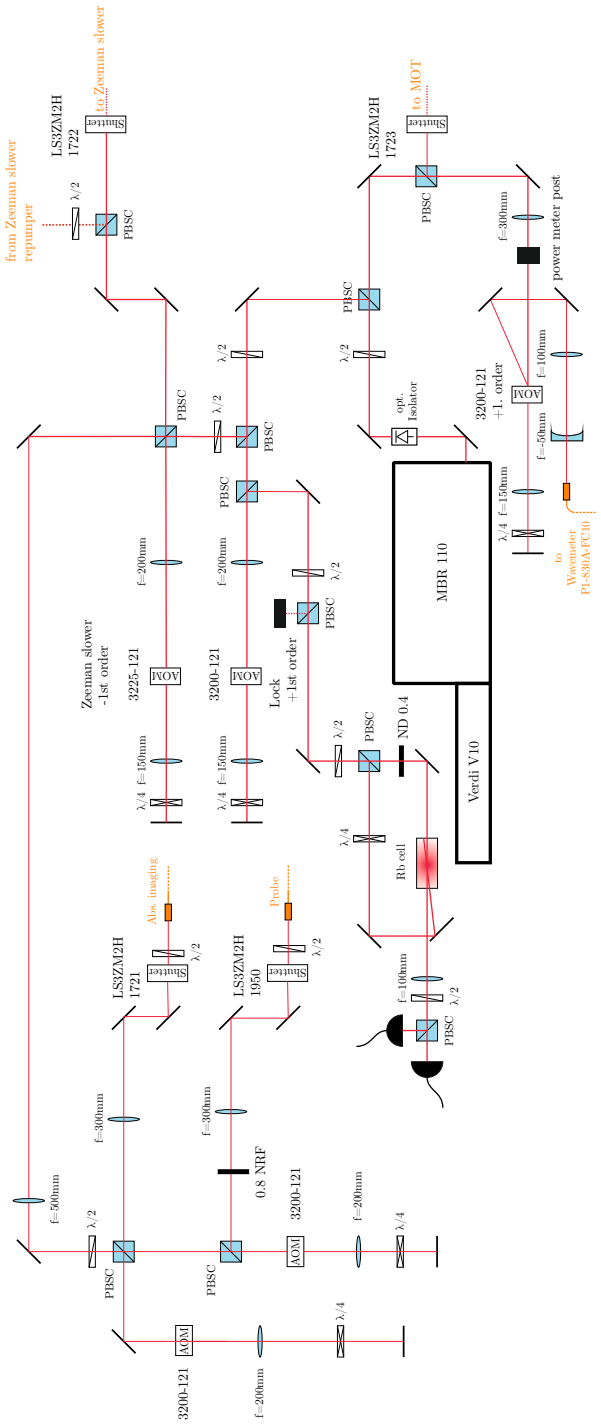

Figure 3.5: The rubidium cooling laser setup. The cooling light is generated by a pumped Titanium Sapphire laser. The light is frequency stabilized with Doppler-free polarization spectroscopy. Most of the laser power is directed to the MOT and the Zeeman slower. The Zeeman slower light is superimposed with repumper light (section 3.2.2). The MOT repumper light is superimposed before it is split up to the different MOT axes. Some light is extracted for absorption imaging.

paths by $\lambda/2$ wave plates and polarizing beamsplitter cubes (PBSCs). Most of the light is coupled into the MOT path. A lens focuses the beam through a 200 MHz AOM in double-pass configuration for the required frequency shift. The $\lambda/4$ wave plate turns the polarization of the reflected beam by $90\,^\circ$ in respect to the incoming beam. This allows the separation of the incoming beam and the reflected beam with a PBSC. The driving frequency of the AOM can be shifted during the sequence to adopt the detuning for the MOT and molasses cooling.

The light for the Zeeman slower is shifted by 475 MHz with a modified double pass AOM. The modulators are made of a crystal, e.g. TeO_2, in which the light beam is Bragg deflected at an acoustic wave. The frequency of the acoustic beam can be changed by $10 - 25$ MHz around the specified central frequency, which is on the order of several tens to some hundreds of megahertz, without influencing the efficiency of the deflection. One reason for this limited bandwidth is a electric resonant circuit inside the AOM. It matches the impedance of the modulator with the impedance of the cable and frequency source. Otherwise the rf power is reflected back to the frequency source and is not radiated into the crystal.

The reflected rf signal of the AOM was measured with a directional coupler[7]. The frequency source is connected to the output port of the directional coupler and the AOM to the input port. The signal returning from the AOM is then directed to the coupled port and can be evaluated on a frequency analyzer. Such a signal is shown in figure 3.6a for an unmodified CrystalTec AOM 3225-121. At the specified driving frequency of 200 MHz most of the power is coupled into the AOM, but at the required frequency of $235 - 240$ MHz for the Zeeman slower most of the signal is reflected. By changing the impedance of the circuit one can change the central frequency in some finite range. In figure 3.6b the resonance circuit with two coils and one capacitor is shown. The resonance frequency of this circuit can be tuned to higher frequencies by stretching the two small coils, thus lowering their inductivity. Additionally the variable capacitor has to be adjusted. The slightly asymmetric resonance curve, shown in figure 3.6a, could be caused by the circuit board, which is not specified for the higher frequencies. However it is also possible, that the perfect adjustment of the resonance circuit was not found. The efficiency was measured with 780 nm light from a Toptica DLPro system with a $1/e^2$ beam waist of 200 µm. The unmodified version has a diffraction efficiency of 80 % at 200 MHz. For the modified version the efficiency of 75 % at 240 MHz is only slightly less. The frequency can be tuned between 225 MHz and 250 MHz without any drop in efficiency larger than 1 %. This is the required frequency range needed for the Zeeman slower

7 MiniCircuits ZDC-20-3

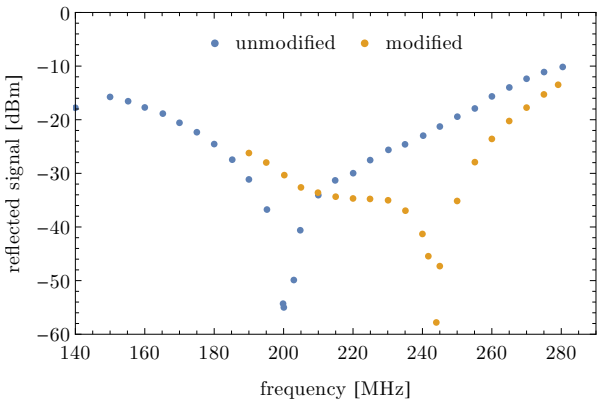

(a) Reflected signal of of the AOM.

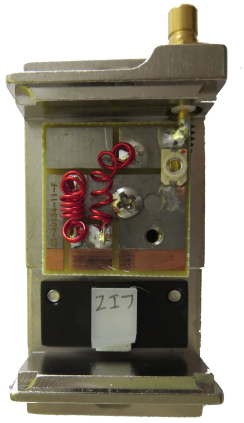

(b) Modified resonance circuit of the modulator

Figure 3.6: The modified accusto optical modulator for the Zeeman slower. The resonance circuit was optimized to work at 240 MHz. The reflected signal was measured with a directional coupler (Mini-Circuits ZDC-20-3)

and therefore the asymmetric impedance around the center frequency in figure 3.6a is no drawback.

For imaging a small amount of light is used. An AOM shifts the light to the desired frequency. The light is then coupled into a fiber to transfer it to the vacuum chamber and to get a clean Gaussian mode. To block any leaking light, a mechanical shutter is placed in front of the fiber couplers.

3.2.2 *Repumper light*

A new distributed feedback laser system (DFB) was set up for the repumper. Compared to normal laser diodes, DFB laser diodes have a Bragg grating in their gain section. This grating restricts the laser to work at a single longitudinal mode. This offers better quality of the beam compared to laser diodes with reflective end surfaces. These types normally operate with multiple longitudinal modes, if no feedback, e. g. by an external cavity, is used. In the old setup such an external cavity diode laser was used which offers a narrower linewidth (typical smaller 1 MHz) as a DFB lasers (several MHz). However this is not necessary for the repumper and therefore a DFB diode offers a stable and compact replacement. To tune the wavelength, the temperature and current of the diode can be changed. Whereas temperature changes the wavelength on a rather slow timescale on the order of seconds, a much faster way to modulate the frequency is realized by modulating the current.

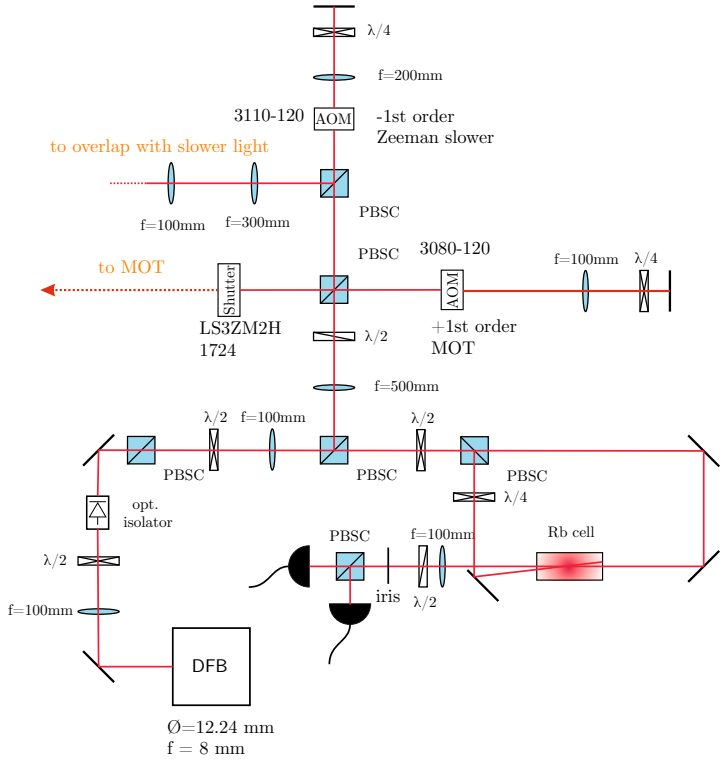

Figure 3.7: Setup of the rubidium repumper laser. A DFB diode with 80 mW output power is stabilized via polarization spectroscopy on a rubidium cell.

In our setup a DFB laser diode[8], emitting at 780 nm, is used. At 140 mA an output power of 80 mW is achieved. It is mounted in a Toptica TCLDM9 mount with integrated thermoelectric cooler for optimal thermal stability. The temperature and current is stabilized with commercial controllers[9]. For the frequency stabilization a rubidium gas cell for Doppler-free polarization spectroscopy and self-built PID controller are used. The measurement of the laser linewidth was done with a heterodyne measurement scheme. For the heterodyne detection, a second very narrow reference laser is needed. The two lasers interfere and generate a beatnote signal. If the laser frequencies are close enough, the beatnote signal can be measured with a photodiode. For a narrow reference laser with negligibly narrow linewidth the width of the beatnote signal peak corresponds to the linewidth of the laser to be characterized. In this measurement a reference laser with 3 kHz linewidth was used [77] and the linewidth of the DFB laser diode was measured to be 14 MHz. This makes it suitable for repumping, because the linewidth is smaller than the hyperfine splitting of the $5P_{3/2}$ state.

8 Eagleyard, EYP-DFB-0780-00080-1500-TOC03-0000
9 Toptica TED200C and Toptica LDC205C

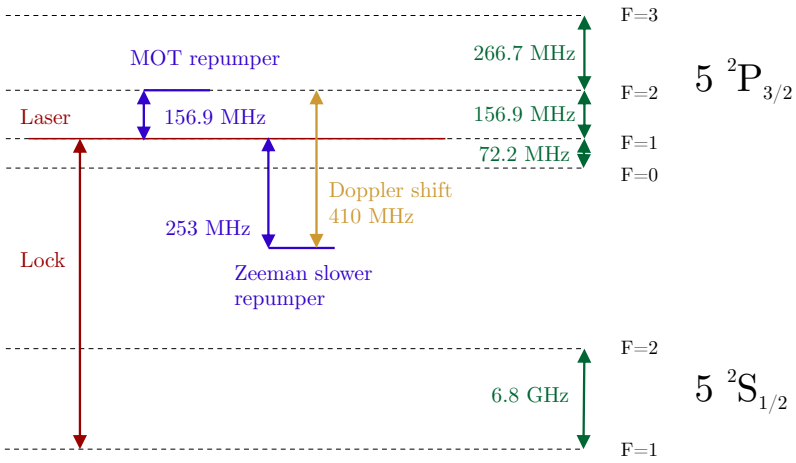

Figure 3.8: Repumper locking scheme for rubidium 87

The complete repumper setup is shown in figure 3.7. An optical isolator preserves the diode from destruction by back reflections of the laser light. A small part of the light is then directed to the rubidium cell for frequency locking of the laser, whereas most of the light is split and send to two AOMs. The locking scheme is shown in figure 3.8. The frequency of the laser is locked to the $5^2S_{1/2}F = 1$ to $5^2P_{3/2}F = 1$ transition via Doppler-free polarization spectroscopy. For the MOT repumping light one AOM shifts the light in resonance with the $5^2S_{1/2}F = 1$ to $5^2P_{3/2}F = 2$ transition, whereas the Zeeman slower repumper is shifted with an AOM to the red by 253 MHz to compensate for the Doppler shift of the atoms leaving the oven with 300 m/s.

3.2.3 *Optical dipole trap*

Dipole traps are, together with magnetic traps, the tool of choice to cool atoms down to the quantum regime. The principle of optical dipole traps is explained in section 2.7. However until now we have not discussed multiple species in one trap.

In general atoms of different species have different light shifts in the same light field. As a consequence, the different species feel distinct potential depths in an optical dipole trap. This property is already used in some experiments for species selective trapping [78, 79].

In this experiment, an ODT for both elements, rubidium and lithium, is required. For a typical ODT with a 1064 nm laser, the trap depth of rubidium (equation 2.21) is

$$\frac{U_{0,Rb}}{U_{0,Li}} = \frac{\Gamma_{Rb} \cdot \delta_{Li} \cdot \omega_{0,Li}}{\Gamma_{Li} \cdot \delta_{Rb} \cdot \omega_{0,Rb}} = 2.6 \tag{3.3}$$

times deeper as for lithium, where ω_0 is the center frequency between the two D lines and δ is the detuning of the laser in respect to this

frequency. This is mainly due to the higher transition frequency of the D_1 and D_2 lines in lithium. The lifetimes of the excited states are nearly the same. Assuming the same temperature for both elements in the ODT and a typical trap depth to temperature ratio for evaporation of $\eta = \frac{U_{0,Li}}{k_B T} = 10$ (see section 2.7.2), the evaporation rate for rubidium is suppressed by

$$\frac{e^{-2.6\cdot\eta}}{e^{-\eta}} \approx 1.1 \cdot 10^{-7} \tag{3.4}$$

compared to the evaporation rate achieved for an η equal to that of lithium. As a result, evaporative cooling will result in loss of lithium atoms, whereas rubidium is sympathetically cooled by the lithium. In magnetic traps this cooling process can be done the other way around, by choosing the appropriate rf frequency to evaporate rubidium [80] instead of lithium. For efficient sympathetical cooling a high elastic interspecies collision rate is important, hence a large spatial overlap of the two clouds is preferable to allow a high number of elastic collisions.

In general the optical dipole potentials are much stronger than the gravitational potential, making it possible to neglect gravitation. For very low trap depths during the evaporation process the high mass ratio of rubidium and lithium with $m_{Li}/m_{Rb} = 14.4$ renders the separation of the clouds. This is called gravitational sag. In the following a setup of an ODT minimizing the relative shift of the two elements is discussed. The relative shift of the potentials for rubidium and lithium is calculated for a single Gaussian laser beam with 1064 nm. This can be done by inserting equation 2.59 in equation 2.24 and adding the linearized gravitational potential

$$U_{pot} = U_0(z) e^{-2\frac{x^2+y^2}{w^2(z)}} - m \cdot g \cdot x \tag{3.5}$$

with U_0 as the potential depth, m the mass of the atom, g the gravitational acceleration and $w(z)$ as the waist size of the beam. In this case the gravitation is pointing in x-direction, whereas the beam is perpendicular, pointing in z-direction. To find the minimum

$$x_{min} = \frac{w_0}{2}\sqrt{W\left[\left(\frac{2U_0}{g \cdot m \cdot w_0}\right)^2\right]} \tag{3.6}$$

the derivative is set to zero at $y = z = 0$, where w_0 is the beam waist size. W represents the Lambert-W function. In figure 3.9 the relative shift between the lithium and rubidium potential minimum is plotted over the waist size and potential depth of lithium. Two conclusions can be drawn from this. First of all, the relative shift matters at very low trap depths of around 3–5 μK (8–13 μK for rubidium). These trap depths are reached for typical degenerate lithium Fermi gases with temperatures of 200 nK to 500 nK [81, 82]. Second, the relative shift

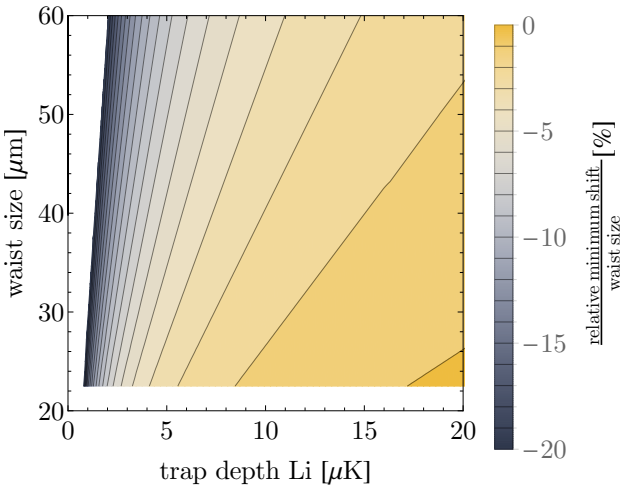

Figure 3.9: Relative shift of the lithium and rubidium potential minima in respect to waist size and trap depth of lithium.

can be minimized by choosing the beam waist as small as possible. In the misaligned crossed dipole trap [63] (see figure 3.10) this shift can be further reduced. Figure 3.10 shows the principle of the crossed misaligned dipole trap and the potentials for lithium and rubidium in a 1064 nm laser. The smaller beam has a waist of 40 µm and a power of 1.2 W, whereas the bigger beam with a waist of 130 µm has a power of 12 W. By increasing the laser power of the larger beam to 20 W, the effective potential depth U_{eff} for lithium can be lowered to 5 µK without changing the trap stiffness. The resulting trap frequencies are calculated by a harmonic potential approximation at the minimum of the trap and given in table 3.1.

	$\omega_x/2\pi$ [Hz]	$\omega_y/2\pi$ [Hz]	$\omega_z/2\pi$ [Hz]	U_0/k_B [µK]
Lithium	1015	1015	236	37
Rubidium	438	438	102	100

Table 3.1: Trap frequencies and maximum trap depth of the crossed misaligned dipole trap for 1.2 W in the small trapping beam.

The relative shift of the potential minimum for the misaligned crossed beam solution compared to the single beam trap is plotted in figure 3.11. The single beam has a waist size of 40 µm and the misaligned crossed trap has beam waists of 40 µm for the small and 130 µm for the large beam. In this configuration the relative shift of the cloud is strongly suppressed. Instead of a relative shift of 10 % of the waist size at a trap depth of 3 µK for lithium, the shift only amounts to 2 %. One can also see in this plot, that the ratio for the trap depths of rubidium and lithium decreases for lower depths even below one in the single beam trap. This is due to the increasing ef-

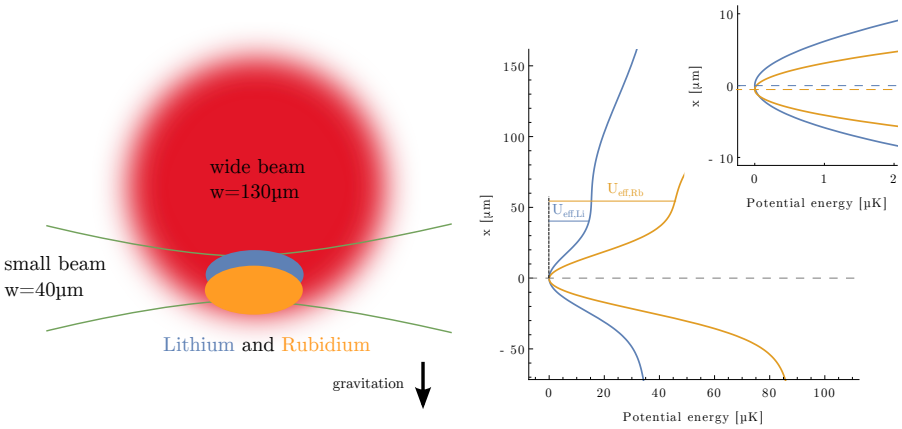

Figure 3.10: Optical dipole trap potentials for lithium and rubidium in misaligned crossed 1064 nm beams with a waist w of 130 µm for the wide beam and w = 40 µm for the small beam, which is displaced by 65 µm. The larger beam applies a force, pulling the atoms out of the tight beam and allowing them to escape along the axial direction of the wide beam. By increasing the power, the effective trap depth can be reduced.

fect of the gravitational potential (14.4 times stronger for rubidium) in lowering the trap depth of the optical dipole potential (2.6 times deeper for rubidium).

3.3 DUAL SPECIES ZEEMAN SLOWER

3.3.1 *Creation of the magnetic field*

To create the magnetic field for the Zeeman slower, several different design possibilities exist. In this chapter different designs are described with their advantages and drawbacks.

- The *permanent magnets* design does not require any electric power and produces no heat. Thus water cooling of the slower is not necessary. In this sense it makes the design easier. Another benefit is the ability to assemble and disassemble the system at any time. So it can be removed during the bake out. Two examples for such a design can be found in [83] and [84]. The trade-off is the transverse magnetic field, whereas in wire wound designs the field points solely in the direction of the slower axis. This transverse field enables atomic transitions other than the closed cooling transitions of the atoms. Also the magnetic field varies strongly over the beam diameter in such a system.

- The same transverse magnetic field can be produced with copper bars running along the vacuum tube. This was realized for ^{85}Rb in the group of V. I. Balykin [85]. Despite the easier design and assembly than a wire wound slower, the *transverse magnetic*

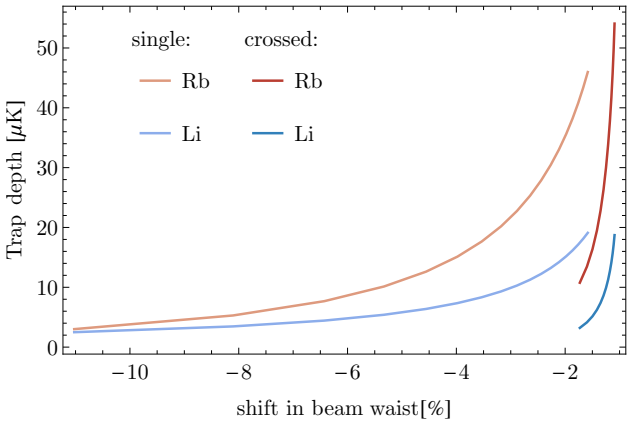

Figure 3.11: Shift of the potential minima for lithium and rubidium in a single beam ODT with 40 µm waist size and the misaligned crossed ODT solution. The shift was calculated up to an trap depth of around 3 µK for lithium.

field Zeeman slower has the same draw-backs of the field design as the the permanent magnet design.

- Lengths of Zeeman slowers are typically in the range of 30 cm to 80 cm. To simplify the production, the coil is often split into *individual segments*. Each segment is wound independently and it is not necessary to rewind the whole slower if it is damaged. With each solenoid connected independently to a power source, the magnetic field can be adjusted to an optimized MOT loading rate with the cost of lots of power supplies. Gaps between the different segments are inevitable and leads to ripples in the magnetic field.

- In reference [86] a single layer Zeeman slower was used for slowing rubidium. The magnetic field profile is produced by a *variable pitch* of the winding. Instead of coiling several hundreds of windings in multiple layers it is reduced to one layer. The drawback of such a design is the high current of 110 A to create the magnetic fields of up to 120 G. In the case of lithium fields up to 700 G are required, which would need much higher currents.

- The *continuous wire wound* Zeeman slower design only needs a single power supply for the continuous wound solenoid, but provides no flexibility in adjustment of the field after the coil is wound. Only the total field can be changed by increasing or decreasing the current.

In our design we have chosen to use a mixture of individual segments and the continuous wire wound design. To reduce the current we have chosen to wind several layers. Most parts of the slower were wound continuously to prevent magnetic field ripples caused by the

gaps between the individual solenoids. However, always two consecutive layers are wound with one consistent wire to provide more connections for fresh cooling water, which is running directly through the wire. Only the end of our Zeeman slower close to the MOT chamber has separate coils to provide a high magnetic field. Because the magnetic field in the coil axis drops proportional to the coil radius squared, only a few windings with small radii are preferable at the end of the slower. This prevents the magnetic field of the slower to leak into the MOT region. The further details are discussed in section 3.3.4.

In general a Zeeman slower is optimized for one specific element. The different masses, linewidths and Zeeman shifts of the different levels change the optimum length and required field strengths. For example with equation 2.43 one gets a required length of $L = 27\,\mathrm{cm}$ to slow lithium with an initial velocity of $700\,\mathrm{m/s}$ down to $20\,\mathrm{m/s}$, whereas rubidium with an initial velocity of $300\,\mathrm{m/s}$ needs a distance of $L = 81\,\mathrm{cm}$. The deceleration $a = \frac{a_0}{2}$ used for the calculation is in both cases half of the maximum allowed deceleration. In the references [87, 88] adoptable Zeeman slowers are described. They can load different species sequentially by changing the current of the coils to adjust the magnetic field profile to load different species sequentially into the MOT. A preferable solution is the ability to load simultaneously two species, because it reduces the experimental cycle time. This can be done by using one Zeeman slower for each element with the cost of reduced optical access to the chamber. By splitting the Zeeman slower into three distinct slowing segments, two optimized to slow lithium and one to slow rubidium atoms, only one Zeeman slower is required. A similar desing is used in the group of Stamper-Kurn [89]. It is used as a reference design for our setup.

3.3.2 *Atom flux*

The rate of atoms leaving the effusive oven (cf. section 3.1.1) into the surface angle $\frac{d\Omega}{4\pi}$ with an angle θ to the surface normal is [46]

$$d\Phi_0 = \frac{d\Omega}{4\pi} n \cdot \bar{v} \cdot A_{\mathrm{oven}} \cos\theta \,. \tag{3.7}$$

The number density $n = \frac{N}{V} = \frac{p(T)}{k_B T}$ for a classical Maxwell-Boltzmann distributed non interacting gas depends on the temperature as well as the mean velocity $\bar{v} = \sqrt{\frac{8 k_B T}{\pi m}}$. The total atomic flux depends then on the aperture of the oven $A_{\mathrm{oven}} = \pi r_{\mathrm{oven}}^2$, the opening angle ϑ and the oven temperature T, as well as the atomic properties like the mass and the vapor pressure p of the considered element:

$$\Phi_0 = \int_0^{\theta=\vartheta} d\Phi_0 = \sqrt{\frac{2\pi}{m k_B T}} \frac{r_{\mathrm{oven}}^2}{2} p(T) \sin^2\vartheta \,. \tag{3.8}$$

The total atomic flux Φ_0 out of the oven is in general not completely captured in the MOT and is reduced due to three factors [90].

First, the rubidium and lithium samples in the oven consists of different isotopes of the element. The natural abundance of the isotope used in the experiment is reflected by η_1. For rubidium 87 and lithium 6 the natural abundance is 0.28 respectively 0.076. This factor can be increased by using samples with an enriched fraction of the used isotope.

Second, the Zeeman slower can slow atoms up to a maximum velocity v_{max} (cf. section 2.4) and covers a finite velocity range of the atoms emitted by the oven. The velocity distribution follows a modified Maxwell-Boltzmann distribution [46]

$$f(v) = 2\left(\frac{m}{2k_B T}\right)^2 v^3 e^{-\frac{mv^2}{2k_B T}} . \tag{3.9}$$

The mass of the isotope is denoted by m, T is the temperature, v the velocity of the atom and k_B the Boltzmann constant. Hence the fraction of slowed atoms is

$$\eta_2 = \frac{\int_0^{v_{max}} f(v)dv}{\int_0^{\infty} f(v)dv} = 1 - e^{-\frac{m\cdot v_{max}^2}{2k_B T}} \left(1 + \frac{m \cdot v_{max}^2}{2k_B T}\right) . \tag{3.10}$$

In figure 3.12 the velocity distribution is shown for a temperature of 160 ° C for rubidium and 400 ° C for lithium. Additionally the fraction, which can be slowed by the Zeeman slower built in this experiment, is shaded. For rubidium this results in a fraction of 30 % and for lithium of 3 %.

Last, the atomic beam expands during the slowing process and its diameter at the position of the MOT is larger than the MOT capture radius, hence the captured fraction of atoms is further reduced by

$$\eta_3 = \frac{\text{atoms inside capture radius}}{\text{total slowed atom flux}} . \tag{3.11}$$

This blooming of the beam is caused by the transverse velocity of the atoms. Due to the slowing process in longitudinal direction, they have a longer time of flight compared to the unslowed motion and they cover a larger transverse distance. Additionally the spontaneous scattering of photons during the slowing process leads to a random walk of the atoms in the plane perpendicular to the slowing direction. At the beginning of the slower, the transverse velocity v_t is small compared to the longitudinal one v_l. After the slower the velocities are on the same order, causing a large diverging beam. To calculate the spread of the atoms, the atomic beam intensity profile at the MOT,

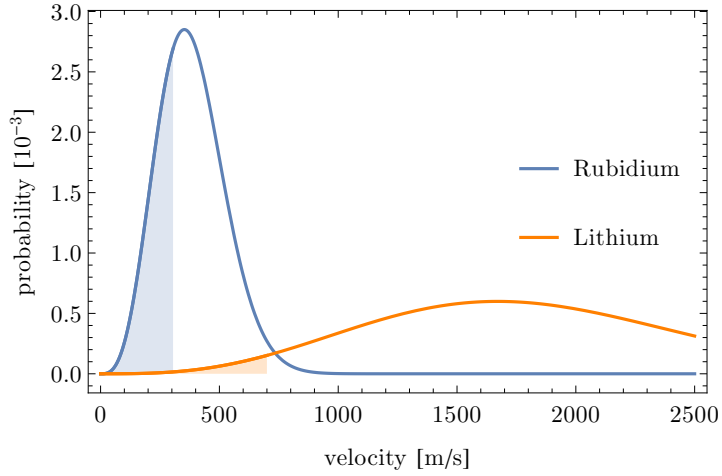

Figure 3.12: Velocity distribution of the rubidium atoms for an oven temperature of 160 °C and for a lithium gas with a temperature of 400 °C. The curve shows the probability to find an atom with velocity v in the velocity range dv. The colored area under the curve symbolizes the fraction of atoms which can be slowed by the Zeeman slower for a capture velocity of 300 m/s for rubidium (≈ 30%) and 700 m/s for lithium (≈ 3%).

perpendicular to the atomic beam axis (z-axis), is approximated by a Gaussian distribution

$$I_i(x) = \frac{1}{\sqrt{2\pi}\,\sigma_{MOT,i}}\, e^{-\frac{x^2}{2\sigma_{MOT,i}^2}} \tag{3.12}$$

for each velocity class v_i of the atomic beam with $0 < v_i < v_{max}$. The width $\sigma_{MOT,i}$ of the Gaussian distribution has now two contributions which we will discuss here, as far it is necessary for the calculation. A detailed treatment of this topic can be found in reference [90].

1. The oven limits the divergence of the beam by geometrical restrictions to an angle ϑ, which restricts the transverse velocity to

   $$v_{t,\,oven,i} = \vartheta \cdot v_{l,i} \tag{3.13}$$

   for atoms of the velocity class $v_{l,i}$. This velocity stays constant, hence the transverse spread

   $$\Delta_{flight,i}(t) = v_{t,\,oven,i} \cdot t \tag{3.14}$$

   is only determined by the time of flight of the atom t. Because the longitudinal velocity decreases and the atom stays longer in the Zeeman slower, the spread at the end of the slower is larger compared to the angle given by the oven.

2. The second contribution to the blooming of the beam is the diffusion of the atoms due to the spontaneous emission. Whereas

the absorption of the photons from the laser light decelerates the atoms, the spontaneous emission is isotropic and in average does not contribute to the momentum. However it leads to a random walk of the atom in the transverse plane, which causes the Gaussian beam profile[10]. The root mean square distance (here in momentum space) of the random walk depends on the square root of the number of steps, which corresponds in this case to the number of spontaneous emitted photons N_{RW}. In each step the momentum $\hbar k$ is transferred to the atom, giving a transverse velocity of

$$v_{RW} = \frac{\hbar k}{m}\sqrt{N_{RW}} \,. \tag{3.15}$$

The sum of the momentum of all scattered photons $N_{RW}\hbar k$ at time t is equal to the longitudinal momentum change of the atom $m \cdot (v_i - v(t))$ with an initial velocity v_i at $t = 0$ and a velocity $v(t)$ after the scattering of the photons. This yields to a transverse velocity of

$$v_{RW}(t) = \frac{\hbar k}{m}\sqrt{\frac{m}{\hbar k}(v_i - v(t))} \,. \tag{3.16}$$

The transverse distance covered by the atom depends on the flight time t and is given by

$$\Delta_{RW,i}(t) = \int_0^t v_{RW}(t')dt' \,. \tag{3.17}$$

Both of the two above outlined mechanisms contribute independently to the width of the atomic beam and have to be added in quadrature [90]. As a consequence a velocity class v_i has a Gaussian intensity profile at time t with a width of

$$\sigma_{MOT,i}(t) = \sqrt{(\Delta_{RW,i}(t))^2 + (\Delta_{flight,i}(t))^2} \,. \tag{3.18}$$

The integral over the intensities for each velocity $0 < v_i < v_{max}$ results in the total intensity of the atomic beam weighted with the modified Maxwell-Boltzmann distribution function

$$I(x) = \int_0^{v_{max}} f(v_i) I_i(x) dv_i \,. \tag{3.19}$$

The fraction of atoms in the MOT capture region with radius r_c is then calculated with

$$\eta_3 = \frac{\int_0^{r_c} I(r)dr}{\int_0^{\infty} I(r)dr} \,. \tag{3.20}$$

10 Initially after the collimating apertures of the oven the beam has a trapezoidal beam shape [46].

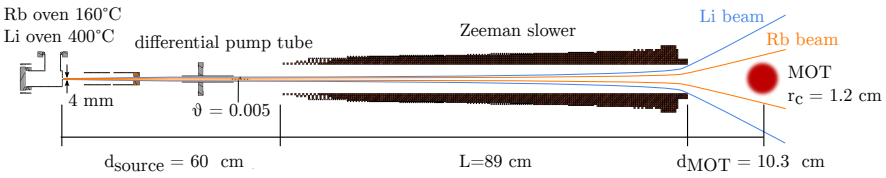

Figure 3.13: Illustration of the lithium and rubidium beam width between the oven and the MOT.

The radial symmetry of the intensity distribution was used to simplify the integral and to switch to polar coordinates. The total atomic flux in the MOT capture region is then expressed by

$$\Phi_{MOT} = \eta_1 \cdot \eta_2 \cdot \eta_3 \cdot \Phi_0 \ .$$

For lithium the divergence of the atomic beam is much more pronounced than for rubidium. Due to its lighter mass, the larger recoil $\hbar k$ and the larger initial velocities, equation 3.16 predicts a faster increase for lithium than for rubidium during the slowing process. Especially at the end of the slower the difference in the spread angle is significant. The transverse velocity for Lithium slowed down form 700 m/s to 60 m/s is 6.4 times larger than the transverse velocity of rubidium slowed from 300 m/s down to 30 m/s[11]. For a high brightness of both atomic beams at the MOT position, it is crucial for the final deceleration section of Li to be located close to the MOT. Figure 3.13 shows an illustration of the lithium and rubidium beam widths. Also a higher capture velocity of the MOT, allowing faster end velocities of the atoms at the end of the slower, is beneficial for a high beam brightness. Estimating the capture range of the MOT with equation 2.57 and typical values for the detuning ($\delta = 3\Gamma$) and the magnetic field gradient ($\partial B = 10\,G/cm$) gives a capture radius of $r_c = 1.2\,cm$. If the deceleration of the atoms in the MOT is conservative estimated to be half of the maximum deceleration a_0, the capture velocity is 35 m/s for rubidium and 140 m/s for lithium. Reference [89] gives capture velocities of 50 m/s for rubidium and 80 m/s in the case of lithium. The achievable size of our MOT will depend in the end also on the available laser power at the position of the MOT. For safe estimations of the required velocities of the atomic beam, the respectively smaller value of the capture velocities is used.

3.3.3 *Design considerations*

The design of the Zeeman slower has to fulfill following specifications, which are given by the experiment. It should produce an atomic flux

11 At the end of the slower the longitudinal velocity is mostly dominated by the random walk of the stimulated emission process. In this case for lithium $v_{t,\,oven,\,i} = 2.8\,m/s$ whereas $v_{RW} = 8\,m/s$.

of about 10^9 to 10^{10} atoms per second for both elements, to allow short loading rates of the MOT. The capture velocity for rubidium was set to 300 m/s and for lithium 700 m/s as such a dual species Zeeman slower was successfully demonstrated in reference [89]. Further aspects of the design are discussed here, before the simulation and construction process is explained.

A laser power of 20 mW in the slower beam for rubidium focused to an area of $1\,cm^2$ corresponds to 12.5 times the saturation intensity ($I_{sat} = 1.6\,mW/cm^2$ for the $F = 2, m_F = \pm 2$ to $F' = 3, m_{F'} = \pm 3$ transition with $\sigma^{\pm}$ polarized light) and gives a maximum possible deceleration of 95% of the maximum deceleration at infinite intensity. For lithium the saturation intensity is $2.54\,mW/cm^2$. For a deceleration of approximately 90% of the maximum possible deceleration, an intensity of nine times the saturation intensity is required. For lithium this results in a power of the laser beam of 23 mW.

Geometric constraints

The oven and the MOT and experimental chamber design define fixed geometric conditions for the Zeeman slower. The distance of the oven to the beginning of the Zeeman slower is approx 60 cm (figure 3.2 and figure 3.13). In between are the cooling shield, the beam shutter, a differential pumping tube, a gate valve and some space to shift the movable Zeeman slower (see section 3.3.5). The angle of divergence of the atomic beam is limited by the oven aperture and the differential pumping tube to $\vartheta \approx 0.005°$. Also the minimum distance between the MOT center and the end of the Zeeman slower is constrained by the size of the chamber and is 10.3 cm. The MOT laser beams are assumed to have a radius of 1.2 cm, which is setting the limit for the MOT size and capture range.

Magnetic field

The Zeeman slower is split into three stages which are described in this section. Comparing the two elements lithium and rubidium, the maximum allowed magnetic field gradient is much higher (equation 2.44):

$$\begin{aligned} v = 300\,m/s: \quad & \partial_z B_{Li} = 64.7\,G/cm, \\ & \partial_z B_{Rb} = 3.4\,G/cm. \end{aligned}$$

To slow down rubidium efficiently, the slower needs a long section with small magnetic field gradients. To stop atoms with $v_{max} = 300\,m/s$, the laser has to be red-detuned by $\delta = k \cdot v_{max} = 385\,MHz$. This frequency detuning is close to the $|F = 2\rangle \rightarrow |F = 1\rangle$ transition ($\approx 6\Gamma$, see figure 2.1) for atoms at small velocities. This is exactly the case for atoms in the MOT, which would consequently scatter the light and heat up. Using an additional bias field of 307 G shifts the laser

frequency 430 MHz to the red and circumvents the above described heating. The lithium is also slowed in this section, but compared to the maximum capture velocity of 700 m/s the velocity change is small (200 m/s) Because of its lighter mass, the effects of transverse heating are mostly influencing the beam brightness of lithium (see section 3.3.2). This requires a short section close to the MOT with a rapid deceleration from 200 m/s to the end velocity of 55 m/s for lithium by a steep rise of the magnetic field up to 700 G. In this section rubidium is not slowed anymore, because it is shifted out of resonance by the large magnetic field gradient and does not fulfill the adiabatic slowing condition anymore. The rise of the bias field for rubidium is additionally used to slow lithium atoms from 700 m/s to 400 m/s. Their transverse velocity after this first section is still much slower than their velocity in the Zeeman slower direction, keeping the diffusion of the lithium beam small during the longer rubidium section. Due to the possibilities of variations in the magnetic field, the Zeeman slower is designed with a smaller deceleration than the maximum deceleration, which is limited by the spontaneous emission. This dimensionless safety factor $\eta = a_{\text{eff}}/a_{\text{max}}$ is chosen to be 0.55 for lithium and rubidium. The length of the slower is then still reasonable short with $L_{\text{Rb}} = 73.6\,\text{cm}$ for the rubidium section and $L_{\text{Li}} = 18.3\,\text{cm}$ for the two combined lithium sections. Additionally a 2 cm long section was added to the beginning of the rubidium part, to allow a smooth transition from the lithium to the rubidium section.

3.3.4 *Simulation*

The Zeeman slower was developped with the help of simulations to match the requirements described in section 3.3.3. This was done by treating each winding of the coil as a current loop. A single current loop with radius R, current I and its axis pointing in z-direction produces a radially symmetric magnetic field which is in cylindrical coordinates given by

$$B_z(z,\rho) = \frac{\mu_0 I}{2\pi}\frac{1}{\sqrt{(R+\rho)^2+z^2}}\left(K(\kappa)+\frac{R^2-\rho^2-z^2}{(R-\rho)^2+z^2}E(\kappa)\right) \tag{3.21}$$

$$B_\rho(z,\rho) = \frac{\mu_0 I}{2\pi}\frac{z}{\rho\sqrt{(R+\rho)^2+z^2}}\left(-K(\kappa)+\frac{R^2+\rho^2+z^2}{(R-\rho)^2+z^2}E(\kappa)\right)\,. \tag{3.22}$$

Here μ_0 is the vacuum permeability and K and E are the complete elliptical integrals of the first and second kind. Their argument κ is

$$\kappa = \frac{4R\rho}{(\rho+R)^2+z^2}.$$

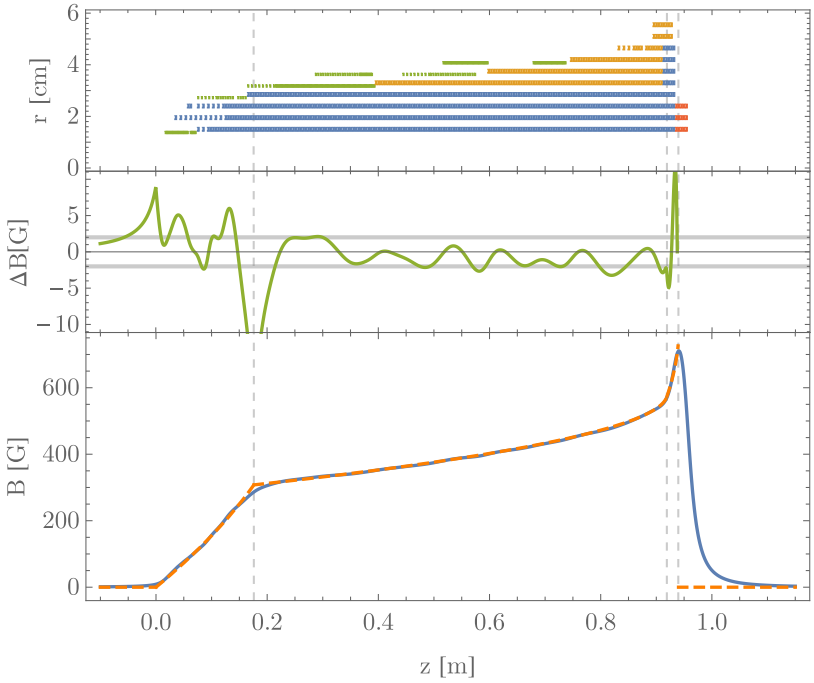

Figure 3.14: Simulated magnetic field (blue) of the Zeeman slower and its deviations (green) with respect to the theoretical optimum value (orange). The deviations in the rubidium section are less than ±2 G. In the lithium section the deviations are higher, but lithium is not as sensible as the rubidium to small deviations of the field. A winding plan to produce the magnetic field is shown at the top.

The magnetic field of the whole coil is the superposition of the magnetic fields of every single winding. The final field of the simulation and the plan for each coil winding is shown in figure 3.14.

The deviations of the simulated field from the ideal theoretical magnetic field are on the order of ±2 G for the middle part of the Zeeman slower. In the two parts where lithium is slowed, the deviations are between −2 G and 10 G. For the lithium slowing transition, the Zeeman shift caused by 10 G is about two times the natural linewidth of the transition. This seems a lot, but the adiabatic slowing condition is always fulfilled as it is shown in figure 3.15. For the large magnetic offset in the middle section, four layers with a current of 27.1 A are used. The last sharp peak is created by a small coil with few windings and a high current of 116 A. The small coil radius reduces the stray magnetic field in the MOT chamber. To minimize the ripples in the magnetic field, several coil layers operated at 19.6 A are placed on top of the bias field coils. Windings with a 2 mm wire with a current of 4.1 A are added to create a smooth magnetic field distribution.

To verify that the calculated magnetic field is suitable to slow the atoms, the slowing process for atoms with different initial velocities is simulated. The simulation solves numerically the differential equa-

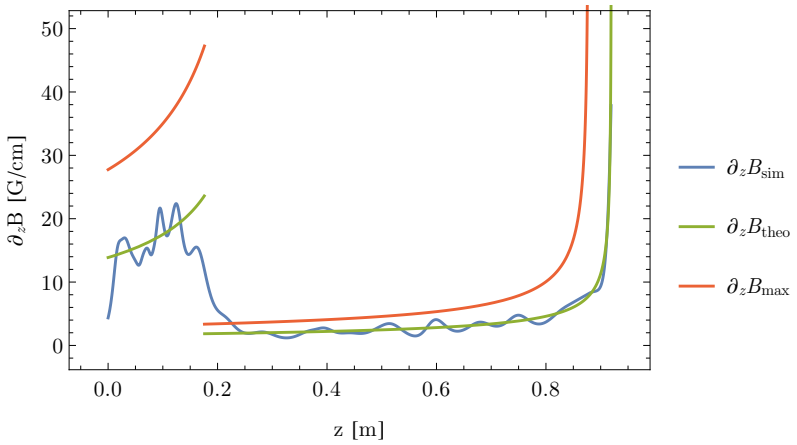

Figure 3.15: Magnetic field gradient of the simulated magnetic field (blue) and the theoretical ideal field (green). The maximum allowed gradient given by the adiabatic slowing condition is plotted in red.

tion for the scattering force (equation 2.13) with the effective detuning of equation 2.40:

$$\ddot{x}(t) = \frac{\hbar k \Gamma}{2m} \frac{s_0}{1 + \frac{4}{\Gamma^2}(\delta_0 + \dot{x}(t)k + \frac{\mu_{\text{eff}} B(x(t))}{\hbar}) + s_0}. \tag{3.23}$$

The stochastic nature in the scattering events is not taken into account in this ansatz. However as long as the deceleration is not close to the maximum value, this can be neglected because the atom is able to scatter enough photons to fulfill always the adiabatic slowing condition. The results for initial velocities of 60 m/s to 310 m/s for rubidium and 100 m/s to 700 m/s for lithium atoms are shown in figure 3.16. The final velocities are around 30 m/s for rubidium and 56 m/s for lithium. The frequency detunings of the slowing laser light for this chosen configuration is 875 MHz for the rubidium laser and 1.09 GHz in the case of lithium. These final velocities can still be tuned to some extend by changing the detuning of the lasers and the end magnetic field of the slower. In the simulation it turned out, that already initially slow rubidium atoms will come to a complete stop at the transition of the rubidium slowing section to the last lithium section. If the change of the magnetic field in the last lithium section is not fast enough, the initially slow rubidium atoms are stopped before they are shifted out of resonance due to the finite linewidth of the transition. The simulation was used to optimize the magnetic profile to reduce the fraction of atoms pushed back into the slower to 0.3% of all slowed rubidium atoms. Because the magnetic field decreases after the last slowing section, this effect does not show up for lithium.

The spread of the atomic beam was calculated by numerically integrating equation 3.17 and using equation 3.14. In figure 3.17 the atomic beam width of the fastest velocity class of each element is

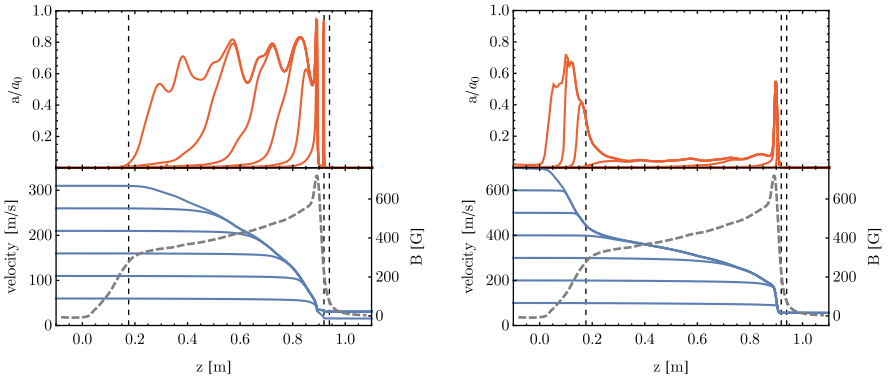

(a) Rubidium (b) Lithium

Figure 3.16: Simulated velocity of atoms flying through the Zeeman slower for different initial velocities. On top the ratio $\frac{a}{a_0}$ of the effective deceleration a and the maximum deceleration a_0 is illustrated.

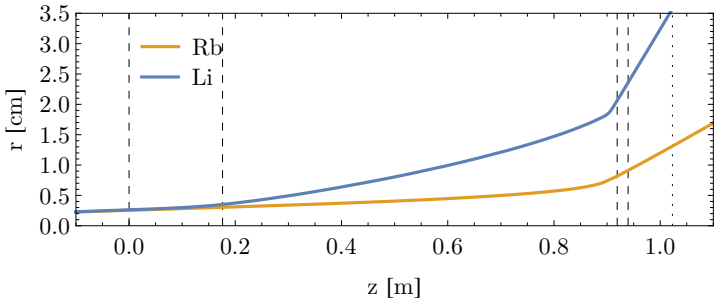

Figure 3.17: Atomic beam width of the velocity class $v_i = 300\,\mathrm{m/s}$ for rubidium and $v_i = 700\,\mathrm{m/s}$. The position of the MOT is marked in a dotted line, whereas the beginning of the slower and the seperation of the three different slowing parts is marked with dashed lines.

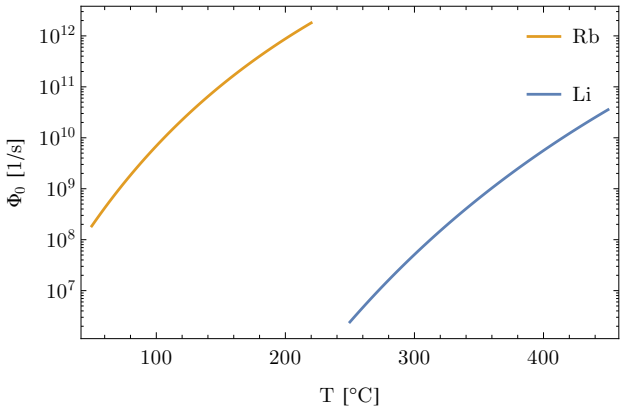

Figure 3.18: Influence of the oven temperature on the atomic flux at the MOT position. The results were obtained by calculating η_3 numerically.

plotted. These velocity classes were chosen, because they scatter the most photons during the slowing process, hence they have a wide spread angle at the end of the slower. Even for an end velocity of 55 m/s for the Lithium beam, the radius of 3.2 cm at the position of the MOT is much larger than the capture range. Rubidium in this case has a radius on the order of the MOT beams, enabling a large fraction of captured atoms. The parameters and dimension used for the calculation of the atomic flux are listed in table 3.2.

$\varnothing_{oven} = 4\,mm$	$T_{Rb} = 160\,°C$	$T_{Li} = 400\,°C$
$\varnothing_{MOT} = 2.4\,cm$	$a_{Rb,\,eff} = 0.55 \cdot a_{Rb\,max}$	$a_{Li,\,eff} = 0.55 \cdot a_{Li\,max}$
$d_{source} = 60\,cm$	$v_{Rb,max} = 310\,m/s$	$v_{Li,max} = 700\,m/s$
$d_{MOT} = 10.3\,cm$	$v_{Rb,end} = 30\,m/s$	$v_{Li,end} = 55\,m/s$

Table 3.2: These dimensions and parameters are used for the calculation of the atomic flux.

With $\eta_{Rb,1} = 0.28$, $\eta_{Rb,2} = 0.30$ (cf. equation 3.10) and $\eta_{Rb,3} = 0.74$ (cf. equation 3.20) one gets an atomic flux of $1.6 \cdot 10^{11}$ atoms per second in the MOT plane for rubidium. Lithium has a total atomic flux of $4.03 \cdot 10^{9}$ atoms per second with the following loss factors: $\eta_{Li,1} = 0.076$, $\eta_{Li,2} = 0.03$ and $\eta_{Li,3} = 0.002$. The atomic flux at the position of the MOT as a function of temperature is shown in figure 3.18. Since the vapor pressure increases exponentially, the atomic flux can be increased with higher temperatures. This increases also the number of atoms which cannot be slowed, leading to an increase in collisions with the atoms in the MOT. Hence the atom number in the MOT saturates.

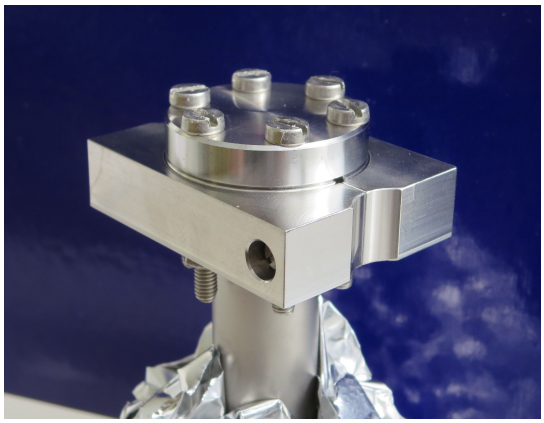

Figure 3.19: Self designed split ring for fixing the Zeeman slower vacuum tube to the gate valve. Here it is mounted in a test setup for a helium leak test.

3.3.5 *Construction*

As seen in section 3.3.4, the distance between the end of the Zeeman slower and the center of the MOT is very critical with respect to the atom flux. To get the maximum atomic flux, the Zeeman slower has to be as close as possible to the MOT chamber. A movable mount is used for the Zeeman slower, to be able to mount the vacuum tube to the chamber and then shift the slower as close as possible to the MOT chamber. This allows it to access the screw holes of the CF35-flange which would otherwise be blocked by the Zeeman slower coils.

The movable mount is made of a 316L steel tube with 22 mm inner diameter and 25 mm outer diameter holding all the windings of the Zeeman slower. This enables the Zeeman slower to be shifted over the knife edges of a CF16 rotatable flange which have a diameter of 21.3 mm. To connect the CF16 knife edge to another flange, an inhouse design for a split-ring was used, because no commercial product was available at this time. This split-ring is shown in figure 3.19 and was produced in the faculty mechanics workshop. It can be placed around the vacuum tube like a clamp and presses the knife edge into the copper gasket.

Two different types of wire are used for the Zeeman slower. A round enameled copper wire with 2 mm diameter is used for the upper layers carrying a current of 4.1 A. The insulation of the wire is high temperature durable up to 210 °C. This is high enough for a safe bake out process of the vacuum chamber. The rest of the layers are wound with a $4 \times 4\,\mathrm{mm}^2$ hollow core copper wire. The hollow core is 2.5 mm in diameter and enables direct water cooling of the wire. First a Kapton-FN insulated wire was chosen, because of its high maximum allowed temperature of 205 °C and its low thickness. Winding tests revealed that the Kapton insulation peeled of very easily at small bending radii. As a consequence glass yarn cov-

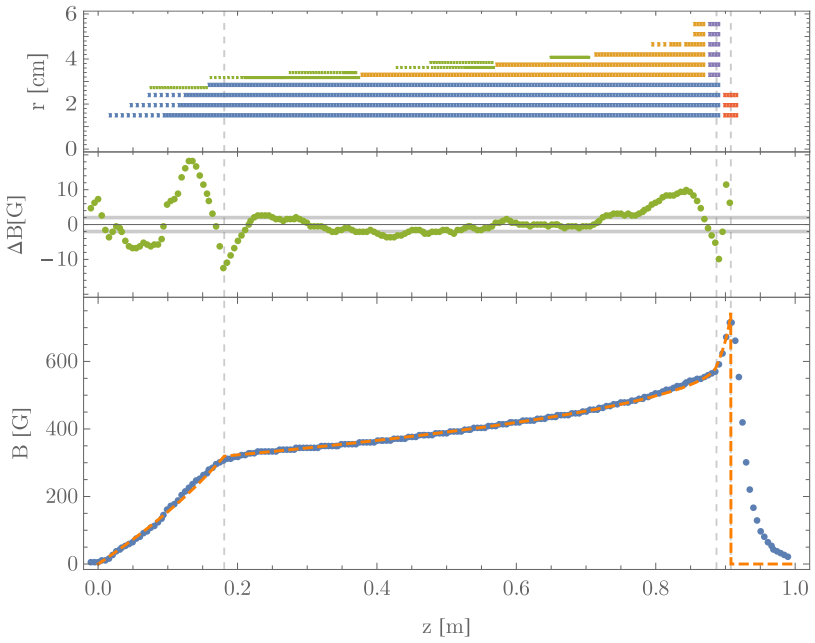

Figure 3.20: Measured magnetic field in blue dots and theoretical ideal field in dashed orange. The difference between the measurement and the ideal magnetic field is plotted in green dots. The adjusted windings are on top with the following color code: 116 A red, 39.7 A violett, 27.1 A blue, 19.7 A orange, 4.1 A green.

ered wire is used, which turned out to be much more stable. During the winding process, short circuits between the layers were regularly ruled out by measuring the magnetic field with a Hall sensor[12] fixed to a wooden stick. Wood was chosen as the mounting material because of its low magnetic permeability. The winding process revealed that the thick copper wire prevented gapless transitions between independently wound solenoids. As a result, the original simulated winding plan (see figure 3.14) was changed to the one shown in figure 3.20. The total thickness per wire, including winding inaccuracies, is 4.3 mm, whereas the simulations were done with 4.5 mm. This results in a total length of 89 cm, however the magnetic field could be matched to the theoretical ideal one at the shorter length by small adjustments in the currents. The final measured field is shown in figure 3.20. A larger deviation in the first part of the slower is still much smaller than the maximum allowed magnetic field gradient and the adiabatic slowing condition is still fulfilled as shown in 3.21.

The finished slower, mounted to the chamber, is shown in figure 3.22. The connections for the cooling water are made from 8 mm brass tubing which was brazed to the wire. This allows us to connect 12 bar cooling water via Prestolok connectors to the slower. The water flow is sufficient to cool the slower and no increase in temperature could be

12 Honywell SS496 A1

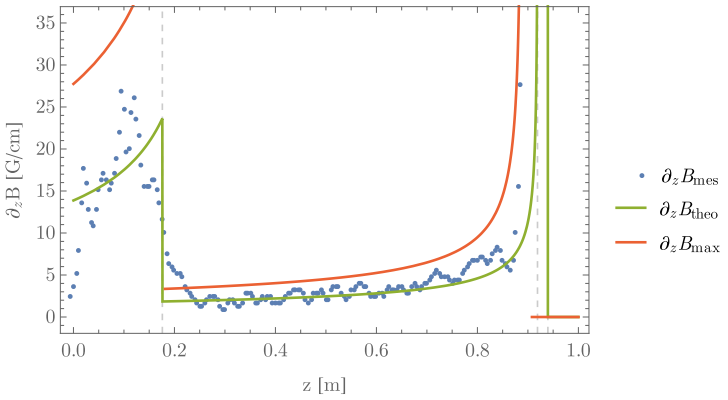

Figure 3.21: Calculated magnetic field gradient of the Zeeman slower (difference quotient). The adiabatic slowing condition is always fulfilled.

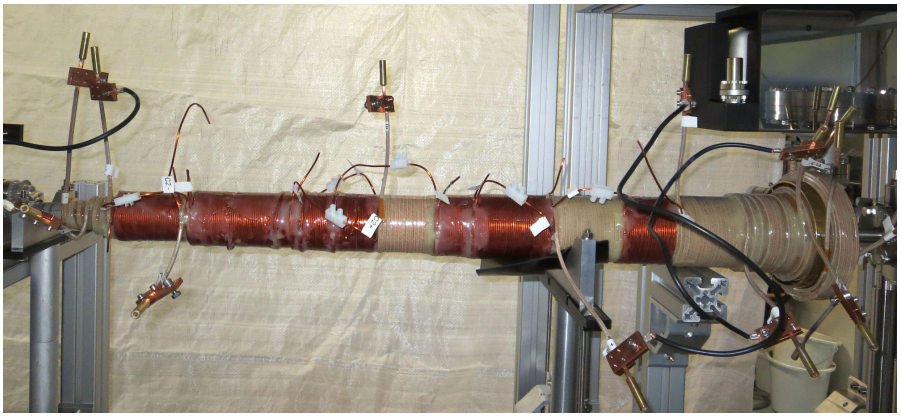

Figure 3.22: Zeeman slower mounted to the chamber. The connectors for the cooling water are braze-joined and the connectors for the current are special designed copper clamps to minimize the contact resistance. Because of its heavy weight, the slower is supported by several braces, unloading the vacuum seals.

measured. The coils are contacted by special designed copper clamps to minimize the contact resistance and heating of the wires.

3.4 MAGNETIC FIELDS

Mainly two types of coils are build around the chambers. There are Helmholtz and anti-Helmholtz coils around the MOT and experiment chamber to compensate small bias fields and gradients. This is important for molasses cooling or exact field control in precision measurements. On one axes of the MOT and experiment chamber water cooled Helmholtz and anti-Helmholtz coil pairs are mounted to produce large magnetic fields and gradients. The magnetic field gradients are used for the MOT or for spin sensitive imaging using a Stern-Gerlach configuration. The Helmholtz coils are capable of pro-

ducing homogeneous magnetic fields up to 1 kG and allow access to the broad s-wave Feshbach resonance of the two lowest ^{6}Li hyperfine ground states at around 830 G [91]. The coils are explained in more detail in the next sections.

3.4.1 *Design considerations*

In the experiment, it is necessary to switch the magnetic fields on a short timescale. For example the time duration for molasses cooling is only several milliseconds and therefore the magnetic field of the MOT has to be switched off much faster. The switching time of the magnetic field is mainly limited for two reasons. First, the inductance L of the coil gives a switching time $\tau = \frac{L}{R}$, where R is the resistance of the coil. The second reason for a long switching time are induced eddy currents in any conductive material by rapidly varying magnetic fields. These can decay much slower, depending on the material, and create magnetic fields itself. Therefore the coil holders and other possible closed conduction loops in the setup are split to suppress such effects. One solution would be to place the coils in vacuum, but this rises other problems. For example wires pressed together could generate a virtual leak, if small spaces remain between them. Also the insulation has to be vacuum compatible.

The induced voltage $U_{ind} = -L\frac{dI}{dt}$ depends on the inductance and the change in the current. By adding an ohmic resistor R_o, the switch off time $\tau = \frac{L}{R+R_o}$ can be in principle arbitrarily reduced (see Appendix A). However this implicates a fast current change and high induced voltages, which can destroy the insulation of the wires or the connected devices. With lower inductance, a shorter switching time can be achieved without exceeding the maximum voltage ratings of the devices. To get an idea of the important design considerations we first have to look at the magnetic field and how it scales.

The magnetic field B in the center of two coils with radius r and current I in Helmholtz configuration is

$$B = \mu_0 \frac{8}{\sqrt{125}} \frac{I \cdot N}{r}. \tag{3.24}$$

This means that the magnetic field increases with decreasing radius and increases linear with the number of windings.

The gradient of coils in anti-Helmholtz configuration is given by

$$\left.\frac{\partial B}{\partial z}\right|_{z=0} = \frac{3}{2}\frac{\mu_0 N I}{r^2} \times \frac{D}{r}\left(1 + \frac{D}{4r}\right)^{-\frac{5}{2}} \tag{3.25}$$

$$\approx 0.705 \times \frac{3}{2}\frac{\mu_0 N I}{r^2} \tag{3.26}$$

for a distance of the coils of $D = \sqrt{3}r$ (anti-Helmholtz condition), where the second and third derivative vanish at $z = 0$. This also implies that for a given current, a smaller radius produces a higher field

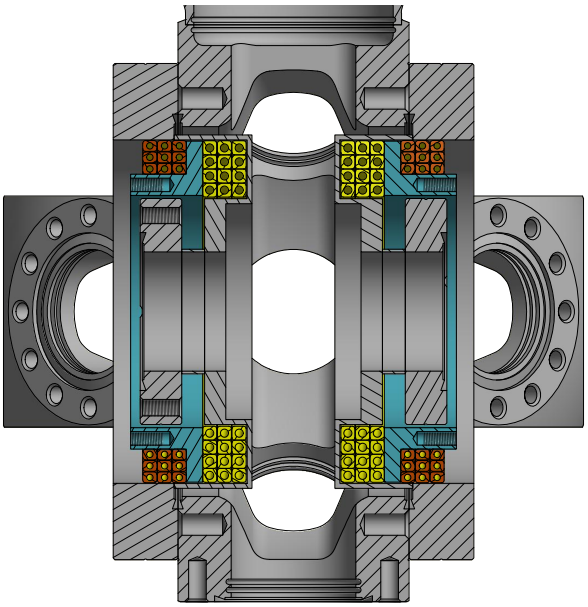

Figure 3.23: CAD drawing of the Feshbach coils (yellow) and gradient coils (brown) in the recessed bucket at the experiment chamber. The coil holder is drawn in blue for better visibility.

gradient. For the outlined reason, the coils are placed in recessed flanges as shown in figure 3.23 to reduce the distance between the coils and the required radius of the coils to fulfill the Helmholtz and anti-Helmholtz conditions.

With this in mind, the next step is to look at scaling properties of the dissipated power, inductance, switching time constant and induced voltage with respect to the winding number. These scaling laws are both valid for the Feshbach and gradient coils. For a given gradient or magnetic field, the required current scales with $I \propto N^{-1}$. The inductance of the coil can be estimated by the formula of a solenoid $L \propto r^2 N^2$. In the experiment the MOT and Feshbach coils are always pairs of coils which means the total inductance is between 2L and 4L depending on the mutual inductance of the coil pair. For the scaling laws, this does not play a role. Because the resistance of the coil is proportional to R the time constant $\tau = LR^{-1} \propto N$ scales with the winding number. The induced voltage is proportional to $U_{ind} \propto N$ for changing the current in a fixed time (then $\dot{I} \propto I \propto N^{-1}$).

In summary one can say, that for fast switching times and lower induced voltages during switching, a low number of windings is important. The downside is the increase in the required current and more dissipated power ($P = RI^2 \propto N^{-1}$). With hollowcore wire coils, as used in this setup, the heat can be easily managed and therefore a small number of windings is best suited for our setup. The coils are described in detail in the following sections.

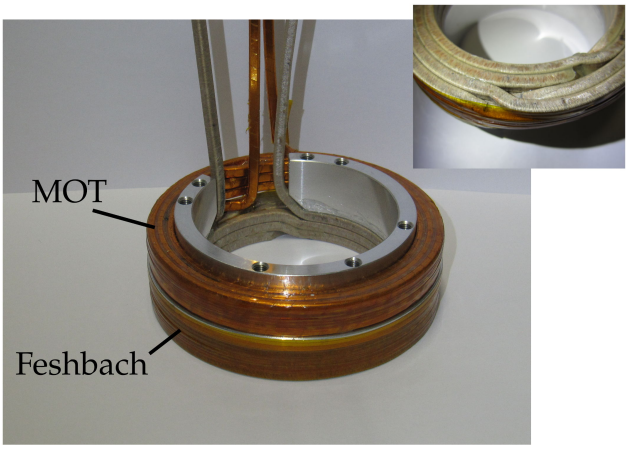

Figure 3.24: Picture of a stack of a MOT and a Feshbach coil mounted on the coil holder. The inset shows the transition between the different layers.

3.4.2 *Feshbach coils*

The Feshbach coils have to produce a high homogeneous magnetic field to access the broad lithium Feshbach resonance of the two lowest hyperfine states at approximately 830 G. They should also feature as low inductivity as possible to allow fast switching times, which means as less windings as possible with as small radius as possible (see section 3.4.1). To produce the desired homogeneous field, two coils are set in a Helmholtz configuration. This means that two round coils with radius R are placed symmetrically in axial distance R to each other. This leads to a magnetic field, which has ideally no deviations up to the second derivative ($\partial^2 B/\partial x^2 = 0$) at the center. Inhomogeneities in the field could otherwise lead to a lowering of the trap depth of the dipole trap.

The magnetic field was calculated as described in section 3.3.4. For still manageable currents of 400 A the coils have to be placed in recessed flanges to match the criteria mentioned above. The recessed bucket of the experiment chamber with the coils is shown in figure 3.23. The symmetry axis of the coil pair is showing in horizontal direction, whereas in the MOT chamber the axis is pointing vertical in the direction of gravitation.

The Feshbach coils are wound with the same 4 mm × 4 mm-wire as the Zeeman slower. Each one has four radial windings and three layers with an inner diameter of 70 mm and an outer diameter of 103 mm. A picture of a Feshbach and a MOT coil mounted on a coil holder is shown in figure 3.24. These coils create magnetic fields of

$$\frac{B(r, z = 0)}{I} = 2.51 \frac{G}{A} \tag{3.27}$$

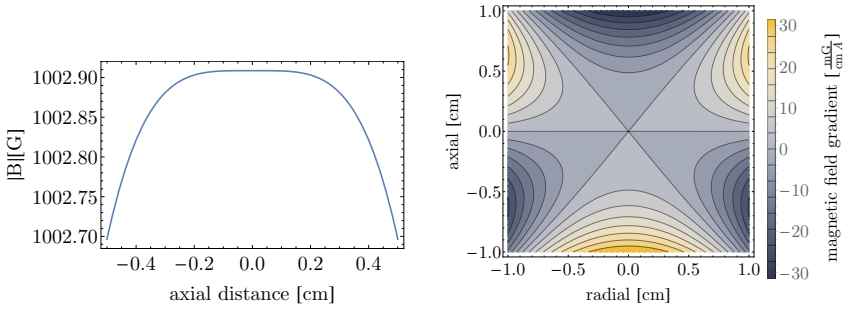

(a) Magnetic field for I_0 (b) Magnetic field gradient

Figure 3.25: Magnetic field of the Feshbach coils for an operating current $I_0 = 400\,A$. Distances are given with respect to the center of the Helmholtz configuration

TYPE	VALUE
max. current	400 A
max. magnetic field	1002 G
power dissipation	1.3 kW
max. temperature rise	8 K

Table 3.3: Estimated specifications of the Feshbach coils. The maximum current is limited by the current supplies.

(see figure 3.25) with very small gradients. For 1 mm off-centered, the simulation gives

$$\left.\frac{\partial B}{\partial z}\right|_{r=0,z=1\,mm} = -0.014\,\frac{G}{cm} \tag{3.28}$$

at 400 A. For a 100 µm wide dipole trap placed 1 mm off-centered in the magnetic field, this generates a potential gradient of

$$\Delta U = 0.014\,\frac{G}{cm}\cdot\mu_B\cdot 100\ \mu m = k_B\cdot 10\,nK\,,$$

which is negligible in the context of our planned experiment. Further specifications of the coils are listed in table 3.3. The wire is water cooled with 12 bar cooling water to reduce the heating of the coil. At 400 A a temperature increase of less than 8 K above the surrounding temperature was calculated. In the long term, a larger temperature increase could damage the glue of the coil and heating of the flange could reduce the vacuum quality in the chamber.

The coils are connected to two power supplies[13] working parallel in master-slave configuration to supply the high currents. The connectors are larger versions of the copper clamps used for the Zeeman slower. Fluctuations in the magnetic field could cause heating

13 Delta SM-30-200

of the atoms, so small current noise of the power supplies is necessary. The Delta power supplies have a rms ripple and noise of 20 mA at 200 A, which corresponds to a stability of 10^{-4} and causes magnetic field noise of maximum 0.07 G. The coils can be switched off by IGBTs[14](see Appendix A). To be able to have short switching times, an ultra low inductive ceramic resistor[15] and a flyback diode[16] are placed parallel to the coils to dissipate the energy of the magnetic field and limit the induced voltage. The IGBT is controlled by a Semikron SKHI23/12 R driver, which can supply high gate currents of up to 8 A necessary for a fast switching.

The wire is glued with Araldite 2012 epoxy adhesive, which provides strong bonding to metal and has a low thermal expansion coefficient. Furthermore, it can be heated up to 100 °C and still provides enough firmness. The temperature is monitored by TS NTC 203 sensors from B+B THERMO-TECHNIK and a self build control unit (see Appendix B), which can switch off the power supplies via an interlock switch in case of a cooling water failure or a malfunction of the power supplies. The employed sensors are small and react within less than two seconds to any temperature change.

3.4.3 *Gradient coils*

The gradient coils are used to create the quadrupole field for the MOT and to provide gradients to spatially split different spin states of the sample for imaging. The coils are mounted in a so-called anti-Helmholtz configuration which produces a quadrupole field for currents running in opposite directions of each coil. The spacing is not as critical as for a Helmholtz configuration, because they will always produce a gradient in the center, but the optimum distance is $\sqrt{3}$ times the radius of the coils. At this distance, the curvature in the center vanishes.

The coils are mounted inside the recessed flanges as shown in figure 3.23. A picture of a MOT coil mounted to a coil holder is shown in figure 3.24. The MOT coils are made of 3×4 mm wire[17] with a two millimeter hole inside allowing water cooling. The wire is arranged in three by three windings with an inner diameter of 84 mm. This allows to lead out the connections of the Feshbach coils on the inner side. The wire is insulated by Kapton-FN jacket[18].

14 Insulated-gate bipolar transitor (IGBT): Infinion FZ-800R16KF4
15 Kantal 503SP1R0LG1
16 Infinion BYM300A120DN2
17 Luvata profile 8329, 4x3mm, straight
18 Detakta, Kapton FN with a Teflon FEP layer

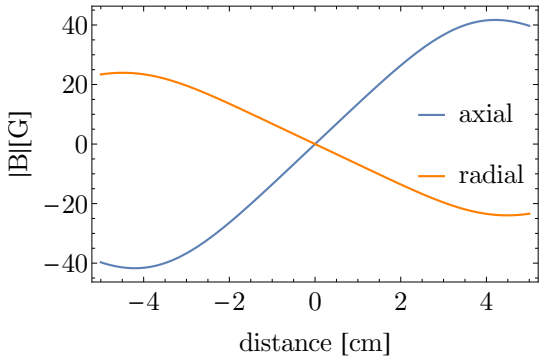

Figure 3.26: Magnetic field of the gradient coils for a current of 40 A, which creates an axial gradient of 13.6 G/cm in the center.

In this configuration the produced gradient is 0.33 G/(cm A) in axial direction, leading to a maximum possible gradient of

$$\left.\frac{\partial B}{\partial z}\right|_{\max,r,z=0} = 81\,\mathrm{G/cm} \tag{3.29}$$

in axial direction and half of it in radial direction at a current of 240 A. The current is limited by the maximum output current of the power supply. For a MOT in general $6-12\,\mathrm{G/cm}$ are sufficient, whereas for compressed MOTs gradients of up to $30-40\,\mathrm{G}$ are necessary. The design is therefore well suited to produce the required magnetic field for a MOT and even allows for higher gradients. The magnetic field for a current of 40 A is shown in figure 3.26.

As for the Feshbach coils, the wires were glued with Araldite 2012 (see section 3.4.2) and the temperature of the coils can be measured with the TS NTC 203 sensors. This is very important, since the coils could be easily destroyed in the case of cooling water failure. At a typical operating current of around 40 A, no increase in temperature is expected.

The current is supplied by two Agilent 240A 21V, each connected to one pair of coils. They have a rms ripple and noise at full output current of 40 mA. For fast switching times, each coil pair can be switched by an IGBT[19]. A flyback diode in series with a very low inductive resistor[20] is used to tune the switching time.

3.4.4 *Compensation coils*

Creating high magnetic fields and gradients is one important aspect of the experimental setup, which is discussed in section 3.4.2 and section 3.4.3. However the possibility to compensate small external fields and gradients, for example the earth magnetic field or any stray fields from ion pumps, is important as well. To efficiently use the optical

19 Eupec BSM200GA120DLC
20 Vishay NH025

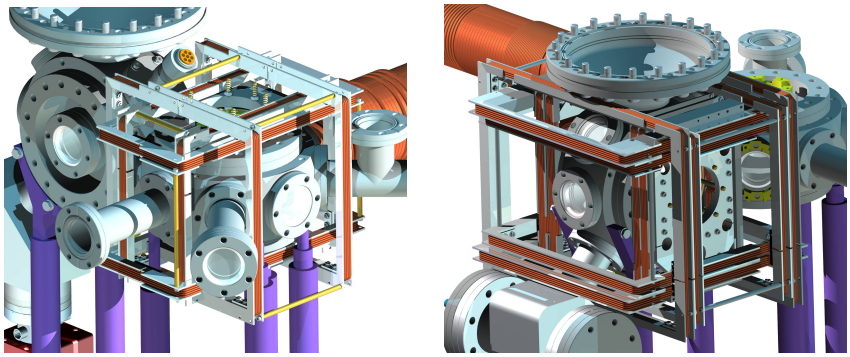

(a) MOT chamber (b) Experiment chamber

Figure 3.27: Low-field compensation coils around MOT and experiment chamber.

AXIS	MOT MAX. FIELD [G]	EXPERIMENT MAX. FIELD [G]	EXPERIMENT MAX. GRADIENT [G/cm]
x	14.3	9.9	0.38
y	9.6	9.8	0.82
z	11.0	10.0	1.33

Table 3.4: Specifications of the compensation coils around MOT and experiment chamber. All values are calculated for a maximum current of 10 A for each coil.

molasses cooling technique, the residual fields have to be smaller than 100 mG. A set of Helmholtz coils are build around the MOT chamber on three orthogonal axes. For the experiment chamber additional to Helmholtz pairs, three anti-Helmholtz coil pairs are used to compensate for small offset fields and gradients independently. The setup is shown in figure 3.27. The coils are wound with the same enameled copper wire as used for the Zeeman slower. It is two millimeter in diameter and the insulation can withstand up to 210 °C. The most important design consideration was the ability to compensate fields up to 10 G and gradients of 0.5 G/cm with the coils. Additionally, optical access to all view ports had to be guaranteed. Therefore the dimensions of each coil pair was designed individually to fit around the octagonal chamber. The calculated magnetic fields and gradients are listed in table 3.4.

The coils are wound in five by three layers on an aluminum frame made from a u-profile. This profile is 15 mm wide and 15 mm high and has a wall thickness of 2 mm. The frame consists of several pieces and is installed around the chamber after the bake out. One part of each aluminum frame is split and connected by a 5 mm thick acrylic glass plate to suppress eddy currents in the frame. Each coil pair

is connected to an individual power supply[21] capable of delivering up to 10 A with a rms noise of < 2 mA. The output current can be controlled by an analog input voltage from $0 - 10$ V.

3.4.4.1 *High-field compensation coils*

The coils described in the previous section are mainly to control low magnetic fields. For a strong magnetic field pointing mainly in one direction, the need to compensate fields perpendicular to this direction is highly reduced. In the fifties and sixties magnetic field homogeneity in high magnetic fields was discussed for nuclear resonance measurements [92, 93]. A strong magnetic field $\boldsymbol{B} = B_0 \hat{e}_z$ with magnitude B_0 pointing in z-direction and a variation of the magnetic field $\delta\boldsymbol{B}$ result in a total field variation of

$$|\boldsymbol{B} + \delta\boldsymbol{B}| = \sqrt{(B_0 + \delta B_z)^2 + \delta B_x^2 + \delta B_y^2} \tag{3.30}$$

$$= B_0 + \delta B_z + \frac{\delta B_x^2 + \delta B_y^2}{2B_0} + \dots \tag{3.31}$$

In our case, the magnetic field of the Feshbach coils is on the order of 10^3 G, whereas the deviations are on the order of one Gauss. Thus the expansion of the total magnetic field in equation 3.31 describes the magnetic field very well. The contributions of the x and y components of the magnetic field, suppressed by B_0, contribute less than 10^{-3} to the absolute value. Only variations in the z-component can have an impact on the total magnetic field.

To compensate these variations, the anti-Helmholtz compensation coils cannot be used. Looking at the magnetic field of such a coil (equation 3.21 for one current loop) it is easy to see, that in the xy-plane at $z = 0$ the magnetic field of these coils does not have a z-component. That means, deviations of the high field in the xy-plane cannot be compensated with such coils. In reference [92] Anderson discusses a variety of different coil configurations placed on two parallel planes, to correct for gradients and curvatures of B_z in different directions. For a magnetic field with $B_z \propto x$ or $B_z \propto y$ the paper proposes the symmetry of the coils, but no optimization has been performed. The basic principle is shown in figure 3.28. Two coil pairs with parallel axes produce opposing magnetic fields. These coil pairs with a coil radius ρ are displaced by 2D from each other and produce the desired field gradient. For an optimal ratio of $\frac{\rho}{d}$ and $\frac{\rho}{D}$ the gradient of B_z can be maximized, whereas higher order gradients vanish.

In our case some constraints for the design were given by our setup. The coils should not overlap with the inner view port to assure the possibility to mount lenses as close as possible to the chamber. Additionally the outer dimensions are limited by the regular compensation coils placed around the chamber. Also the distance D has a lower

21 EA-PS 3016-10 B with 0-16 V, 0-10 A

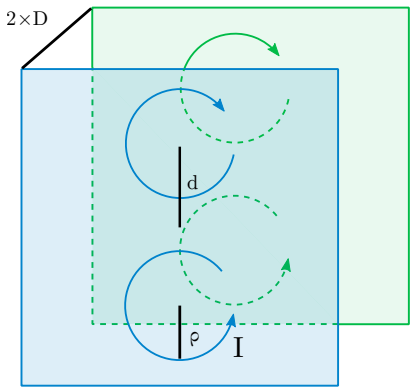

(a) Working principle for two coil pairs.

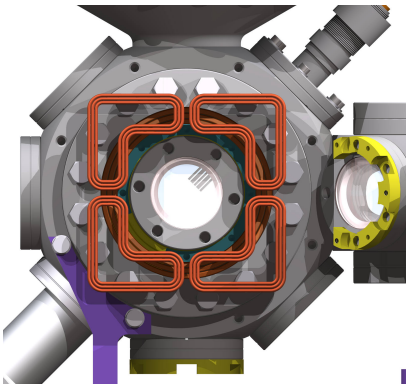

(b) CAD drawing of the compensation coils at the experiment chamber. On the back of the chamber, the corresponding pairs of the coils are mounted.

Figure 3.28: Compensation coils for the Feshbach field capable of producing a magnetic field with $B_z \propto x$ and $B_z \propto y$. This can be used to compensate gradients of the high field.

bound due to the chamber. Several designs of coils were simulated to find the best combination of gradient strength and linearity. In figure 3.29 the magnetic field of round coils and angled coils are shown. The angled coils are shown in figure 3.28 and will be used in the new setup. The gradient achievable in z-direction with this angled coils is $0.09\,{}^{\mathrm{G}}/_{(\mathrm{cmA})}$, whereas the gradient of the round coils is half of this value.

Comparing the second derivative, the round coils show slightly larger values in radial and axial direction. For smaller distance D this could be minimized, however our setup constrains the dimensions. The angled coils additionally offering enough space for the bracket of the Feshbach coils and a higher magnetic field gradient as the round coils. Therefore the angled coils constitute the best suited solution.

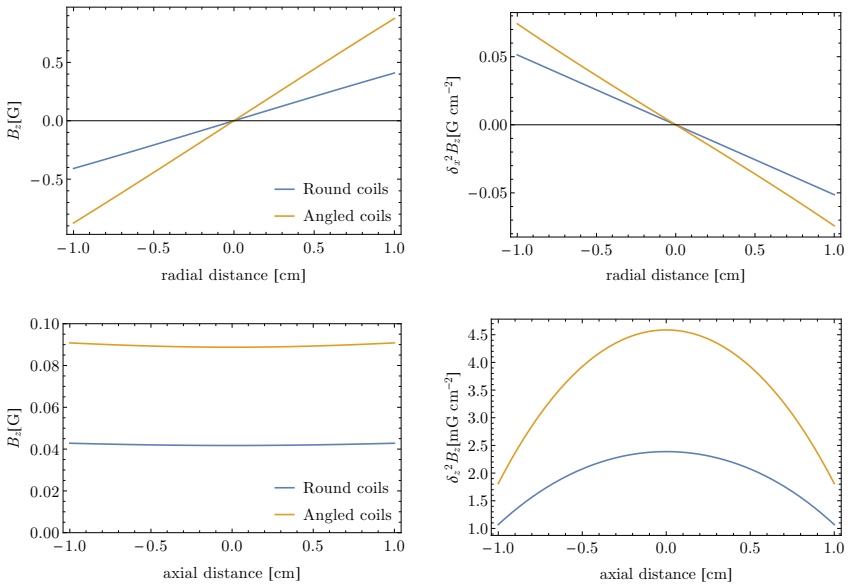

Figure 3.29: Radial and axial magnetic field B_z of the angled and round coils in the center of the chamber. The axial dependency is plotted 1 mm displaced in radial direction.

4

SUMMARY AND OUTLOOK

This thesis reports on the design and setup of pivotal parts of a new ultracold dual-species Rydberg experiment. These essential parts comprise a dual-species Zeeman slower, an elaborate magnetic field control, and a refined dual-species optical dipole trap. Furthermore the precursor experiment was fully disassembled except for most parts of the laser system and new infrastructure, including cooling water and a cage system around the optical table, was designed and build. The experiment will allow for the production of an ultracold quantum gas mixture of lithium and rubidium in combination with the generation, manipulation, and detection of Rydberg atoms and molecules.

The dual-species increasing field Zeeman slower providing a high flux for rubidium and lithium was simulated and constructed. A key design consideration for the Zeeman slower was to place it as close as possible to the MOT. This ensures that a large fraction of the lithium is caught despite of the large divergence angle of the lithium beam due to its light mass. As a consequence a movable design was chosen. Hollow-core wires were chosen to wind the Zeeman slower for the possibility of water cooling the coils. Measurements of the magnetic field show excellent agreement with the desired field profile. The maximum deviations are -6 G to 20 G in the parts slowing lithium and -4 G to 10 G for the part of rubidium, allowing always the successful slowing of the atoms. The simulations of the slowing process indicate a maximum capture velocity of the Zeeman slower of 310 $\mathrm{m/s}$ for rubidium and 700 $\mathrm{m/s}$ for lithium. At the end of the Zeeman slower, the rubidium and lithium atoms possess a velocity of 30 $\mathrm{m/s}$ and 55 $\mathrm{m/s}$, respectively.

To access a broad Feshbach resonance of lithium at 830 G [26], water cooled Helmholtz coil pairs were designed and built for the MOT and experiment chamber. Custom-made recessed flanges allow to position the coils close to the atoms and enable excellent homogeneous magnetic fields of up to 1 kG at an operation current of 400 A. The design is optimized for a low inductance, allowing fast switching of the magnetic field. Additional coil pairs at the experiment chamber allow for compensation of imperfections in the high magnetic field of the Helmholtz coils. Both MOT and experiment chamber will be equipped with gradient coils in anti-Helmholtz configuration, providing gradients of up to 80 $\mathrm{G/cm}$ in axial direction at an operation current of 240 A. The design is well suited to generate the magnetic quadrupole field of the MOT and allows spin-sensitive imaging in a

Stern-Gerlach configuration. To allow a stable and safe permanent operation of the machine, a safety interlock monitoring the temperature and currents of the coils was built.

The experiment requires not only high magnetic fields, but also the ability to compensate for any small stray magnetic fields, e. g. the earth magnetic field. For this reason, both, MOT and experiment chamber, will be equipped with Helmholtz coil pairs able to produce homogeneous magnetic fields up to 10 G in all three space dimensions. Three anti-Helmholtz coil pairs at the experiment chamber can compensate magnetic field gradients of up to $1\,\mathrm{G/cm}$.

In the new experiment the magnetic trap of the precursor experiment is replaced with an optical dipole trap due to stability reasons. Within this thesis, detailed calculations and simulations were conducted for different geometries of a combined optical trap for lithium and rubidium. The simulations show, that a good spatial overlap between the rubidium and lithium cloud can be achieved in an asymmetric crossed-optical dipole trap [63]. The proposed configuration allows for efficient evaporative cooling since trap frequency and trap depth are decoupled. It has previously been employed for the all-optical production of a degenerate gas [63].

Today, one year after the beginning of this thesis, the experiment is now ready for a first test of the Zeeman slower and the MOT. The vacuum system is assembled, leak-tight and baked, the Zeeman slower is integrated, almost all coils are wound and the oven is already filled with rubidium.

Outlook:
The next objective is the realization of a rubidium MOT and the testing of the Zeeman slower. For this the MOT and compensation coils have to be integrated into the experiment. Moreover, the slowing, cooling and repumping light has to be delivered to the MOT chamber and an imaging system has to be set up to measure the atom number and temperature of the MOT. Further steps include the installation of our experiment control consisting of an ADwin-proII system and an inhouse written control software [94]. The experiment control will allow for the optimization of the Zeeman slower and MOT parameters and will be later used to realize a stable non-stop operation of the experiment. A successful loading of the MOT allows then to test the optical transport of the rubidium atoms from the MOT to the experiment chamber.

After the successful completion of the above mentioned optimization and test of the setup, the ion microscope, the delay-line detector and the electric field control can be integrated. These elements are not yet built in, in order to reduce error sources and to simplify testing. Furthermore, the cooling laser system for lithium has to be built from scratch and a lithium reservoir has to be added. After this, the

Zeeman slower and the MOT have to be optimized for dual-species operation. Instead of a simultaneous loading of the MOT, a consecutive loading could be more preferable due to light-induced collisions between lithium and rubidium [95].

The completion of these technical tasks opens the door to the exploration of a plethora of physical phenomena, as for example the visualization of Rydberg clusters, the observation of dipole-mediated energy transport, and the study of heteronuclear Rydberg molecules. The understanding of these molecules is crucial for further experiments, in which the Rydberg molecules are planned to be used for probing the spatial correlations of a weakly- and strongly-interacting Fermi gas and for investigating atom-ion collisions in the ultracold, quantum regime.

A

CURRENT SWITCH

The setup contains two pairs of high magnetic field coils (section 3.4.2, Feshbach coils) and two pairs of high gradient coils (section 3.4.3, MOT coils). The Feshbach coils are used to tune the interactions via Feshbach resonances, whereas the MOT coils can be used for a MOT and spin-selective imaging in a Stern-Gerlach configuration. Also the last coil of the Zeeman slower has to be switched off to minimize the residual magnetic field in the MOT chamber. The coils have to be switched in below 1 ms. High currents of up to 400 A have to be switched which is done with insulated-gate bipolar transistors (IGBTs). Two Delta 30–200 power supplies are connected parallel to provide the Feshbach coils with the high currents as shown in figure A.1. Two Infinion FZ-800R16KF4 IGBTs are used to switch between the

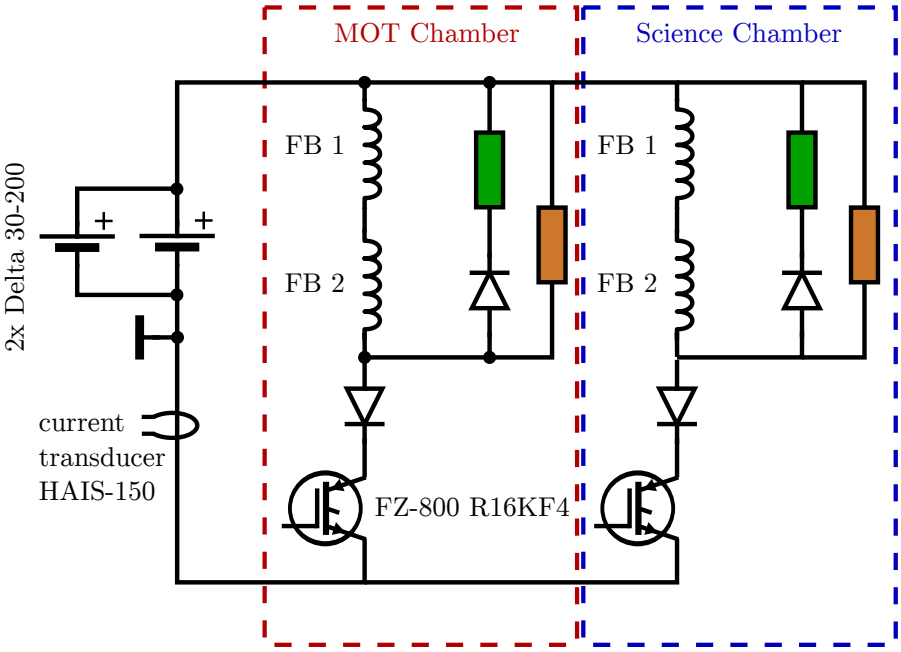

Figure A.1: Circuit diagram of the current switch for the high magnetic field coils. Two Delta 30-200 power supplies provide up to 400 A. Green indicates a high power 0.5 Ω resistor, where as the brown resistor is 1 kΩ.

two Feshbach coil pairs. The IGBTs can handle up to 800 A with a voltage drop of 2.1 V. In the case of the MOT coils, a maximum current of 240 A is given by the Agilent power supply (see figure A.2). In contrast to the Feshbach coils, each coil pair is connected to a separate power supply. The maximum current of the last coil of the Zeeman slower is limited to 125 A by the Sorensen power supply. In both cases

BSM200GA120DLC IGBTs from eupec are used to switch the currents. The maximum rated forward current is 370 A with a voltage drop of 2.1 V.
To limit the induced voltage caused by switching the current of the coils, flyback diodes (ultra fast rectifier diodes VS85HF120) are connected parallel to the coils. Additional resistors with 0.5 Ω decrease the switch time of the coils and dissipate the inductive energy. In the case of the Feshbach coils, non inductive ceramic resistors (Kanthal 503SP1R0LG1) are used. These resistors are very robust and can dissipate the energy of the magnetic field. Additional 1 kΩ resistors discharge remnant voltages on the flyback diodes. The IGBTs, diodes and power supplies are protected against high voltage spikes with transient voltage suppressor diodes and varistors.
Current transducers monitor the currents and are connected to a control unit. If the current exceeds set current limits, the unit switches off the power supplies via an interlock switch.

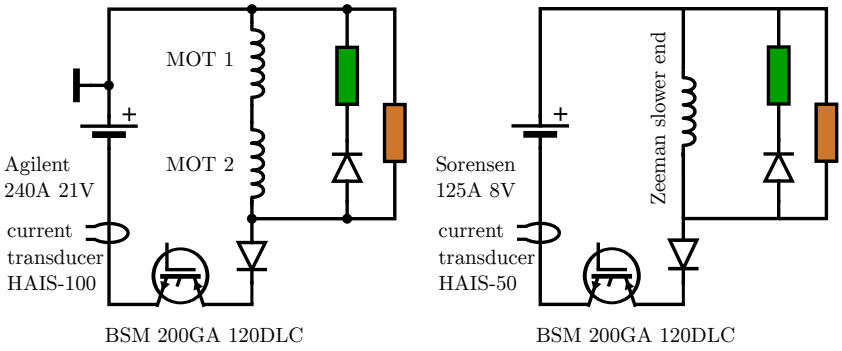

Figure A.2: The circuit diagram for the switching of the MOT coils and the last coil of the Zeeman slower closest to the MOT chamber. Green indicates a high power 0.5 Ω resistor, where as the brown resistor is 1 kΩ.

B

MONITOR CIRCUIT

The temperature monitoring system is based on a circuit developed by Schlagmüller [67] and is described in his thesis. The circuit was extended to allow a more flexible way of connecting current transducers and temperature sensors. The board offers now 16 channels and has the ability to store the measured values on a SD-card. The Mega arduino monitors the temperatures and currents. If any of these monitored values exceeds the allowed range, an output is switched from 5 V to ground, disabling the power supplies via an interlock circuit. The schematics and the new board design is shown in figure B.1 and figure B.2 respectively.

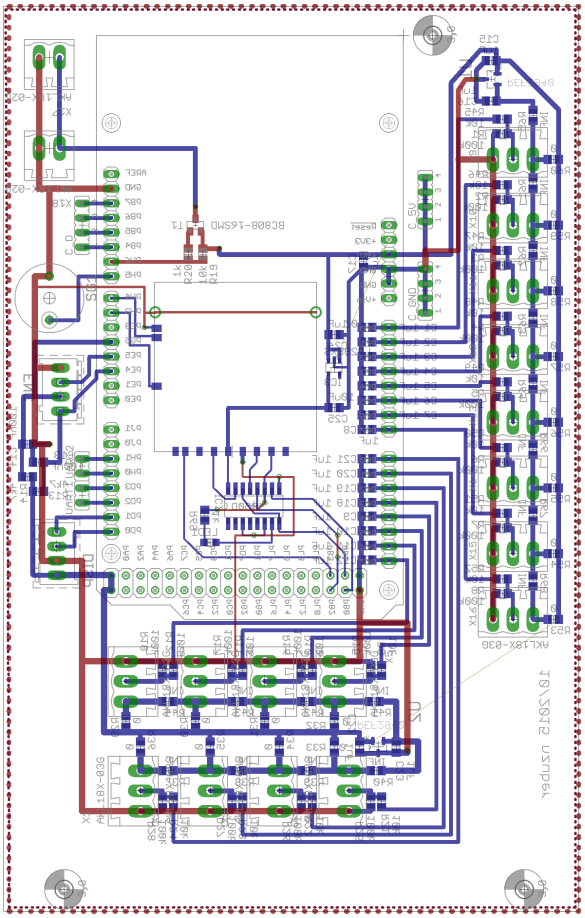

Figure B.1: The new board layout of the monitor unit to allow a flexible connection of the temperature sensors and current transducers. The upper conducting paths are drawn in blue, whereas the lower conducting paths are red.

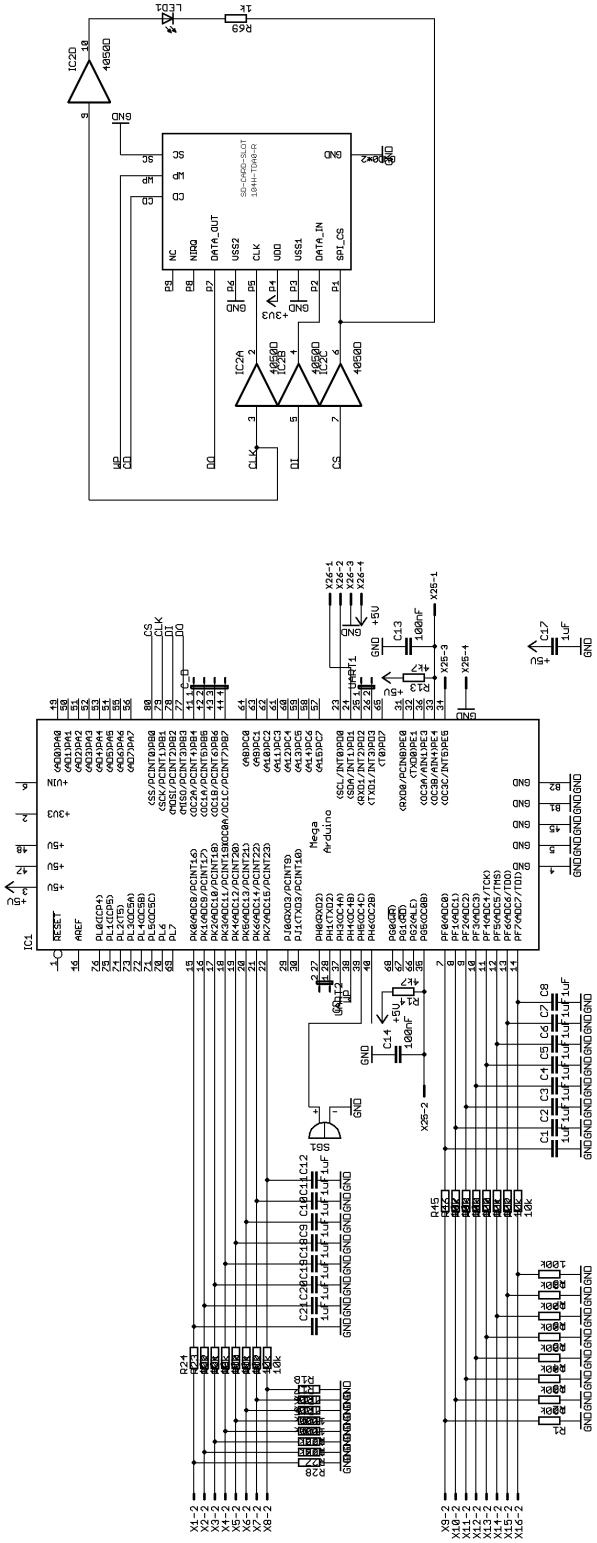

Figure B.2: The schematic shows the monitoring circuit with all 16 inputs and the voltage level shifter for the SD-card operating at 3.3 V.

C

CAGE SYSTEM

The experiment table is surrounded by a newly designed cage system to protect the sensitive optics on the one hand and on the other hand to shield the 300 W laser light of the transport laser. The cage system is built with aluminum profiles from Rose Krieger[1]. Laser safety tiles can be mounted on the sides to shield the laser light. The cage is closed from above by painted wooden boards blocking dust and providing storage space. Two flow boxes are integrated into the cage to provide a small overpressure inside the cage in order to prevent the accumulation of dust inside the cage. The whole setup is shown in figure C.1 and figure C.2.

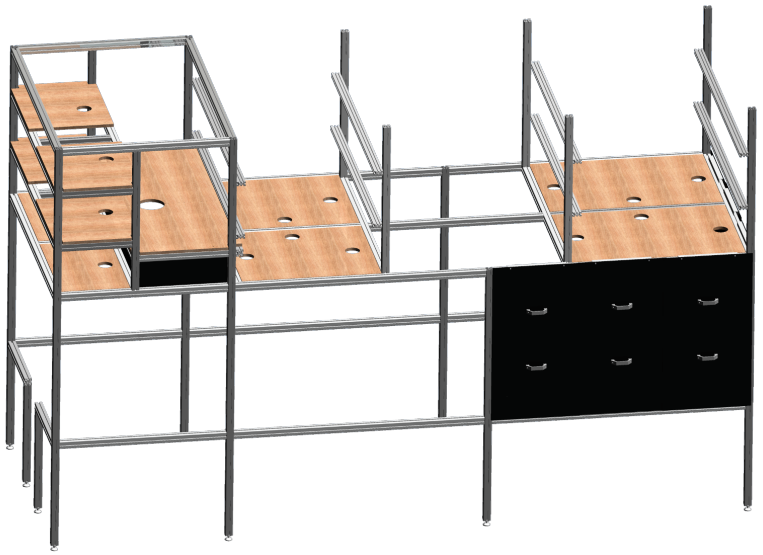

Figure C.1: CAD drawing of the whole cage system and laser safety plates on the side. The two flow boxes are not shown in this picture.

1 Blocan F-50x50

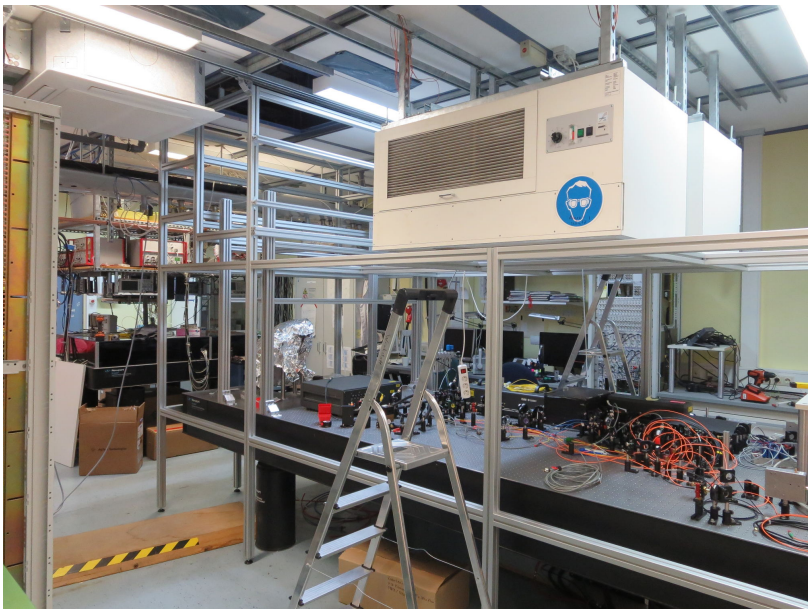

Figure C.2: The assembled cage system with the two integrated flow boxes.

BIBLIOGRAPHY

[1] Markus Greiner, Olaf Mandel, Tilman Esslinger, Theodor W. Hansch, and Immanuel Bloch. "Quantum phase transition from a superfluid to a Mott insulator in a gas of ultracold atoms." In: *Nature* 415.6867 (Jan. 2002), pp. 39–44. ISSN: 0028-0836. DOI: 10.1038/415039a.

[2] Immanuel Bloch. "Ultracold quantum gases in optical lattices." In: *Nat Phys* 1.1 (Oct. 2005), pp. 23–30. ISSN: 1745-2473. DOI: 10.1038/nphys138.

[3] Tim Langen, Sebastian Erne, Remi Geiger, Bernhard Rauer, Thomas Schweigler, Maximilian Kuhnert, Wolfgang Rohringer, Igor E Mazets, Thomas Gasenzer, and Jörg Schmiedmayer. "Experimental observation of a generalized Gibbs ensemble." In: *Science* 348.6231 (2015), pp. 207–211.

[4] Axel Griesmaier, Jörg Werner, Sven Hensler, Jürgen Stuhler, and Tilman Pfau. "Bose-Einstein Condensation of Chromium." In: *Phys. Rev. Lett.* 94.16 (Apr. 2005), p. 160401. DOI: 10.1103/PhysRevLett.94.160401.

[5] Serge Haroche. "Nobel Lecture: Controlling photons in a box and exploring the quantum to classical boundary." en. In: *Reviews of Modern Physics* 85.3 (July 2013), pp. 1083–1102. ISSN: 0034-6861, 1539-0756. DOI: 10.1103/RevModPhys.85.1083.

[6] Chris H. Greene, A. S. Dickinson, and H. R. Sadeghpour. "Creation of Polar and Nonpolar Ultra-Long-Range Rydberg Molecules." In: *Phys. Rev. Lett.* 85.12 (Sept. 2000), pp. 2458–2461. DOI: 10.1103/PhysRevLett.85.2458.

[7] Vera Bendkowsky, Bjorn Butscher, Johannes Nipper, James P. Shaffer, Robert Low, and Tilman Pfau. "Observation of ultralong-range Rydberg molecules." In: *Nature* 458.7241 (Apr. 2009), pp. 1005–1008. ISSN: 0028-0836. DOI: 10.1038/nature07945.

[8] Heiner Saßmannshausen, Frédéric Merkt, and Johannes Deiglmayr. "Experimental Characterization of Singlet Scattering Channels in Long-Range Rydberg Molecules." en. In: *Physical Review Letters* 114.13 (Mar. 2015). ISSN: 0031-9007, 1079-7114. DOI: 10.1103/PhysRevLett.114.133201.

[9] B. J. DeSalvo, J. A. Aman, F. B. Dunning, T. C. Killian, H. R. Sadeghpour, S. Yoshida, and J. Burgdörfer. "Ultra-long-range Rydberg molecules in a divalent atomic system." In: *Phys. Rev. A* 92.3 (Sept. 2015), p. 031403. DOI: 10.1103/PhysRevA.92.031403.

[10] Richard Schmidt, H. R. Sadeghpour, and E. Demler. "Mesoscopic Rydberg Impurity in an Atomic Quantum Gas." In: *Phys. Rev. Lett.* 116.10 (Mar. 2016), p. 105302. DOI: 10.1103/PhysRevLett.116.105302.

[11] Heike Kamerlingh Onnes. "Investigations into the properties of substances at low temperatures, which have led, amongst other things, to the preparation of liquid helium." In: *Nobel lecture* 4 (1913).

[12] P Kapitza. "Viscosity of liquid helium below the l-point." In: *Nature* 141.3558 (1938), p. 74.

[13] JF Allen and AD Misener. "Flow of liquid helium II." In: *Nature* 141.3558 (1938), p. 75.

[14] J. Bardeen, L. N. Cooper, and J. R.57 Schrieffer. "Theory of Superconductivity." In: *Phys. Rev.* 108.5 (Dec. 1957), pp. 1175–1204. DOI: 10.1103/PhysRev.108.1175.

[15] John V. Prodan, William D. Phillips, and Harold Metcalf. "Laser Production of a Very Slow Monoenergetic Atomic Beam." In: *Physical Review Letters* 49.16 (Oct. 1982), pp. 1149–1153. DOI: 10.1103/PhysRevLett.49.1149.

[16] Steven Chu, Leo Hollberg, John E. Bjorkholm, Alex Cable, and Arthur Ashkin. "Three-dimensional viscous confinement and cooling of atoms by resonance radiation pressure." In: *Physical Review Letters* 55.1 (1985), p. 48.

[17] Paul D. Lett, Richard N. Watts, Christoph I. Westbrook, William D. Phillips, Phillip L. Gould, and Harold J. Metcalf. "Observation of atoms laser cooled below the Doppler limit." In: *Physical Review Letters* 61.2 (1988), p. 169.

[18] Mike H. Anderson, Jason R. Ensher, Michael R. Matthews, Carl E. Wieman, and Eric A. Cornell. "Observation of Bose-Einstein condensation in a dilute atomic vapor." In: *science* 269.5221 (1995), pp. 198–201.

[19] K. B. Davis, M. O. Mewes, M. R. Andrews, N. J. van Druten, D. S. Durfee, D. M. Kurn, and W. Ketterle. "Bose-Einstein Condensation in a Gas of Sodium Atoms." In: *Phys. Rev. Lett.* 75.22 (Nov. 1995), pp. 3969–3973. DOI: 10.1103/PhysRevLett.75.3969.

[20] E Amaldi and E Segrè. "Effect of pressure on high terms of alkaline spectra." In: *Nature* 133 (1934), p. 141.

[21] Enrico Fermi. "Sopra lo Spostamento per Pressione delle Righe Elevate delle Serie Spettrali." In: *Il Nuovo Cimento (1924-1942)* 11.3 (1934), pp. 157–166. ISSN: 1827-6121. DOI: 10.1007/BF02959829.

[22] D. A. Anderson, S. A. Miller, and G. Raithel. "Photoassociation of Long-Range nD Rydberg Molecules." In: *Phys. Rev. Lett.* 112.16 (Apr. 2014), p. 163201. DOI: 10.1103/PhysRevLett.112.163201.

[23] A. T. Krupp, A. Gaj, J. B. Balewski, P. Ilzhöfer, S. Hofferberth, R. Löw, T. Pfau, M. Kurz, and P. Schmelcher. "Alignment of D -State Rydberg Molecules." en. In: *Physical Review Letters* 112.14 (Apr. 2014). ISSN: 0031-9007, 1079-7114. DOI: 10.1103/PhysRevLett.112.143008.

[24] Donald Booth, ST Rittenhouse, Jin Yang, HR Sadeghpour, and JP Shaffer. "Production of trilobite Rydberg molecule dimers with kilo-Debye permanent electric dipole moments." In: *Science* 348.6230 (2015), pp. 99–102.

[25] Thomas Niederprüm, Oliver Thomas, Tanita Eichert, Carsten Lippe, Jesús Pérez-Ríos, Chris H Greene, and Herwig Ott. "Observation of pendular butterfly Rydberg molecules." In: *arXiv preprint arXiv:1602.08400* (2016).

[26] C. H. Schunck, M. W. Zwierlein, C. A. Stan, S. M. F. Raupach, W. Ketterle, A. Simoni, E. Tiesinga, C. J. Williams, and P. S. Julienne. "Feshbach resonances in fermionic $^6\mathrmLi$." In: *Phys. Rev. A* 71.4 (Apr. 2005), p. 045601. DOI: 10.1103/PhysRevA.71.045601.

[27] A. Härter and J. Hecker Denschlag. "Cold atom–ion experiments in hybrid traps." In: *Contemporary Physics* 55.1 (2014), pp. 33–45. DOI: 10.1080/00107514.2013.854618.

[28] Marko Cetina, Andrew T. Grier, and Vladan Vuletiıfmmode \acutec\else ć\fi. "Micromotion-Induced Limit to Atom-Ion Sympathetic Cooling in Paul Traps." In: *Phys. Rev. Lett.* 109.25 (Dec. 2012), p. 253201. DOI: 10.1103/PhysRevLett.109.253201.

[29] Thomas Huber, Alexander Lambrecht, Julian Schmidt, Leon Karpa, and Tobias Schaetz. "A far-off-resonance optical trap for a Ba+ ion." In: *Nat Commun* 5 (Nov. 2014).

[30] T. P. Heavner, S. R. Jefferts, and G. H. Dunn. "Atomic mass of 6 Li using a Penning-ion-trap mass spectrometer." en. In: *Physical Review A* 64.6 (Nov. 2001). ISSN: 1050-2947, 1094-1622. DOI: 10.1103/PhysRevA.64.062504.

[31] Michael P. Bradley, James V. Porto, Simon Rainville, James K. Thompson, and David E. Pritchard. "Penning Trap Measurements of the Masses of C 133 s, R 8 7, 8 5 b, and N 23 a with Uncertainties$\leqslant$ 0.2 ppb." In: *Physical Review Letters* 83.22 (1999), p. 4510.

[32] C. C. McMullen, K. Fritze, and R. H. Tomlinson. "The half-life of Rubidium 87." In: *Canadian Journal of Physics* 44.12 (1966), pp. 3033–3038. DOI: 10.1139/p66-248.

[33] R. F. Gutterres, C. Amiot, A. Fioretti, C. Gabbanini, M. Mazzoni, and O. Dulieu. "Determination of the 87 Rb 5 p state dipole matrix element and radiative lifetime from the photoassociation spectroscopy of the Rb 2 0 g - (P 3 / 2) long-range state." en. In: *Physical Review A* 66.2 (Aug. 2002). ISSN: 1050-2947, 1094-1622. DOI: 10.1103/PhysRevA.66.024502.

[34] W. I. McAlexander, E. R. I. Abraham, and R. G. Hulet. "Radiative lifetime of the 2P state of lithium." In: *Phys. Rev. A* 54.1 (July 1996), R5–R8. DOI: 10.1103/PhysRevA.54.R5.

[35] G. Nienhuis, P. van der Straten, and S-Q. Shang. "Operator description of laser cooling below the Doppler limit." In: *Phys. Rev. A* 44.1 (July 1991), pp. 462–474. DOI: 10.1103/PhysRevA.44.462.

[36] Rudolf Grimm, Matthias Weidemüller M.ller, and Yurii B. Ovchinnikov. "Optical dipole traps for neutral atoms." In: *Advances in Atomic, Molecular and Optical Physics* 42 (2000), pp. 95–170.

[37] C.J. Foot. *Atomic Physics*. Oxford Master Series in Physics. OUP Oxford, 2004. ISBN: 978-0-19-103707-8.

[38] J. Dalibard and Claude Cohen-Tannoudji. "Dressed-atom approach to atomic motion in laser light: the dipole force revisited." In: *JOSA B* 2.11 (1985), pp. 1707–1720.

[39] H.A. Bethe and E.E. Salpeter. *Quantum Mechanics of One- and Two-Electron Atoms*. Springer Berlin Heidelberg, 2013. ISBN: 9783662128695.

[40] Charles Schwartz. "Theory of Hyperfine Structure." In: *Phys. Rev.* 97.2 (Jan. 1955), pp. 380–395. DOI: 10.1103/PhysRev.97.380.

[41] E. Arimondo, M. Inguscio, and P. Violino. "Experimental determinations of the hyperfine structure in the alkali atoms." English. In: *Reviews of Modern Physics* 49.1 (Jan. 1977), pp. 31–75. DOI: 10.1103/RevModPhys.49.31.

[42] S. Bize, Y. Sortais, M. S. Santos, C. Mandache, A. Clairon, and C. Salomon. "High-accuracy measurement of the 87 Rb ground-state hyperfine splitting in an atomic fountain." In: *EPL (Europhysics Letters)* 45.5 (1999), p. 558.

[43] Jun Ye, Steve Swartz, Peter Jungner, and John L. Hall. "Hyperfine structure and absolute frequency of the 87 Rb 5P 3/2 state." In: *Optics letters* 21.16 (1996), pp. 1280–1282.

[44] W. Raith and T. Mulvey. *Constituents of Matter: Atoms, Molecules, Nuclei, and Particles*. De Gruyter Experimental Physics. Taylor & Francis, 2001. ISBN: 9780849312021.

[45] L. Bergmann, M. Fink, W. Raith, C. Schaefer, H. Kleinpoppen, and N. Risch. *Bestandteile der Materie: Atome, Moleküle, Atomkerne, Elementarteilchen*. Lehrbuch Series. de Gruyter, 2003. ISBN: 9783110168006.

[46] N. Ramsey. *Molecular Beams*. International series of monographs on physics. OUP Oxford, 1985. ISBN: 978-0-19-852021-4.

[47] VI Balykin, VS Letokhov, and VI Mushin. "Observation of the cooling of free sodium atoms in a resonance laser field with a scanning frequency." In: *JETP lett* 29.10 (1979), pp. 560–564.

[48] Jean Dalibard and C. Cohen-Tannoudji. "Laser cooling below the Doppler limit by polarization gradients: simple theoretical models." In: *Journal of the Optical Society of America B* 6.11 (Nov. 1989), pp. 2023–2040.

[49] E. L. Raab, M. Prentiss, Alex Cable, Steven Chu, and D. E. Pritchard. "Trapping of Neutral Sodium Atoms with Radiation Pressure." In: *Phys. Rev. Lett.* 59.23 (Dec. 1987), pp. 2631–2634. DOI: 10.1103/PhysRevLett.59.2631.

[50] D. W. Sesko, T. G. Walker, and C. E. Wieman. "Behavior of neutral atoms in a spontaneous force trap." In: *J. Opt. Soc. Am. B* 8.5 (May 1991), pp. 946–958. DOI: 10.1364/JOSAB.8.000946.

[51] A. M. Steane, M. Chowdhury, and C. J. Foot. "Radiation force in the magneto-optical trap." In: *J. Opt. Soc. Am. B* 9.12 (Dec. 1992), pp. 2142–2158. DOI: 10.1364/JOSAB.9.002142.

[52] T. L. Gustavson, A. P. Chikkatur, A. E. Leanhardt, A. Görlitz, S. Gupta, D. E. Pritchard, and W. Ketterle. "Transport of Bose-Einstein Condensates with Optical Tweezers." en. In: *Physical Review Letters* 88.2 (Dec. 2001). ISSN: 0031-9007, 1079-7114. DOI: 10.1103/PhysRevLett.88.020401.

[53] O. J. Luiten, M. W. Reynolds, and J. T. M. Walraven. "Kinetic theory of the evaporative cooling of a trapped gas." In: *Phys. Rev. A* 53.1 (Jan. 1996), pp. 381–389. DOI: 10.1103/PhysRevA.53.381.

[54] P. W. H. Pinkse, A. Mosk, M. Weidemüller M.ller, M. W. Reynolds, T. W. Hijmans, and J. T. M. Walraven. "One-dimensional evaporative cooling of magnetically trapped atomic hydrogen." In: *Phys. Rev. A* 57.6 (June 1998), pp. 4747–4760. DOI: 10.1103/PhysRevA.57.4747.

[55] K. M. O'Hara, M. E. Gehm, S. R. Granade, and J. E. Thomas. "Scaling laws for evaporative cooling in time-dependent optical traps." en. In: *Physical Review A* 64.5 (Oct. 2001). ISSN: 1050-2947, 1094-1622. DOI: 10.1103/PhysRevA.64.051403.

[56] T. D. Lee and C. N. Yang. "Low-temperature behavior of a dilute Bose system of hard spheres. I. Equilibrium properties." In: *Physical Review* 112.5 (1958), p. 1419.

[57] S. R. Granade, M. E. Gehm, K. M. O'Hara, and J. E. Thomas. "All-Optical Production of a Degenerate Fermi Gas." en. In: *Physical Review Letters* 88.12 (Mar. 2002). ISSN: 0031-9007, 1079-7114. DOI: 10.1103/PhysRevLett.88.120405.

[58] Charles S. Adams, Heun Jin Lee, Nir Davidson, Mark Kasevich, and Steven Chu. "Evaporative cooling in a crossed dipole trap." In: *Physical review letters* 74.18 (1995), p. 3577.

[59] M. D. Barrett, J. A. Sauer, and M. S. Chapman. "All-Optical Formation of an Atomic Bose-Einstein Condensate." en. In: *Physical Review Letters* 87.1 (June 2001). ISSN: 0031-9007, 1079-7114. DOI: 10.1103/PhysRevLett.87.010404.

[60] Toshiya Kinoshita, Trevor Wenger, and David S. Weiss. "All-optical Bose-Einstein condensation using a compressible crossed dipole trap." en. In: *Physical Review A* 71.1 (Jan. 2005). ISSN: 1050-2947, 1094-1622. DOI: 10.1103/PhysRevA.71.011602.

[61] T. Weber. "Bose-Einstein Condensation of Cesium." In: *Science* 299.5604 (Jan. 2003), pp. 232–235. ISSN: 00368075, 10959203. DOI: 10.1126/science.1079699.

[62] Chen-Lung Hung, Xibo Zhang, Nathan Gemelke, and Cheng Chin. "Accelerating evaporative cooling of atoms into Bose-Einstein condensation in optical traps." en. In: *Physical Review A* 78.1 (July 2008). ISSN: 1050-2947, 1094-1622. DOI: 10.1103/PhysRevA.78.011604.

[63] J.-F. Clément, J.-P. Brantut, M. Robert-de Saint-Vincent, R. A. Nyman, A. Aspect, T. Bourdel, and P. Bouyer. "All-optical runaway evaporation to Bose-Einstein condensation." en. In: *Physical Review A* 79.6 (June 2009). ISSN: 1050-2947, 1094-1622. DOI: 10.1103/PhysRevA.79.061406.

[64] Robert Löw. "A versatile setup for experiments with Rubidium Bose Einstein condensates: From optical lattices to Rydberg matter." PhD thesis. Stuttgart: Universität Stuttgart, 2006.

[65] W Li et al. "A homonuclear molecule with a permanent electric dipole moment." In: *Science* 334.6059 (2011), pp. 1110–1114.

[66] Jonathan B. Balewski, Alexander T. Krupp, Anita Gaj, David Peter, Hans Peter Buchler, Robert Low, Sebastian Hofferberth, and Tilman Pfau. "Coupling a single electron to a Bose-Einstein condensate." In: *Nature* 502.7473 (Oct. 2013), pp. 664–667. ISSN: 0028-0836.

[67] Michael Thomas Schlagmüller. "A single Rydberg Atom interacting with a Dense and Ultracold Gas." PhD thesis. Stuttgart: Universität Stuttgart, 2016.

[68] Thomas Schmid. "High precision excitation, manipulation and detection of Rydberg atoms." MA thesis. Universität Stuttgart, Jan. 2014.

[69] E. Urban, T. A. Johnson, T. Henage, L. Isenhower, D. D. Yavuz, T. G. Walker, and M. Saffman. "Observation of Rydberg blockade between two atoms." In: *Nat Phys* 5.2 (Feb. 2009), pp. 110–114. ISSN: 1745-2473. DOI: 10.1038/nphys1178.

[70] T. Lauber, J. Küber, O. Wille, and G. Birkl. "Optimized Bose-Einstein-condensate production in a dipole trap based on a 1070-nm multifrequency laser: Influence of enhanced two-body loss on the evaporation process." In: *Phys. Rev. A* 84.4 (Oct. 2011), p. 043641. DOI: 10.1103/PhysRevA.84.043641.

[71] A. Steane, P. Szriftgiser, P. Desbiolles, and J. Dalibard. "Phase Modulation of Atomic de Broglie Waves." In: *Phys. Rev. Lett.* 74.25 (June 1995), pp. 4972–4975. DOI: 10.1103/PhysRevLett.74.4972.

[72] T. B. Swanson, D. Asgeirsson, J. A. Behr, A. Gorelov, and D. Melconian. "Efficient transfer in a double magneto-optical trap system." In: *J. Opt. Soc. Am. B* 15.11 (Nov. 1998), pp. 2641–2645. DOI: 10.1364/JOSAB.15.002641.

[73] K. Dieckmann, R. J. C. Spreeuw, M. Weidemüller, and J. T. M. Walraven. "Two-dimensional magneto-optical trap as a source of slow atoms." In: *Phys. Rev. A* 58.5 (Nov. 1998), pp. 3891–3895. DOI: 10.1103/PhysRevA.58.3891.

[74] Björn Karlsson. "Optical constants and spectral selectivity of stainless steel and its oxides." en. In: *Journal of Applied Physics* 53.9 (1982), p. 6340. ISSN: 00218979. DOI: 10.1063/1.331503.

[75] Robert Löw, Hendrik Weimer, Johannes Nipper, Jonathan B Balewski, Björn Butscher, Hans Peter Büchler, and Tilman Pfau. "An experimental and theoretical guide to strongly interacting Rydberg gases." In: *Journal of Physics B: Atomic, Molecular and Optical Physics* 45.11 (June 2012), p. 113001. ISSN: 0953-4075, 1361-6455. DOI: 10.1088/0953-4075/45/11/113001.

[76] C. Wieman and T. W. Hänsch. "Doppler-Free Laser Polarization Spectroscopy." In: *Phys. Rev. Lett.* 36.20 (May 1976), pp. 1170–1173. DOI: 10.1103/PhysRevLett.36.1170.

[77] Florian Christaller. "Aufbau und Charakterisierung von einem Lasersystem zur schmalbandigen Anregung von Rydberg-Atomen." Bachelorthesis. Universität Stuttgart, 2015.

[78] L. J. LeBlanc and J. H. Thywissen. "Species-specific optical lattices." In: *Phys. Rev. A* 75 (5 2007), p. 053612. DOI: 10.1103/PhysRevA.75.053612.

[79] Bindiya Arora, M. S. Safronova, and Charles W. Clark. "Tune-out wavelengths of alkali-metal atoms and their applications." In: *Phys. Rev. A* 84 (4 2011), p. 043401. DOI: 10.1103/PhysRevA.84.043401.

[80] C. Silber, S. Günther, C. Marzok, B. Deh, Ph. W. Courteille, and C. Zimmermann. "Quantum-Degenerate Mixture of Fermionic Lithium and Bosonic Rubidium Gases." In: *Phys. Rev. Lett.* 95.17 (Oct. 2005), p. 170408. DOI: 10.1103/PhysRevLett.95.170408.

[81] M. Taglieber, A.-C. Voigt, T. Aoki, T. W. Hänsch, and K. Dieckmann. "Quantum Degenerate Two-Species Fermi-Fermi Mixture Coexisting with a Bose-Einstein Condensate." In: *Phys. Rev. Lett.* 100 (1 2008), p. 010401. DOI: 10.1103/PhysRevLett.100.010401.

[82] A. Burchianti, J. A. Seman, G. Valtolina, A. Morales, M. Inguscio, M. Zaccanti, and G. Roati. "All-optical production of 6 Li quantum gases." In: *Journal of Physics: Conference Series* 594.1 (Mar. 2015), p. 012042. ISSN: 1742-6596. DOI: 10.1088/1742-6596/594/1/012042.

[83] Yuri B. Ovchinnikov. "A Zeeman slower based on magnetic dipoles." en. In: *Optics Communications* 276.2 (Aug. 2007), pp. 261–267. ISSN: 00304018. DOI: 10.1016/j.optcom.2007.04.048.

[84] Pierrick Cheiney, O. Carraz, D. Bartoszek-Bober, Stéphane Faure, François Vermersch, C. M. Fabre, G. L. Gattobigio, Thierry Lahaye, David Guéry-Odelin, and Renaud Mathevet. "A Zeeman slower design with permanent magnets in a Halbach configuration." In: *Review of Scientific Instruments* 82.6 (2011), p. 063115.

[85] P. N. Melentiev, P. A. Borisov, and V. I. Balykin. "Zeeman laser cooling of 85Rb atoms in transverse magnetic field." In: *Journal of Experimental and Theoretical Physics* 98.4 (2004), pp. 667–677. ISSN: 1090-6509. DOI: 10.1134/1.1757666.

[86] S. C. Bell, M. Junker, M. Jasperse, L. D. Turner, Y.-J. Lin, I. B. Spielman, and R. E. Scholten. "A slow atom source using a collimated effusive oven and a single-layer variable pitch coil Zeeman slower." en. In: *Review of Scientific Instruments* 81.1 (2010), p. 013105. ISSN: 00346748. DOI: 10.1063/1.3276712.

[87] William Bowden, Will Gunton, Mariusz Semczuk, Kahan Dare, and Kirk W. Madison. "An Adaptable Dual Species Effusive Source and Zeeman Slower Design Demonstrated with Rb and Li." In: *arXiv preprint arXiv:1509.07460* (2015).

[88] Asaf Paris-Mandoki, Matthew D. Jones, Jonathan Nute, Jizhou Wu, Sonali Warriar, and Lucia Hackermüller. "Versatile cold atom source for multi-species experiments." In: *Review of Scientific Instruments* 85.11 (2014), p. 113103.

[89] G. Edward Marti, Ryan Olf, Enrico Vogt, Anton Öttl, and Dan M. Stamper-Kurn. "Two-element Zeeman slower for rubidium and lithium." In: *Physical Review A* 81.4 (Apr. 2010), p. 043424. DOI: 10.1103/PhysRevA.81.043424.

[90] Sven Kroboth. "Laserkühlung von Ytterbiumatomen." Diploma thesis. Stuttgart: Universität Stuttgart, 2002.

[91] G. Zürn, T. Lompe, A. N. Wenz, S. Jochim, P. S. Julienne, and J. M. Hutson. "Precise Characterization of $^6\mathrmLi$ Feshbach Resonances Using Trap-Sideband-Resolved RF Spectroscopy of Weakly Bound Molecules." In: *Phys. Rev. Lett.* 110.13 (Mar. 2013), p. 135301. DOI: 10.1103/PhysRevLett.110.135301.

[92] Weston A. Anderson. "Electrical Current Shims for Correcting Magnetic Fields." en. In: *Review of Scientific Instruments* 32.3 (1961), p. 241. ISSN: 00346748. DOI: 10.1063/1.1717338.

[93] Marcel J. E. Golay. "Field Homogenizing Coils for Nuclear Spin Resonance Instrumentation." en. In: *Review of Scientific Instruments* 29.4 (1958), p. 313. ISSN: 00346748. DOI: 10.1063/1.1716184.

[94] S. Jennewein. "Building an Apparatus for Cold Rubidium Rydberg Atoms." Diploma Thesis. Universität Stuttgart, 2012.

[95] Keith Ladouceur, Bruce G. Klappauf, Janelle Van Dongen, Nina Rauhut, Bastian Schuster, Arthur K. Mills, David J. Jones, and Kirk W. Madison. "Compact laser cooling apparatus for simultaneous cooling of lithium and rubidium." In: *J. Opt. Soc. Am. B* 26.2 (Feb. 2009), pp. 210–217. DOI: 10.1364/JOSAB.26.000210.

DANKSAGUNG

An dieser Stelle möchte ich mich noch bei all jenen bedanken, die zum Gelingen dieser Masterarbeit und meines Studiums beigetragen haben.

Zuallererst möchte ich Prof. Dr. Tilman Pfau nicht nur für die Möglichkeit danken, an seinem Institut diese Masterarbeit zu schreiben und bei einem völlig neuen Projekt mit zu arbeiten, sondern das ich auch ein Auslandssemester an der University of Toronto verbringen konnte.

Vielen Dank auch an Prof. Dr. Martin Dressel in seiner Funktion als Mitberichter dieser Arbeit.

Einen ganz herzlichen Dank an Thomas Schmid und Christian Veit für die tolle Zusammenarbeit an diesem großen Projekt und der großartigen Unterstützung während der Masterarbeit, die auch während dem tagelangen Wickeln des Zeeman slowers nie nachgelassen hat.
Zudem möchte ich mich auch bei Dr. Robert Löw für die netten Diskussionen und hilfreichen Ratschläge bedanken.

Dem ganzen 5. Physikalischen Institut danke ich für die tolle Atmosphäre und die große Hilfsbereitschaft.

Zum Schluss noch ein große Dankeschön an meine Familie und Freunden, die mich während dem Studium immer tatkräftig unterstützten.

EHRENWÖRTLICHE ERKLÄRUNG

Hiermit versichere ich, dass die Arbeit selbstständig verfasst wurde und keine anderen als die angegebenen Quellen benutzt wurden. Alle wörtlich oder sinngemäß aus anderen Werken übernommenen Aussagen sind als solche gekennzeichnet. Die Arbeit war weder vollständig noch in Teilen Gegenstand eines anderen Prüfungsverfahrens. Der Inhalt des elektronischen Exemplars stimmt mit dem des Druckexemplars überein.

Stuttgart, 20. April 2016

Nicolas Zuber